March 2016

Supramolecular Strategies for the Generation of Nanoparticle Assemblies and Biomolecular Thin Films

Bradley P. Duncan
University of Massachusetts Amherst

SUPRAMOLECULAR STRATEGIES FOR THE GENERATION OF NANOPARTICLE ASSEMBLIES AND BIOMOLECULAR THIN FILMS

A Dissertation Presented

by

BRADLEY P. DUNCAN

Submitted to the Graduate School of the

University of Massachusetts Amherst in partial fulfillment

of the requirements for the degree of

DOCTOR OF PHILOSOPHY

February 2016

Department of Chemistry

SUPRAMOLECULAR STRATEGIES FOR THE GENERATION OF NANOPARTICLE ASSEMBLIES AND BIOMOLECULAR THIN FILMS

A Dissertation Presented

by

BRADLEY P. DUNCAN

Approved as to style and content by:

_____
Vincent M. Rotello, Chair

_____
Michael J. Knapp, Member

_____
Matthew A. Holden, Member

_____
Anthony D. Dinsmore, Member

_____
Craig T. Martin, Department Head
Department of Chemistry

DEDICATION

To my family, friends, and mentors whose indispensable guidance and support have helped bring this research to fruition

ACKNOWLEDGEMENTS

I would like to express my sincere gratefulness to my family, friends, and colleagues without whose constant support and encouragement none of this research would have been possible.

First, I would like to thank Professor Vincent M. Rotello for his valuable guidance and mentorship throughout this work. His vision and rigorous approach to scientific inquiry have and will continue to have a tremendous influence on my research career.

I would like to acknowledge the professors who have served as my research committee members, Professor Matthew A. Holden, Professor Jeanne A. Hardy, Professor Michael J. Knapp, and Professor Anthony D. Dinsmore for their constructive comments and constant academic support throughout my graduate studies.

I owe a great debt of gratitude to all of the present and past members of the Rotello group. All of this research has been accomplished in collaboration with group members. I have truly appreciated the friendly and cooperative environment in the lab. Although every member helped me develop as a scientist, I would specifically like to mention, Rui, Brian Creran, Li-Sheng, Ryan, Daniel, Gulen, Subinoy, Ying, Akash, Xiaoning, Bo, Krish, Chae-kyu, Youngdo, Sung Tae, Chang-Soo, Myoung, Eunhee, Vikas, Rubul, Mahdieh, Raj, NLe, and Brian Jordan. I would also like to thank Carol, Carrie, Bob and the rest of the chemistry staff for their support inside and outside the lab.

Finally, I would like to thank my entire family for their love and support, especially my parents, brothers, and my wife Molly. Their endless understanding and care have been a source of continual inspiration for me.

ABSTRACT

SUPRAMOLECULAR STRATEGIES FOR THE GENERATION OF NANOPARTICLE ASSEMBLIES AND BIOMOLECULAR THIN FILMS

FEBRUARY 2016

BRADLEY P. DUNCAN, H.A.B., SAINT ANSELM COLLEGE

Ph.D., UNIVERSITY OF MASSACHUSETTS AMHERST

Directed by: Professor Vincent M. Rotello

The conceptual framework of supramolecular chemistry elucidates a powerful set of strategies for chemists to generate functional nanomaterials based on intermolecular forces. My research focused on tuning the molecular interactions of nanoscale components to create larger structures with enhanced properties. In one approach, I developed and optimized an additive-free, nanoimprint lithography-based methodology to generate stable thin films from a variety of proteins. The generalized process retains intrinsic properties of the protein as demonstrated by selective cellular adhesion. The heat and pressure of the nanoimprinting process induces slight structural reorganization of the peptide side chains to yield highly stable films held together by inter-protein hydrophobic forces. The selective cell adhesion shown by our initial model proteins was further harnessed using inkjet printing to control the micropatterning of biomaterial substrates in a highly modular fashion. The protein-based ‘ink’ deposition when combined with the nanoimprint lithography stabilization procedure permits the rapid creation of patterns and film compositions not achievable using other nanomanufacturing techniques. My research also demonstrates that the supramolecular interactions that

occur at the surface of nanomaterials can be used to create complexes to interact with the human olfactory system. Surface functionalized gold nanoparticles serve as selective and reversible inhibitors for enzymes that upon displacement by analytes in solution generate a scent-based signal from pro-fragrance molecules. The self-assembly of nanoparticles at oil/water interfaces led to the development of an alternative method to form nanoparticle-polymer nanocomposites. The assembled composite system, generated by crosslinking and phase transferring hydrophilic nanoparticles into the hydrophobic oil core, showed remarkable stability to the phase disrupting influence of ethanol. This inside-out Pickering emulsion template later aided in the creation of a multimodal nanoparticle stabilized capsule platform for the treatment of bacterial biofilms. The amine surface functionality of the nanoparticles both improved delivery to bacterial biofilms through complementary electrostatic interactions as well as stabilized the therapeutic payload of the capsules through the formation of Schiff bases. Overall, these examples highlight the potency of using supramolecular strategies for the intelligent design of nanomaterials.

TABLE OF CONTENTS

Page

LIST OF TABLES

Table Page

LIST OF FIGURES

Figure Page

CHAPTER 1

ASSEMBLING FUNCTIONAL NANOMATERIALS

1.1. Overview of Nanoscale Materials

Nanomaterials are defined as objects that possess a component with at least one dimension in the nanometer length scale. These nanoscale materials are particularly attractive since they display unique physiochemical properties not achievable with bulk material analogues.[1] Examples of commonly used nanoscale materials are shown in Figure 1.1. The large surface area to volume ratios possessed by nanomaterials make them advantageous materials for catalytic,[2] therapeutic,[3] sensing,[4] and electronic applications.[5] Furthermore, the biologically relevant scale of nanomaterials can be employed to interface and interact many biological structures, such as cell membranes and proteins, to provide unique insight into the underlying behaviors.[6] The following chapter will focus on the materials and methods that served as the background for this thesis.

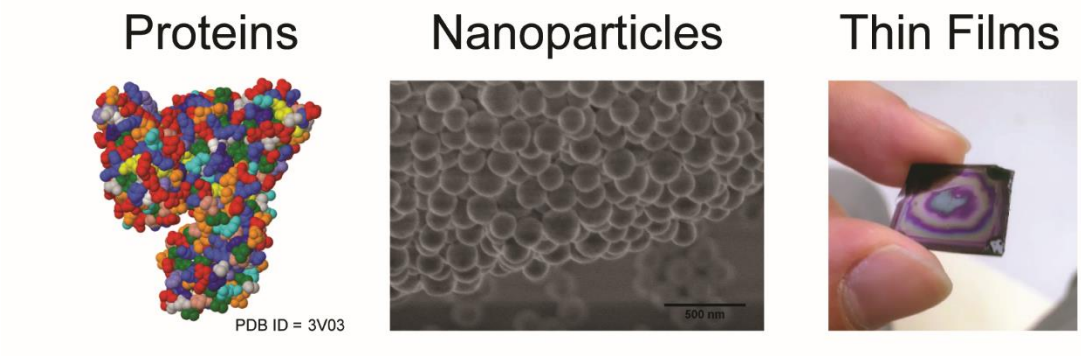

Figure 1.1: A space filling model of bovine serum albumin, a scanning electron micrograph of silica nanoparticles, and a thin protein film on a silica wafer are shown as representative nanomaterials.

1.1.1. Proteins

Proteins provide a naturally occurring nanoscale building material. Most proteins are constructed using 100-500 of amino acid building blocks or residues. The individual amino acids possess side chains of varying functionality. These groups give the amino acids their unique chemical properties. The order in which the amino acids are sequentially arranged is described as the primary structure of the protein. Dependent on this ordering of the side chains, segments of the polymer assemble into various structures due to van der Waals, hydrogen bonding, electrostatic, hydrophobic, and disulfide crosslinking interactions. These individual secondary structures of the protein, such as alpha helices and beta-sheets, are further assembled into a tertiary structure that gives the protein an overall structural character such as globular, fibrous, or random coil. Their inherent structure and functionality allows their rapid incorporation into functional materials.

Proteins serve a variety of biological functions including cell signaling, enzymatic catalysis, and structural support of tissues. The behavior of the protein is dependent on its tertiary structure. Proteins can be divided into 3 main classes: globular, fibrous, and membrane proteins which correlates with their tertiary structures. Globular proteins are primarily water soluble, generally spherical in three dimensional shape, and can be transporter proteins as well as enzymes. Fibrous proteins are structural biomacromolecules that assemble to form connective tissues which are water insoluble. Membrane proteins interact with biological membranes such as the cell's phospholipid bilayer to aid in cellular response to environmental stimuli.

1.1.2. Nanoparticles

Nanoparticles possess unique physiochemical properties compared to bulk materials.[7] These size dependent characteristics of nanomaterials, as shown in Table 1.1, give rise to a variety of phenomenon such as quantum confinement of photons,[8] enhanced permeation and retention within cancerous tissues,[9] and superparamagnetic behavior of transition metals.[10] Furthermore, the behavior of nanoparticles depends greatly on the surface functionalization of the nanoparticle.[11] The chemical moieties present at the surface of nanoparticles can be tailored to regulate biological processes, such as exocytosis, as demonstrated by the work of Rotello *et al.*[12] Additionally, Mirkin and coworkers have shown that DNA functionalized nanoparticles can be "crystallized" into larger assemblies through rational design rules of the surface chemistry of the individual nanoparticles.[13]

Table 1.1: Metal and semiconductor nanoparticles commonly used for biological applications and their corresponding properties. Reprinted from Ref. 7 with permission from Wiley-VCH Verlag GmbH & Co.

Core material	**Characteristics**	**Ligand(s)**	**Applications**
Au	Optical absorption, fluorescence and fluorescence quenching, stability	Thiol, disulfide, phosphine, amine	Biomolecular recognition, delivery, sensing
Ag	Surface-enhanced fluorescence	Thiol	Sensing
Pt	Catalytic property	Thiol, phosphine, amine, isocyanide	Bio-catalyst, sensing
CdSe	Luminescence, photo-stability	Thiol, phosphine, pyridine	Imaging, sensing
Fe_2O_3	Magnetic property	Diol, dopamine derivative, amine	MR imaging and biomolecule purification
SiO_2	Biocompatibility	Alkoxysilane	Biocompatible by surface coating

1.1.3. Thin Films

Thin films of polymeric materials have been used for a variety of applications such as antifouling coatings,[14] photovoltaics,[15] and biosensors.[16] These films offer a tailorable interface to alter the functional, mechanical, and biological behavior of substrates in a modular fashion.[17] As demonstrated in Figure 1.2, a thin film can be held together by a variety of supramolecular forces between the individual components comprising the film.[18] In addition, the layers of materials assembled on surfaces often vastly alters the properties of the underlying substrate.[19] The chemical structure of the layer material, method used for coating the underlying substrate, and post-functionalization can all be used to modify the final behavior of the thin film.[20]

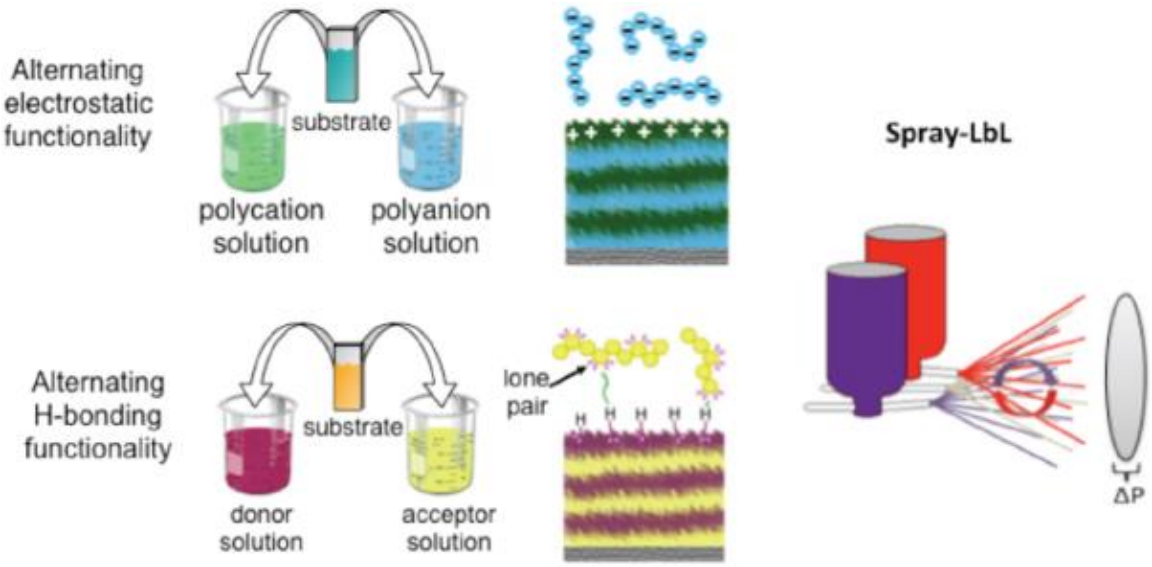

Figure 1.2: Schematic depiction of methods used to form Layer-by-Layer (LbL) films. Supramolecular interactions between the polymers within the film affect the behavior of the overall device. Spray-LbL is an example of rapid method to deposit these films on medical devices. Reprinted from Ref. 18 with permission from Wiley-VCH Verlag GmbH & Co.

Thin films are particular attractive scaffolds for creating biomaterial coatings. For instance, the surface functionality of thin films has been shown to modulate immune

response,[21] protein adsorption,[22] and affect cellular adhesion/behavior.[23] Biodegradability can also be tuned to create controlled release drug platforms.[24] For example, Hammond *et al*. demonstrated that thin polymer coatings on bone implants that contain osteoconductive hydroxyapatite and osteoinductive recombinant human bone morphogenetic protein-2 effectively induced integration of the implant into the host tissue.[25] Overall, the surface functionalities of the components of the thin film tend to dictate the performance of the film. Therefore, expanding the range of incorporable, biocompatible polymers to form stable films would greatly improve the field.

1.2. Nanoscale Fabrication Techniques

The two basic methodologies for the generation of nanomaterials can be classified as either "bottom-up" or "top-down" approaches.[26] Bottom-up approaches rely on the spontaneous assembly of smaller components into larger materials dependent on the interactions between the individual constituents. Top-down methods, on the other hand, reduce larger substrates into smaller units via etching, milling, or other physical removal of surface elements from the initial material. As shown in Figure 1.3, both of these strategies can be used to generate similar structures albeit via diametrically opposed pathways. Bottom-up assemblies generate feature sizes that cannot be created following a top-down approach. Structures that are formed from top-down approaches can be achieved on much larger substrates and more rapidly than bottom-up approaches can produce.

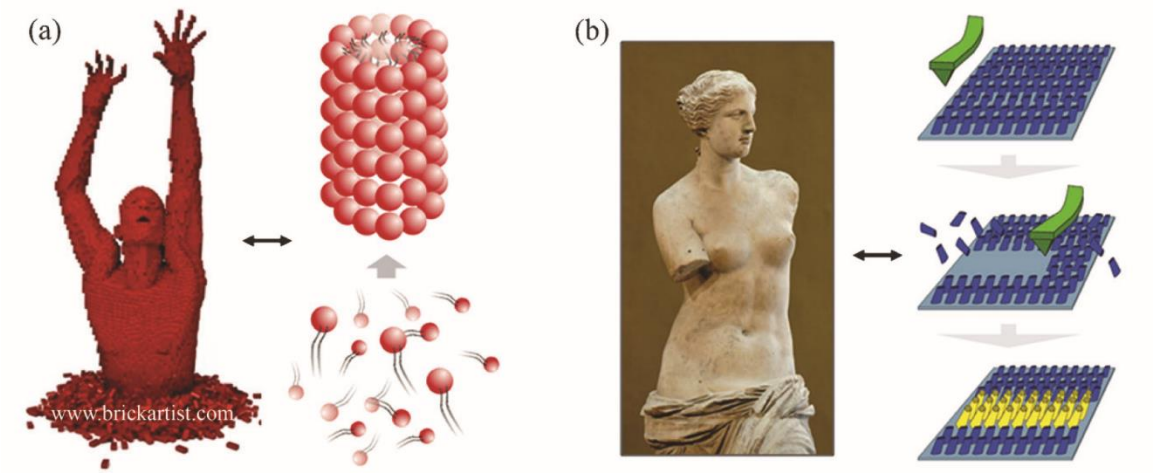

Figure 1.3: Analogies for the production of a statue via bottom-up and top-down fabrication methods: a) Lego pieces can be connected to build a sculpture in a similar fashion that surfactant molecules can self-assemble into micellar structures. b) Marble is sculpted from a larger block to reveal the stone statue within in much the same way that an AFM tip can be used to carve patterns into silicon substrates. Reprinted from Ref. 26 with permission from the RSC.

1.2.1. Bottom-up Assembly

Bottom-up assembly employs small building blocks that self-organize into larger structures. For example, DNA origami nanodevices,[27] liposomes,[28] and metal-organic frameworks[29] are widely used nanomaterials that depend on combining individual components to create synergistic constructs. These assemblies are held together by non-covalent interactions, such as Van der Waals forces, hydrogen bonding, metal coordination, and electrostatic interactions.[30] The non-covalent nature of these interactions give rise to a variety of dynamic assemblies. In particular, the protean surface chemistry of nanomaterials offers a versatile palette to subtly influence biological behaviors at the molecular level.[31]

Rotello *et al.* have developed a variety of sensors based on the selective interactions of surface functionalized gold nanoparticles with biological systems.[32,33] An

unbiased sensor array based on the electrostatic interactions between an anionic fluorescent probe and multiple cationic functionalized gold nanoparticles was developed initially for cancer cell sensing. Complexation with the nanoparticle reversibly quenches the fluorescence of the probe. Following incubation with cells in a 96 well plate, the fluorescence of the probe is regenerated due to competitive binding for the nanoparticle surface (Figure 1.4). This selective response can also be used to differentiate bacteria and bacterial biofilms indicating the generality of this sensing strategy across biological systems.[34,35] These cationic gold nanoparticles have also been shown to reversibly control the catalytic activity of the enzyme β-galactosidase.[36] The complementary electrostatic interactions between the anionic β-galactosidase and the cationic nanoparticles is disrupted in the presence of bacteria generating an enzymatically amplified signal.[37]

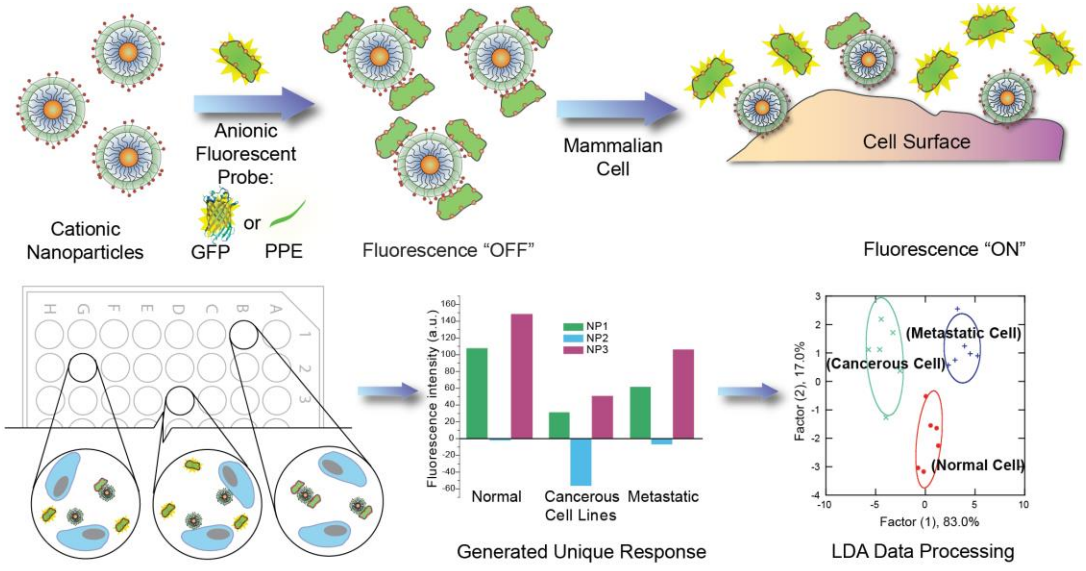

Figure 1.4: Sensor array formed through the self-assembly gold nanoparticles and fluorescent probes. Sample differentiation and classification is accomplished by combining the individual responses from wells each containing differently functionalized nanoparticles and performing statistical analysis to the data. Reprinted from Ref. 38 with permission from Elsevier.

1.2.2. Top-down Assembly

Top-down assembly strategies rely on taking a larger substrate and dividing it into smaller pieces. The smaller components are made through the slicing, etching, or cutting of the raw material. Common top-down nanomanufacturing approaches are inkjet printing,[39] photolithography,[40] dip-pen nanolithography,[41] and nanoimprint lithography.[42] The processing steps transfer a 'master' pattern unto the substrate generating the final structure. The attainable feature sizes and complexities of the patterns is dependent on the resolution of the manufacturing technique used.

Nanoimprint lithography is a particularly promising technique due to its low cost, simplicity, and high-throughput potential.[43] The process, as shown in Figure 1.5, is accomplished by physically deforming a thin polymer film with a patterned mask under high temperature and pressure.[44] The polymer film is reorganized to replicate the nanometer sized features of the mask. The transferred patterned polymer film can be used for a range of fields such as controlled cellular behavior,[45] photonics,[46] and magneto-optics.[47]

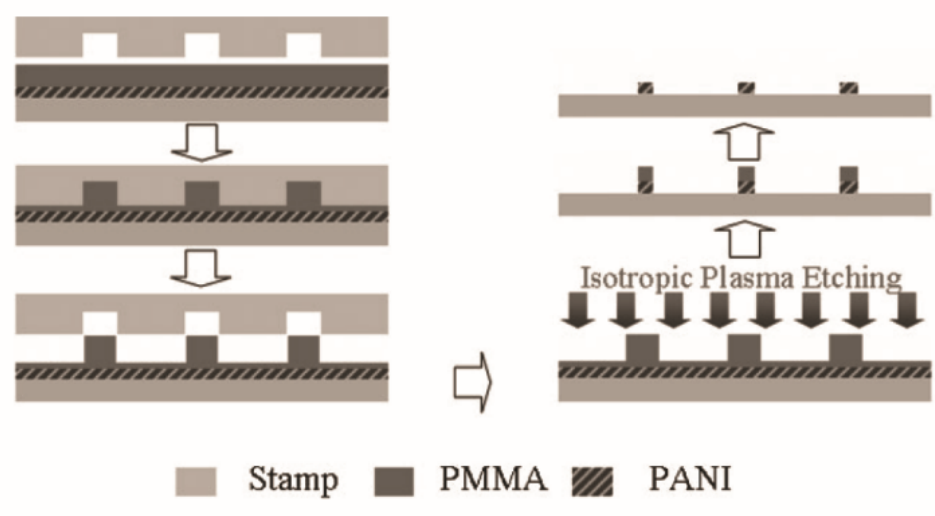

Figure 1.5: Schematic of the NIL process. Reprinted from Ref. 44 with permission from Wiley-VCH Verlag GmbH & Co.

1.3. Protein Film Based Materials

Thin films of proteins are often fabricated through the self-assembly or crosslinking of individual protein molecules. Protein films are widely used in a variety of applications such as artificial organs,[48] drug-releasing patches,[49] and food packaging.[50] Proteins that self-assemble in nature (*e.g.* amyloidogenic,[51] silk proteins,[52] collagen,[53] and fibrinogen[54]) provide particularly attractive scaffolds, combining biodegradability and biocompatibility in materials comprised entirely of natural precursors. The remarkable stability of these proteins is generally attributed to β-sheet rich regions in the peptide backbone that aggregate to form the resultant film. These attributes have made these protein-based materials especially promising materials for interfacing with cells for tissue engineering[55] and wound healing[56] applications. Soy protein scaffolds have been used for tissue regeneration,[57] collagen-based scaffolds have been employed for culturing retinal epithelial cells,[58] and both collagen and chitosan-gelatin scaffolds have been used for making artificial skin.[59] Amyloid-forming proteins likewise provide a useful

platform.[60] For example, Welland's group demonstrated a scalable self-assembly approach to make free-standing films from amyloid protein fibrils.[51] Langer *et al.* have fabricated micropatterned cellular co-cultures by using layer-by-layer deposition of hyaluronic acid and fibronectin (Figure 1.6). This co-culture system allowed researchers to study complicated cell behaviors, including cell-cell communication.[61]

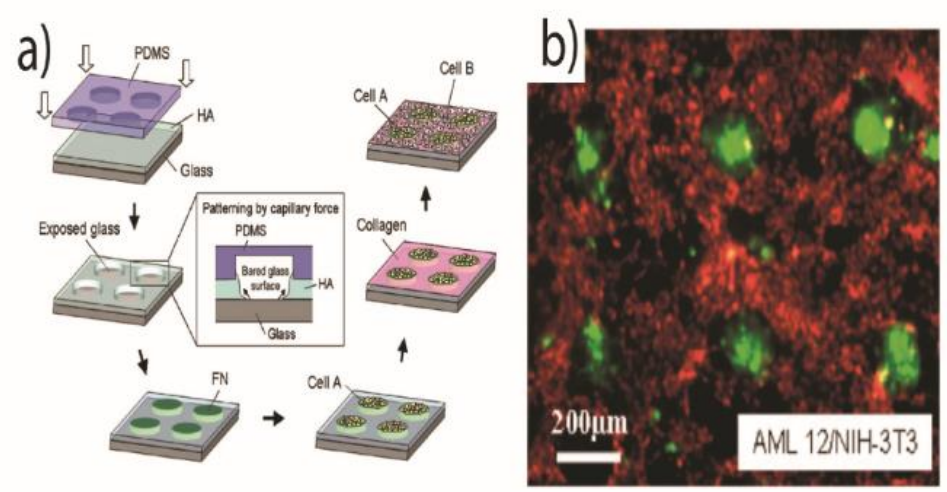

Figure 1.6: a) Co-culture systems were fabricated using capillary force lithography followed by the layer-by-layer deposition of hyaluronic acid and fibronectin. b) Cells were fluorescently stained, AML 12 (green) and NIH-3T3 (red), to show the spatial distribution of each cell type. Reprinted from Ref. 61 with permission from Elsevier.

Outside the small number of self-assembling proteins, most proteins generate films that are not stable under aqueous conditions severely limiting their potential biomaterial applications.[62] One strategy to improve the stability of protein films is to use covalent crosslinkers,[63] including glutaraldehyde,[64] formaldehyde,[65] and glyoxal.[66] However, these treatments can compromise the behavior of the films, and residual free linkers or those released from the hydrolysis of film can cause toxic effects.[67] Alternatively, side chain modification can be used to impart stability to protein films.[68] As shown in Figure 1.7, Chen's group demonstrated that soy proteins modified with

diethoxyphosphoryl groups feature enhanced film stability. UV crosslinking can also be used to stabilize films, though the irreversible chemical modification to the protein that will occur using this process limits the biocompatibility of the film.[69]

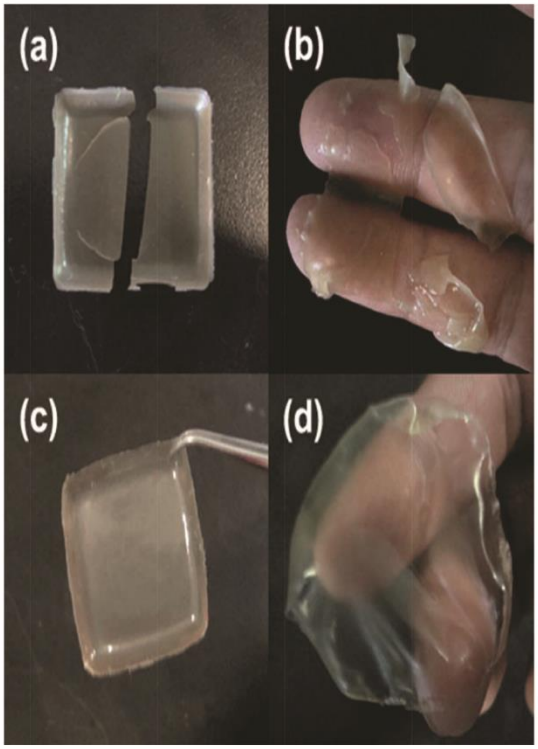

Figure 1.7: Photographs demonstrating the stability of the native soy protein film a), at 50 % humidity and b) in the wet state. Photographs demonstrating the stability of the chemical modified soy protein film c), at 50 % humidity and d) in the wet state. Reprinted from Ref. 68 with permission from the RSC.

Heat curing of proteins is a straightforward technique to generate water-stable films.[70] Many approaches have used elevated temperatures to form soy,[71] amaranth,[72] and whey protein[73] films. However, the temperature of the treatment greatly affects the stability of the protein film, and can lead to unwanted chemical reactions such as the Maillard reaction.[74] In addition, heat curing often results in significantly denatured protein films.[75] Therefore, the development of new methods that could incorporate a

broader set of proteins, without compromising the structural integrity of the protein, would vastly expand the biomaterial potential of films comprised solely of proteins.

1.4. Colloidal Assembly at Liquid/Liquid Interfaces

The boundary between two different phases is a thermodynamically constrained condition. This unstable interface will reorganize the interacting molecules in order to achieve a lower energetic state. Colloidal particles localize at these interfaces, such as between immiscible liquids, to minimize the free energy of overall system. (Figure 1.8a) This phenomenon was first observed by Ramsden[76] and Pickering[77] at the turn of the 20th century and the structures were then identified as "Pickering emulsions." This bottom-up assembly strategy has been used to create a variety of stable structures such as catalysts,[78] drug delivery vehicles,[79] and microreactors.[80] Pieranski demonstrated that this observed stability due to the decreased interfacial energy could be explained with the following equation:[81]

$$\Delta E = \pi r^2 \gamma_{o/w} \times (1 - \cos\theta)^2$$

The major factors in Equation 1 that contribute to minimizing the interfacial energy of colloidal interfaces are the effective radius of the particle (r), the surface tension between the oil and water phases ($\gamma_{o/w}$), and the wettability of the particle surface (*i.e.* contact angle θ of the particle at interface as shown in Figure 1.8b). The greater the diameter of particle used to stabilize the interface, more likely the particle is to resist displacement by thermal fluctuations in the system. This behavior is due to the greater amount of work required to remove a larger particle from the interface and disperse it into the mother liquor than is required for a smaller particle. Adjusting the wettability of the particle through surface functionalization and modification to generate more

amphiphilic particles, ideally a contact angle θ = 90°, can also be used to further improve the stability of the emulsion.[82] Typically, hydrophilic NPs stabilize oil-in-water emulsions and hydrophobic NPs are used to stabilize water-in-oil emulsions.

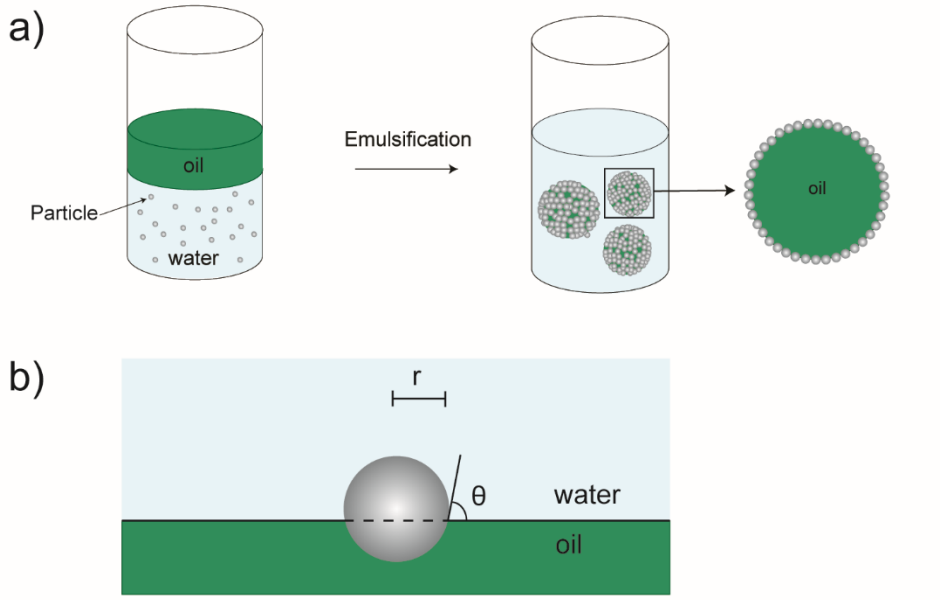

Figure 1.8: Schematic illustration of Pickering emulsions. a) Particles self-assemble at the oil/water interface to form stable emulsions. b) Isotropic particle present at the oil/water interface.

1.5. Dissertation Overview

The research described herein will focus on tuning of the molecular interactions of nanoscale building blocks to create highly versatile systems. Chapter 2 describes the development of a generalized protein film stabilization strategy using nanoimprint lithography. Both processing conditions used during fabrication as well as the structure of the protein precursor were shown to influence the stability and cytophilicity of the resultant films. Chapter 3 expands on the selective mammalian cell adhesion demonstrated by films of the individual proteins by introducing a modular inkjet printing

deposition technique to generate tunable biomaterial surfaces. Chapter 4 describes the development of a supramolecular construct to enhance the human olfactory system beyond our antediluvian limitations. Chapter 5 provides a Pickering emulsion based method to create discrete inorganic-organic microparticles for the retention of hydrophobic payloads. Finally, Chapter 6 discusses the generation of a nanoparticle-stabilized capsule based assembly for treatment of bacterial biofilms.

1.6. References

(1) Dreaden, E. C.; Alkilany, A. M.; Huang, X.; Murphy, C. J.; El-Sayed, M. A. *Chem. Soc. Rev.* **2012**, *41*, 2740.

(2) Lupoi, J. S.; Smith, E. A. *Biotechnol. Bioeng.* **2011**, *108*, 2835.

(3) Bombelli, F. B.; Webster, C. A; Moncrieff, M.; Sherwood, V. *Lancet. Oncol.* **2014**, *15*, e22.

(4) Sim, H. R.; Wark, A. W.; Lee, H. J. *Analyst* **2010**, *135*, 2528.

(5) Pyayt, A. L.; Wiley, B.; Xia, Y.; Chen, A.; Dalton, L. *Nat. Nanotechnol.* **2008**, *3*, 660.

(6) Jiang, Y.; Huo, S.; Mizuhara, T.; Das, R.; Lee, Y.; Hou, S.; Moyano, D. F.; Duncan, B.; Liang, X.; Rotello, V. M. *ACS Nano* **2015**, *9*, 9986.

(7) De, M.; Ghosh, P. S.; Rotello, V. M. *Adv. Mater.* **2008**, *20*, 4225.

(8) Scholl, J. A.; Koh, A. L.; Dionne, J. A. *Nature* **2012**, *483*, 421.

(9) Prabhakar, U.; Maeda, H.; Jain, R. K.; Sevick-Muraca, E. M.; Zamboni, W.; Farokhzad, O. C.; Barry, S. T.; Gabizon, A.; Grodzinski, P.; Blakey, D. C. *Cancer Res.* **2013**, *73*, 2412.

(10) Park, J.; Lee, E.; Hwang, N.-M.; Kang, M.; Kim, S. C.; Hwang, Y.; Park, J.-G.; Noh, H.-J.; Kim, J.-Y.; Park, J.-H.; Hyeon, T. *Angew. Chemie Int. Ed.* **2005**, *44*, 2872.

(11) Duncan, B.; Kim, C.; Rotello, V. M. *J. Control. Release* **2010**, *148*, 122.

(12) Kim, C. S.; Le, N. D. B.; Xing, Y.; Yan, B.; Tonga, G. Y.; Kim, C.; Vachet, R. W.; Rotello, V. M. *Adv. Healthc. Mater.* **2014**, *3*, 1200.

(13) Macfarlane, R. J.; Jones, M. R.; Senesi, A. J.; Young, K. L.; Lee, B.; Wu, J.; Mirkin, C. A. *Angew. Chem. Int. Ed. Engl.* **2010**, *49*, 4589.

(14) Banerjee, I.; Pangule, R. C.; Kane, R. S. *Adv. Mater.* **2011**, *23*, 690.

(15) Atwater, H. A; Polman, A. *Nat. Mater.* **2010**, *9*, 205.

(16) Tokarev, I.; Minko, S. *Soft Matter* **2012**, *8*, 5980.

(17) Sun, T.; Qing, G.; Su, B.; Jiang, L. *Chem. Soc. Rev.* **2011**, *40*, 2909.

(18) Hammond, P. T. *AIChE J.* **2015**, *61*, 1106.

(19) Richardson, J. J.; Bjornmalm, M.; Caruso, F. *Science.* **2015**, *348*, aaa2491.

(20) Sakakibara, K.; Hill, J. P.; Ariga, K. *Small* **2011**, *7*, 1288.

(21) Such, G. K.; Johnston, A. P. R.; Caruso, F. *Chem. Soc. Rev.* **2011**, *40*, 19.

(22) Jiang, S.; Cao, Z. *Adv. Mater.* **2010**, *22*, 920.

(23) Gil, E. S.; Panilaitis, B.; Bellas, E.; Kaplan, D. L. *Adv. Healthc. Mater.* **2013**, *2*, 206.

(24) Shah, N. J.; Hong, J.; Hyder, M. N.; Hammond, P. T. *Adv. Mater.* **2012**, *24*, 1445.

(25) Shah, N. J.; Hyder, M. N.; Moskowitz, J. S.; Quadir, M. A.; Morton, S. W.; Seeherman, H. J.; Padera, R. F.; Spector, M.; Hammond, P. T. *Sci. Transl. Med.* **2013**, *5*, 191ra83.

(26) Smith, K. H.; Tejeda-Montes, E.; Poch, M.; Mata, A. *Chem. Soc. Rev.* **2011**, *40*, 4563.

(27) Pinheiro, A. V.; Han, D.; Shih, W. M.; Yan, H. *Nat. Nanotechnol.* **2011**, *6*, 763.

(28) Johnston, A. P. R.; Such, G. K.; Ng, S. L.; Caruso, F. *Curr. Opin. Colloid Interface Sci.* **2011**, *16*, 171.

(29) Ameloot, R.; Vermoortele, F.; Vanhove, W.; Roeffaers, M. B. J.; Sels, B. F.; De Vos, D. E. *Nat. Chem.* **2011**, *3*, 382.

(30) Mann, S. *Nat. Mater.* **2009**, *8*, 781.

(31) Tang, R.; Moyano, D. F.; Subramani, C.; Yan, B.; Jeoung, E.; Tonga, G. Y.; Duncan, B.; Yeh, Y.-C.; Jiang, Z.; Kim, C.; Rotello, V. M. *Adv. Mater.* **2014**, *26*, 3310.

(32) Rana, S.; Le, N. D. B.; Mout, R.; Duncan, B.; Elci, S. G.; Saha, K.; Rotello, V. M. *ACS Cent. Sci.* **2015**, *1*, 191.

(33) Miranda, O. R.; Creran, B.; Rotello, V. M. *Curr. Opin. Chem. Biol.* **2010**, *14*, 728.

(34) Phillips, R. L.; Miranda, O. R.; You, C.-C.; Rotello, V. M.; Bunz, U. H. F. *Angew. Chemie Int. Ed.* **2008**, *47*, 2590.

(35) Li, X.; Kong, H.; Mout, R.; Saha, K.; Moyano, D. F.; Robinson, S. M.; Rana, S.; Zhang, X.; Riley, M. A.; Rotello, V. M. *ACS Nano* **2014**.

(36) Miranda, O. R.; Li, X.; Garcia-Gonzalez, L.; Zhu, Z.; Yan, B.; Bunz, U. H. F.; Rotello, V. M. *J. Am. Chem. Soc.* **2011**, *133*, 9650.

(37) Creran, B.; Li, X.; Duncan, B.; Kim, C. S.; Moyano, D. F.; Rotello, V. M. *ACS Appl. Mater. Interfaces* **2014**, *6*, 19525.

(38) Duncan, B.; Elci, S. G.; Rotello, V. M. *Nano Today* **2012**, *7*, 228.

(39) Delaney, J. T.; Smith, P. J.; Schubert, U. S. *Soft Matter* **2009**, *5*, 4866.

(40) Subramani, C.; Yu, X.; Agasti, S. S.; Duncan, B.; Eymur, S.; Tonga, M.; Rotello, V. M. *J. Mater. Chem.* **2011**, *21*, 14156.

(41) Lee, K.-B.; Park, S.-J.; Mirkin, C. A.; Smith, J. C.; Mrksich, M. *Science* **2002**, *295*, 1702.

(42) Fredin, N. J.; Broderick, A. H.; Buck, M. E.; Lynn, D. M. *Biomacromolecules* **2(009**, *10*, 994.

(43) Ahn, S. H.; Guo, L. J. *ACS Nano* **2009**, *3*, 2304.

(44) Huang, C.; Dong, B.; Lu, N.; Yang, B.; Gao, L.; Tian, L.; Qi, D.; Wu, Q.; Chi, L. *Small* **2009**, *5*, 583.

(45) Subramani, C.; Saha, K.; Creran, B.; Bajaj, A.; Moyano, D. F.; Wang, H.; Rotello, V. M. *Small* **2012**, *8*, 1209.

(46) Amsden, J. J.; Domachuk, P.; Gopinath, A.; White, R. D.; Negro, L. D.; Kaplan, D. L.; Omenetto, F. G. *Adv. Mater.* **2010**, *22*, 1746.

(47) González-Díaz, J. B.; García-Martín, A.; Armelles, G.; Navas, D.; Vázquez, M.; Nielsch, K.; Wehrspohn, R. B.; Gösele, U. *Adv. Mater.* **2007**, *19*, 2643.

(48) Choi, Y. S.; Hong, S. R.; Lee, Y. M.; Song, K. W.; Park, M. H.; Nam, Y. S. *Biomaterials* **1999**, *20*, 409.

(49) Hofmann, S.; Wong Po Foo, C. T.; Rossetti, F.; Textor, M.; Vunjak-Novakovic, G.; Kaplan, D. L.; Merkle, H. P.; Meinel, L. *J. Control. Release* **2006**, *111*, 219.

(50) Rhim, J. W.; Park, H. M.; Ha, C. S. *Prog. Polym. Sci.* **2013**, *38*, 1629.

(51) Knowles, T. P. J.; Oppenheim, T. W.; Buell, A. K.; Chirgadze, D. Y.; Welland, M. E. *Nat. Nanotechnol.* **2010**, *5*, 204.

(52) Altman, G. H.; Diaz, F.; Jakuba, C.; Calabro, T.; Horan, R. L.; Chen, J.; Lu, H.; Richmond, J.; Kaplan, D. L. *Biomaterials* **2003**, *24*, 401.

(53) Roberts, M. J.; Bhatt, N.; Voge, C. M.; Meshot, E. R.; Stegemann, J. P.; Hart, A. J. *J. Mater. Chem. B* **2013**, *1*, 4711.

(54) Yermolenko, I. S.; Gorkun, O. V; Fuhrmann, A.; Podolnikova, N. P.; Lishko, V. K.; Oshkadyerov, S. P.; Lord, S. T.; Ros, R.; Ugarova, T. P. *J. Biol. Chem.* **2012**, *287*, 41979.

(55) Zhao, Y.; Jiang, Q.; Xu, H.; Reddy, N.; Xu, L.; Yang, Y. *J. Biomed. Mater. Res. - Part B Appl. Biomater.* **2014**, *102*, 729.

(56) Peles, Z.; Binderman, I.; Berdicevsky, I.; Zilberman, M. *J. Tissue Eng. Regen. Med.* **2013**, *7*, 401.

(57) Chien, K. B.; Shah, R. N. *Acta Biomater.* **2012**, *8*, 694.

(58) Lu, J. T.; Lee, C. J.; Bent, S. F.; Fishman, H. A.; Sabelman, E. E. *Biomaterials* **2007**, *28*, 1486.

(59) Mao, J.; Zhao, L.; de Yao, K.; Shang, Q.; Yang, G.; Cao, Y. *J. Biomed. Mater. Res.* **2003**, *64A*, 301.

(60) Meier, C.; Welland, M. E. *Biomacromolecules* **2011**, *12*, 3453.

(61) Fukuda, J.; Khademhosseini, A.; Yeh, J.; Eng, G.; Cheng, J.; Farokhzad, O. C.; Langer, R. *Biomaterials* **2006**, *27*, 1479.

(62) Reddy, N.; Tan, Y.; Li, Y.; Yang, Y. *Macromol. Mater. Eng.* **2008**, *293*, 614.

(63) Gennadios, A. (Ed.). "*Protein-based films and coatings"*, CRC Press, 2002.

(64) Park, S. K.; Bae, D. H.; Rhee, K. C. *J. Am. Oil Chem. Soc.* **2000**, *77*, 879.

(65) Marquié, C. *J. Agric. Food Chem.* **2001**, *49*, 4676.

(66) Vaz, C. M.; De Graaf, L. a; Reis, R. L.; Cunha, A. M. *J. Mater. Sci. Mater. Med.* **2003**, *14*, 789.

(67) Matsuda, S.; Iwata, H.; Se, N.; Ikada, Y. *J. Biomed. Mater. Res.* **1999**, *45*, 20.

(68) Ma, L.; Yang, Y.; Yao, J.; Shao, Z.; Chen, X. *Polym. Chem.* **2013**, *4*, 5425.

(69) Rhim, J. W.; Gennadios, A.; Fu, D.; Weller, C. L.; Hanna, M. a. *LWT - Food Sci. Technol.* **1999**, *32*, 129.

(70) Zhang, H.; Mittal, G. *Environ. Prog. Sustain. Energy* **2010**, *29*, 203.

(71) Cao, N.; Fu, Y.; He, J. *Food Hydrocoll.* **2007**, *21*, 1153.

(72) Condés, M. C.; Añón, M. C.; Mauri, A. N. *J. Food Eng.* **2013**, *119*, 573.

(73) Amin, S.; Ustunol, Z. *Int. J. Dairy Technol.* **2007**, *60*, 149.

(74) Hernández-Muñoz, P.; Villalobos, R.; Chiralt, A. *Food Hydrocoll.* **2004**, *18*, 647.

(75) Rangavajhyala, N.; Ghorpade, V.; Hanna, M. *J. Agric. Food Chem.* **1997**, *45*, 4204.

(76) Ramsden, W. *Proc. R. Soc. London* **1903**, *72*, 156.

(77) Pickering, S. U. *J. Chem. Soc. Trans.* **1907**, *91*, 2001.

(78) Jeong, Y.; Duncan, B.; Park, M.-H.; Kim, C.; Rotello, V. M. *Chem. Commun. (Camb).* **2011**, *47*, 12077.

(79) Yang, X.-C.; Samanta, B.; Agasti, S. S.; Jeong, Y.; Zhu, Z.-J.; Rana, S.; Miranda, O. R.; Rotello, V. M. *Angew. Chemie Int. Ed.* **2011**, *50*, 477.

(80) Yang, H.; Fu, L.; Wei, L.; Liang, J.; Binks, B. P. *J. Am. Chem. Soc.* **2015**, *137*, 1362.

(81) Pieranski, P. *Phys. Rev. Lett.* **1980**, *45*, 569.

(82) Binks, B. P.; Lumsdon, S. O. *Langmuir* **2000**, *16*, 8622.

CHAPTER 2

ROBUST PROTEIN FILMS GENERATED VIA NANOIMPRINT LITHOGRAPHY

2.1. Introduction

Protein-based materials provide a uniquely biocompatible and sustainable platform for the generation of functional materials.[1,2,3,4] The intrinsic structural and functional diversity inherent to proteins make them highly versatile building blocks.[5] Prior research has harnessed the innate biocompatibility of protein films for applications as diverse as bioelectronics,[14] tissue engineering,[10,11,16] and drug delivery.[13,15] Proteins also possess aqueous processability[6] and have minimal environmental impact,[7] making them ideal components for sustainable "green" materials. Translating these characteristics into protein films resistant to aqueous degradation is crucial for most applications such as tissue engineering and controlled drug delivery.[8,9,10,11,12]

Current methods to stabilize protein films use two main strategies: employing a relatively limited range of naturally self-assembling proteins[2,3,4] or using added crosslinkers.[13,14,15,16,17] Naturally-assembling proteins, such as silk fibroin, can be processed into a multitude of biocompatible structures, though post-functionalization is often needed to diversify the surface chemistry of the films.[18] The latter covalent crosslinking strategy generates polymeric complexes from a variety of proteins, however, unreacted additives retained in the crosslinked protein films can adversely affect their final behavior.[18,19,20,21] Therefore an alternative methodology to stabilize protein films would vastly expand the functional toolkit for creating biomaterials.

We demonstrate here a scalable, additive-free nanoimprint lithography (NIL) based method for the fabrication of stable, patterned protein films. This approach is general in terms of protein building block, with the imprinted proteins retaining much of their native structure and hence materials properties. The surface charge of the films can be programmed through choice of protein, as demonstrated though Kelvin probe force microscopy. Simultaneously, the stability and degradability of these materials is controlled through parametric variation of processing temperature and pressure. The ability to utilize these materials properties is highlighted through generation of effective non-fouling surfaces and tuning of cellular adhesion through choice of protein precursor.

2.2.Results and Discussion

We hypothesized that the combination of temperature and pressure provided using thermal NIL could be used to create stable protein films with minimal loss of protein structure, and without the use of additives. This NIL-based strategy for generating protein films would allow us to greatly expand the range of protein building blocks from the subset of naturally self-assembling proteins to the full range of readily available proteins. Importantly, retention of protein structure in the NIL process would provide effective translation of protein properties, such as surface charge, to the macroscopic properties of the films. These hypotheses were tested using three readily available proteins that do not natively self-assemble: anionic bovine serum albumin (BSA, MW 66.3 kDa, pI 4.8), neutral hemoglobin (Hemo, MW 64.5 kDa, pI 6.8), and cationic lysozyme (Lyso, MW 14.3 kDa, pI 11).

Precursor protein films were generated by spin-casting 10 % w/w aqueous solutions of protein onto plasma cleaned substrates (Figure 2.1a). The films were ~200

nm in thickness as determined by ellipsometry and atomic force microscopy (Figure 2.2). The spin-cast films were next imprinted/embossed by using a fluorosilane-functionalized mold. The NIL conditions were parametrically varied to identify the factors that determine the aqueous stability of the imprinted protein films (Figure 2.1b); the results demonstrate that both pressure and heat are required for generating stable protein films, a synergistic behavior that had not been previously probed. Stable films were generated from all three proteins at temperatures greater than 140 °C and pressures of 2.8 MPa, with variation observed in the pressure/temperature profile of the individual protein, a natural consequence of the dramatically differing structures of the precursor proteins.

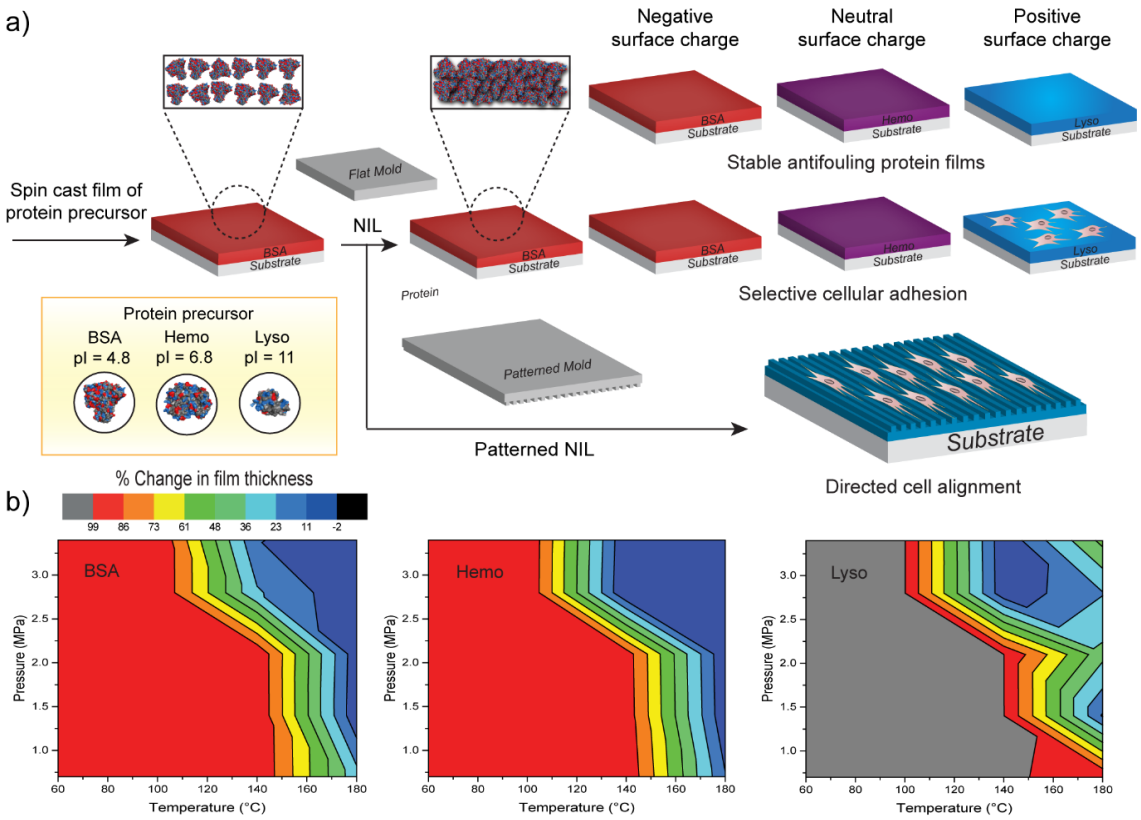

Figure 2.1: Method and optimized conditions used for imprinted protein film fabrication. a) Proteins were spin-cast and then imprinted/embossed using temperature and pressure to generate stable planar and patterned surfaces. These surfaces retain properties of the precursor proteins that can be employed for a range of applications. b) Plots showing the effect of pressure and temperature on film stability in water. Films were washed for 1 min with water and the thickness measured by ellipsometry after drying, with water stability observed only when heat and pressure are combined.

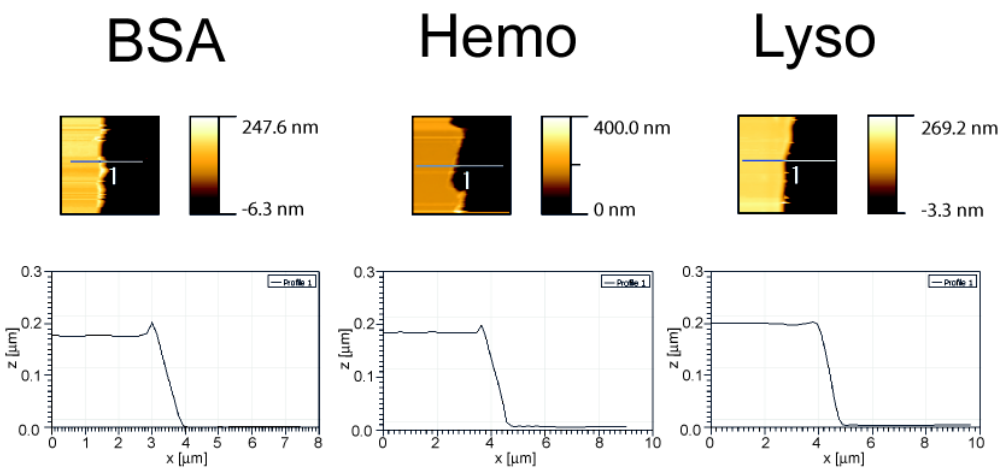

Figure 2.2: AFM images and cross-sections of scratched protein films. The protein films made by BSA, Hemo, and Lyso were scratched by blade and the film thicknesses were determined by measuring the height differences made by scratching.

The secondary protein structure of the components within the films was characterized using circular dichroism (CD) spectroscopy.[22] (Figure 2.3a-c) The substantial retention of secondary structure indicates that a more subtle mechanism of film stabilization than complete denaturation is operative. We hypothesize that the elevated temperature of the nanoimprinter causes flexibility of the random coil segments of the peptide backbone, while the pressure limits conformational reorganization of the protein structure. The origin of the film stability was probed through use of traditional protein denaturants. Treatment of the films with 2-mercaptoethanol did not disrupt the films, ruling out inter-protein disulfide bonds as the stabilizing factor.[23] In contrast, treatment with a surfactant (sodium dodecyl sulfate, SDS) rapidly disrupted the films, indicating that inter-protein hydrophobic interactions imparts the observed stability of the film to aqueous media.[24] (Figure 2.4)

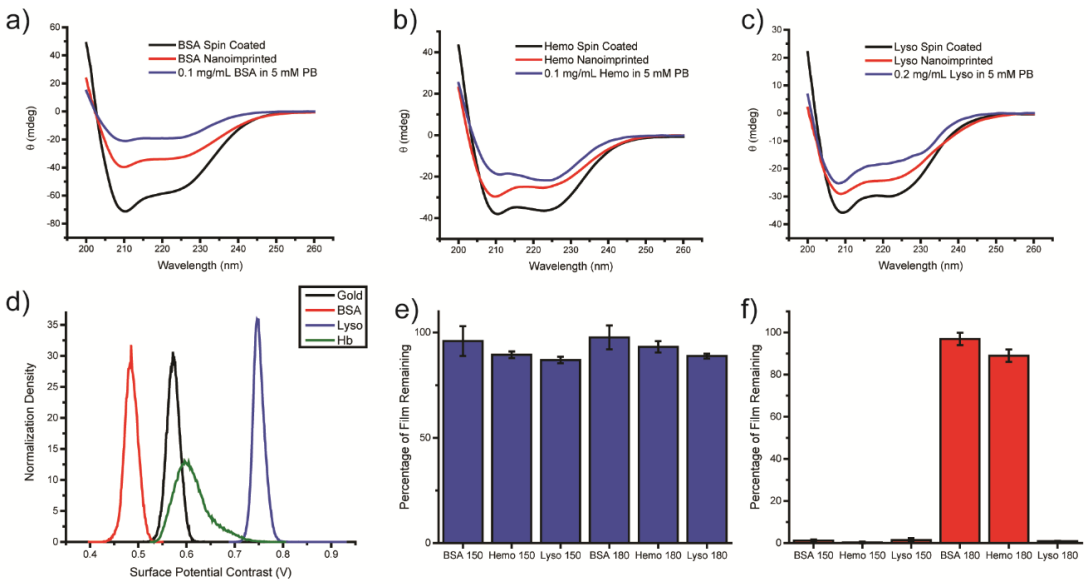

Figure 2.3: Structural characterization of protein films a) CD spectra of BSA. b) CD spectra of Hemo. c) CD spectra of Lyso. The individual proteins in phosphate buffer are also shown for comparison. d) Surface potential of individual protein films as determined by Kelvin probe force microscopy (KPFM). e) Thickness change in protein films measured by ellipsometry after 48 hrs of incubation in 10 % serum solution. f) Thickness change in protein films measured by ellipsometry after 24 hrs of incubation in 0.01 % trypsin solution.

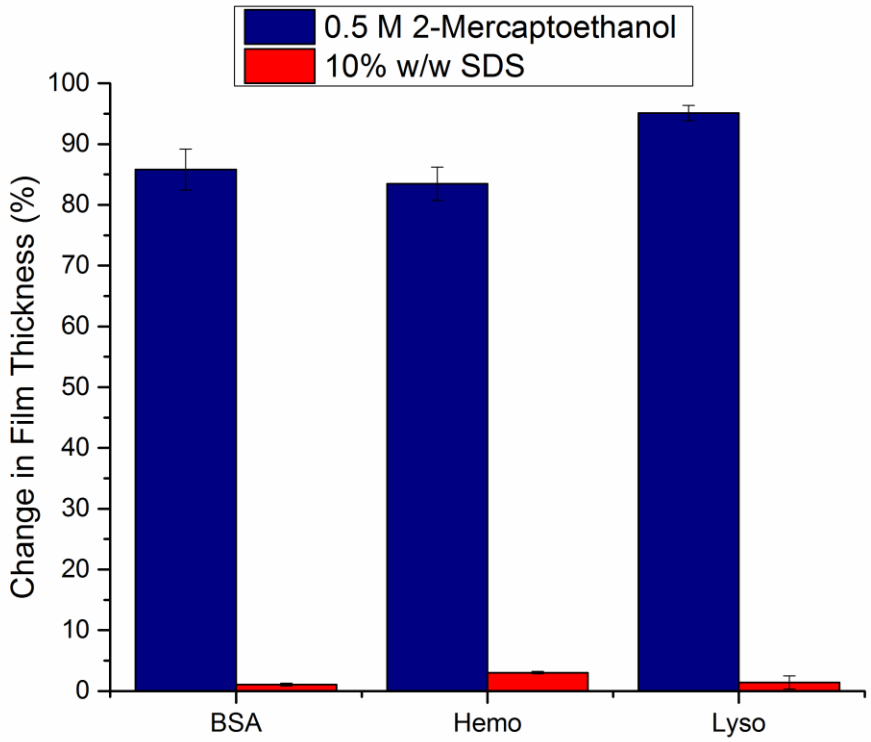

Figure 2.4: Thickness changes of protein films after incubating with 0.5 M 2-mercaptoethanol (2-ME) and 10% sodium dodecyl sulfate (SDS) for 48 hours. The thickness was measured by ellipsometry and the percentage changes were calculated by comparing the thicknesses of protein films before and after treating with 2-ME or SDS. SDS was used for disrupting hydrophobic interaction and 2-ME was able to break disulfide bonds of protein films. The results indicated that the protein films were stabilized mainly by hydrophobic interactions.

The retention of protein structure in the imprinted films implied that the choice of protein could be used to dictate the charge of the resulting macroscopic films, an important tool for numerous applications. Kelvin probe force microscopy (KPFM) [25] was used to measure the local work function difference between the metallized probe (Pt) and the protein surfaces.[26] Figure 2.3d (along with Figure 2.5) shows histograms of measured surface potential contrast (SPC) relative to the evaporated gold supporting substrate. As expected based on precursor protein charge, the BSA surfaces present a negative surface

potential, while the Lyso film possesses a positive surface potential. Hemo showed a near neutral potential, consistent with its near neutral pI. The retention of charge was further probed through charge-selective adhesion of positively and negatively charged quantum dots (Figure 2.6), supporting that the surface charge differences established by KPFM translate into functional control of adhesion.

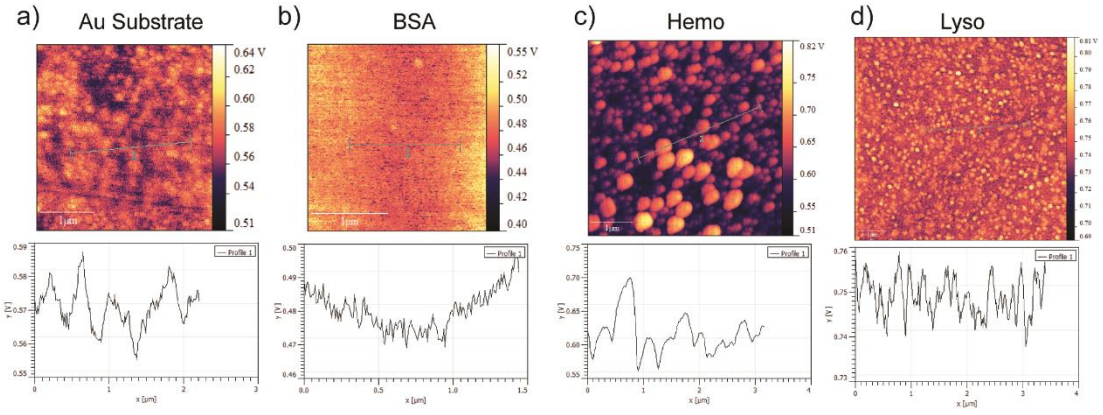

Figure 2.5: Kelvin probe force microscopy analysis of the protein films. a) Surface potential contrast measurement of gold substrate. Below is the line section profile. b) Surface potential contrast measurement bovine serum albumin. Below is the line section profile. c) Surface potential contrast measurement of hemoglobin. Below is the line section profile. d) Surface potential contrast measurement of lysozyme. Below is the line section profile.

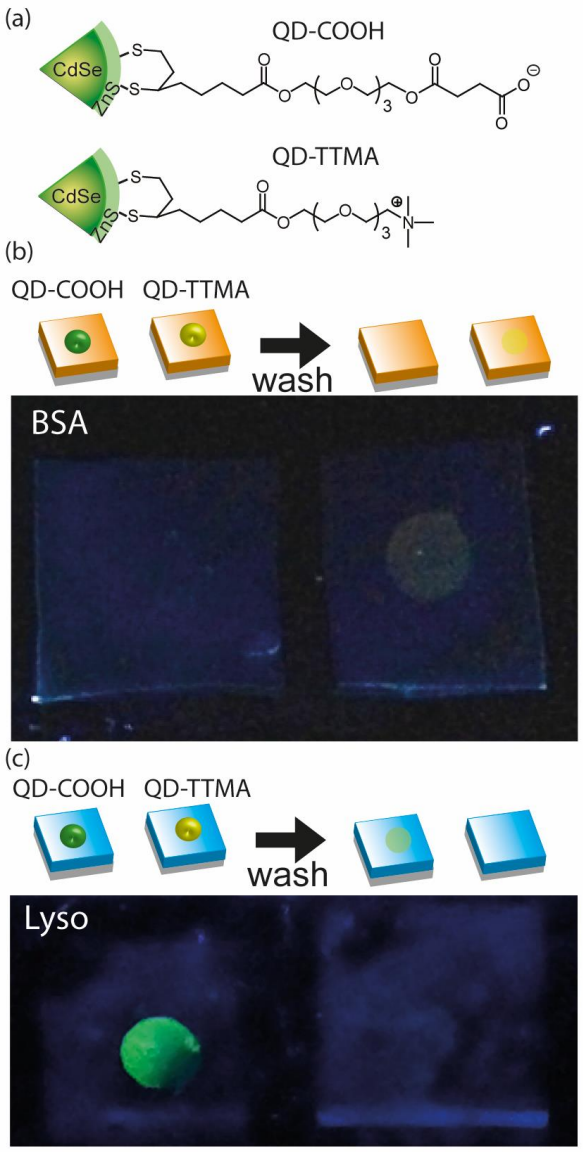

Figure 2.6: Adhesion of functionalized quantum dots (QDs) to protein films. a) The chemical structures of surface functionalities on QDs. The charged QDs were used as probes for the surface charges of protein films by interacting with protein films through electrostatic interaction. b,c) 10 µL 1 µM QD probes were dropped on the protein films and incubated for 15 mins in a humid chamber to avoid drying. After incubation, the protein films were washed by Milli-Q water 5 times. Then the surface charges of protein films were determined by the fluorescent responses under the irradiation of a UV lamp at 365 nm. For the BSA film, only the positively charged probe showed a strong interaction, indicating that BSA film is negatively charged. The Lyso film showed the opposite result due to its inherent positive charge.

We next focused on biomaterial applications for these NIL protein films. The inherently zwitterionic surfaces of soluble proteins is essential in inhibiting their aggregation in solution.[1] The retention of surface properties should therefore provide resistance to protein fouling, an important requirement for both implantable devices and for *ex vivo* applications.[27,28] We evaluated resistance to protein deposition of our films by incubating films in 10 % serum solutions for 48 hrs and then measuring the film thicknesses by ellipsometry. As shown in Figure 2.3e, there were no significant increases in film thicknesses, indicating that the films are resist non-specific protein adsorption. We further tested the response of the films to the intracellular protease trypsin, as controlled degradation of scaffolding plays an important role in interfacing materials with biological systems.[12,14] After incubating in 0.01 % w/w trypsin solution for 24 hrs, BSA and Hemo films fabricated at 180 °C were resistant to trypsin hydrolysis. All films imprinted at 150 °C, however, were degraded (Figure 2.3f), making these films promising candidates for controlled-release applications.[29]

Previous studies have demonstrated that charged molecules on surfaces are important for directing cellular adhesion, with more efficient attachment observed with positively charged surfaces.[30] Based on our ability to control the surface charge of the imprinted protein films, functional demonstration of the differences in film properties was obtained through cell adhesion studies. NIH-3T3 fibroblast cells were seeded onto protein films for 48 hrs and stained with calcein-AM. Fluorescence microscopy images show that films made from negatively charged BSA and neutral Hemo cells had limited adhesion on films fabricated at 150 °C (Figure 2.7a) while the films fabricated at 180 °C (Figure 2.7b) demonstrated no measurable adhesion. In contrast, Lyso films provided

excellent adhesion at both processing temperatures, consistent with the expected higher cellular adhesion by the cationic surface.[30]

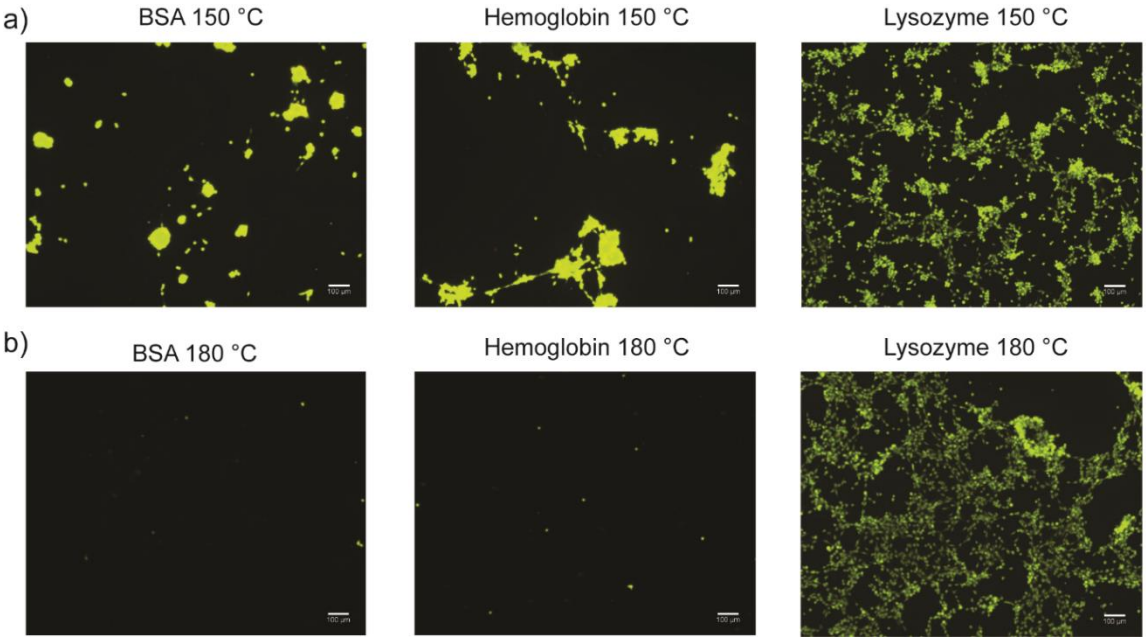

Figure 2.7: Cellular adhesion to protein films. Adhered cells on protein films generated at a) 150 °C and b) 180 °C were stained with calcein-AM after 48 hrs. Scale bars represent 100 µm.

The NIL process used in our method provides direct access to nanoscale patterning that can be used to dictate cellular alignment, a feature that subsequently can be translated into tissue formation.[30] Based on the cellular adhesion studies, Lyso was chosen to investigate cell alignment based on nanopatterning. As shown in Figure 2.8a inset and Figure 2.9a, the Lyso film was texturally patterned using a fluorosilane-functionalized master mold with a 300 nm grooved pattern. Next, NIH-3T3 fibroblast cells were cultured onto the patterned film. As shown in Figure 2.8b and Figure 2.9b, cells were fixed, stained with phalloidin to visualize actin filaments, and alignments were measured by optical microscopy. Figure 2.8a shows that a majority of the cells aligned

with the nanoscale pattern, demonstrating that the film properties and patterning provided by the NIL process can be used synergystically to direct cellular growth.

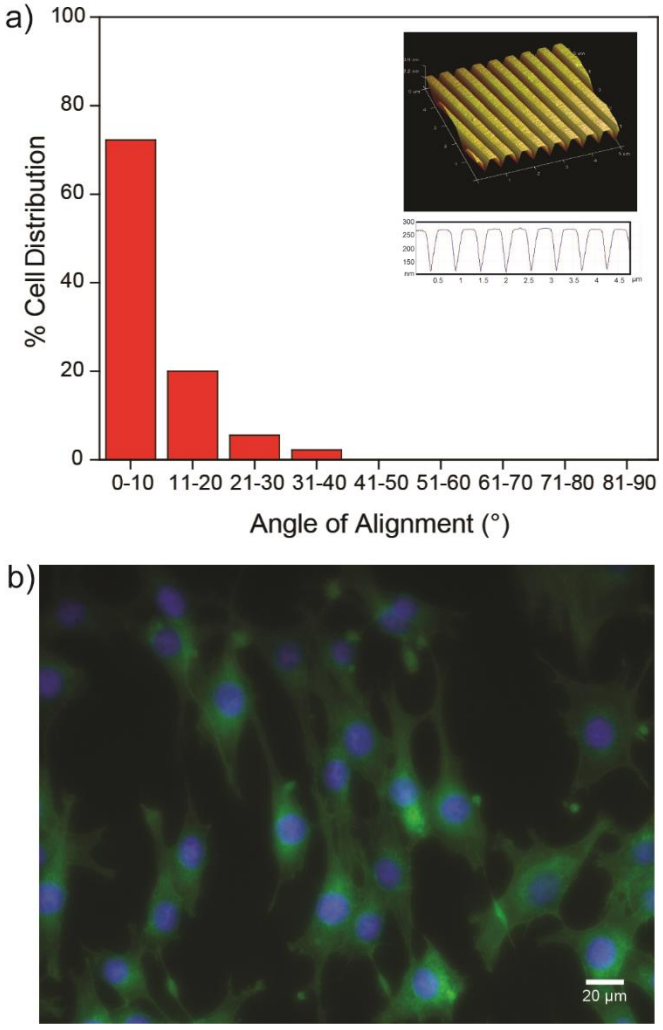

Figure 2.8: Cellular adhesion and alignment with patterned surfaces. **a)** Percentage of cells aligned along the imprinted pattern. Inset is a 3D atomic force microscopy image of the Lyso film generated with a patterned mold. **b)** Fluorescence micrograph of fibroblast cells cultured on the patterned Lyso film. Cell nuclei were stained with Hoechst 33342 and actin filaments were stained with phalloidin.

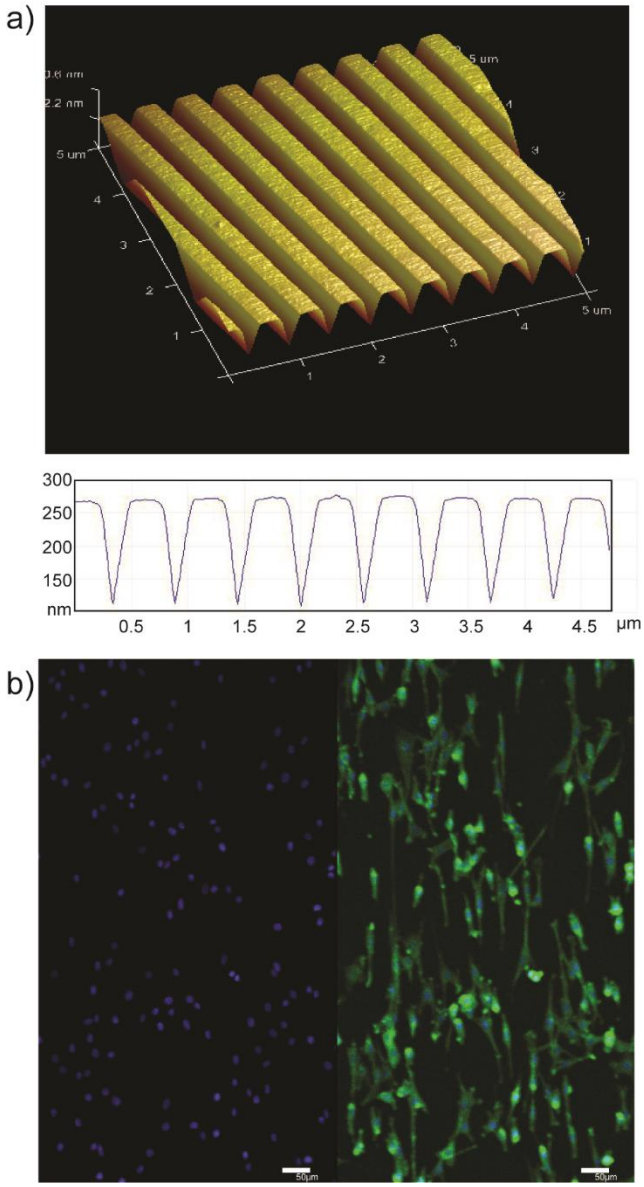

Figure 2.9: Cell culture adhesion and cellular alignment with patterned surfaces. **a)** 3D atomic force microscopy image of the lysozyme film generated with a patterned mold. **b)** Fluorescence micrograph of fibroblast cells cultured on the patterned lysozyme film. Hoechst (left) was used to stain cell nuclei and phalloidin (right) to stain actin filaments. Scale bars are 50 µm.

2.3. Conclusions

In summary, we have demonstrated that the controlled heat and pressure provided by thermal NIL generates water-stable films from a range of precursor proteins. These films are generated without additives and in an environmentally benign fashion. The

proteins retain substantial native protein structure, which renders them biocompatible and resistant to protein fouling. The films also integrate the intrinsic physical properties of the precursor proteins, allowing surface charge and stability to be tuned by choice of precursor protein and processing conditions. This bottom-up method is generalizable, indicating it can use the enormous variety of naturally occurring and engineered proteins to generate films with a commensurate range of properties. Furthermore, the readily scalable NIL based method is multimodal, as the process both influences the stability of the films and introduces nanoscale architectural features. Taken together, the ability to generate stable protein films using NIL provides an enabling technology for a broad range of applications ranging from biomedicine to sustainable consumer materials.

2.4. Experimental Methods

2.4.1. Materials

BSA, Hemo, and Lyso were purchased from Fisher Scientific and used without further purification. Silica wafers were purchased from WRS Materials. Quartz microscopy slides were purchased from Electron Microscopy Sciences. MilliQ water was purified by using a Millipore water purification system.

2.4.2. Film Preparation

10 % w/w solutions of protein in MilliQ water were filtered by using a 0.22 μm filter and spin-coated at 3000 rpm for 60 s onto an oxygen plasma cleaned silicon substrate, yielding a thin film of protein.

2.4.3. Nanoimprint Lithography (NIL)

Nanoimprinting of protein films was performed by using a Nanonex NX-2000 nanoimprinter with silicon molds. Imprinting was performed at various temperatures and

pressures for 5 min. A silicon NIL mold (line width 303 nm, period 606 nm, and groove depth 190 nm) from Lightsmyth Technologies was used in the cell patterning. All molds were treated with heptadecafluoro-1,1,2,2-(tetrahydrodecyl)dimethyl- chlorosilane at 75 °C for 2 days in a vacuum chamber.

2.4.4. Kelvin Probe Force Microscopy (KPFM)

10 % w/w solutions of protein in MilliQ water were filtered using a 0.22 µm filter and dropcast onto an oxygen plasma cleaned gold substrate, yielding a thin film of protein. Nanoimprinting of the protein films was performed by using a Nanonex NX-2000 nanoimprinter with flat silicon molds at 180 °C and 2.8 MPa. The KPFM was conducted with platinum coated tips (ANSCM-PA) purchased from AppNano on a Digital Instrument atomic force microscope under ambient temperature and atmospheric conditions.

2.4.5. Cell Culture

Mouse fibroblast cells 3T3 (ATCC CRL-1658) were cultured in Dulbecco's modified Eagle's medium (DMEM; ATCC 30-2002) supplemented with 10% bovine calf serum (ATCC 30-2030) and 1 % antibiotics in T75 flasks. Cells were maintained at 37 °C in a humidified atmosphere of 5 % CO_2 and were sub-cultured once in 4 days.

2.4.6. Cell Adhesion

3T3 cells grown in T75 flasks were washed with phosphate buffered saline (PBS), trypsinized with 1X trypsin and collected in DMEM media. Cells were centrifuged and were re-suspended in fresh DMEM media and counted by using a hemocytometer. Protein film coated surfaces were placed in a six-well plate where 3T3 cells were added to each well (100000 cells/well) and incubated for 48 h at 37 °C in a humidified

atmosphere of 5 % CO_2. Following incubation, cells were washed with phosphate-buffered saline (PBS) three times and incubated with calcein AM (Biotium Inc, 80011-2) and propidium iodide (Invitrogen) in PBS (final concentration 3 μM each) for 30 min. Fluorescence microscopy images were taken by using an Olympus IX51 microscope to visualize the adhered live (Calcein AM stained, green) and dead cell (propidium iodide stained, red) population in each surface.

2.4.7. Cell Alignment on Nano-patterned Surfaces

The cell alignment on the patterned surfaces were performed according to previously published procedures.[30] Briefly, 100000 cells were incubated with the nano-patterned surface for 48 h and washed twice with pre-warmed PBS and fixed with 3.7 % methanol-free formaldehyde solution (Electron Microscopy Sciences 15714-S). Cells were then washed three times with PBS and extracted with 0.1 % Triton X-100 in PBS for 5 min. Surfaces were then washed with PBS and incubated with a solution of Oregon Green 488 phalloidin (Invitrogen O7466) to stain actin filaments and Hoechst nuclear stain (Invitrogen H1399) at final concentrations of 200 nM and 1 μg/mL respectively in PBS. After 30 minutes, the cells were washed three times and the images were captured using a confocal microscope (Olympus). Cell alignment was measured by using ImageJ software by determining the angle of the long axis of the nucleus with respect to the parallel direction of the pattern. 45 random cells from each image were counted according to their angle of alignment from 0 ° to 90 ° in 10 ° increments and their percentage distribution was graphed.

2.4.8. Characterization

Bright field images and fluorescence were detected by using an Olympus IX51 microscope with excitation wavelengths of 470 nm and 535 nm. AFM imaging of the surfaces was done on a Dimensions 3000 (Veeco) in tapping mode using a RTESP7 tip (Veeco). Confocal images were obtained by using a Zeiss LSM 510 Meta microscope. The film thickness of the protein films was measured by a Rudolph Research Auto EL ellipsometer. Far-UV circular dichroism (CD) spectra were measured on a JASCO J-720 spectropolarimeter with a quartz cuvette of 1 mm path length at 25 °C. The spectra were recorded from 200 to 260 nm as an average of three scans at a rate of 20 nm/min.

2.5. References

(1) Smith, K. H.; Tejeda-Montes, E.; Poch, M.; Mata, A. *Chem. Soc. Rev.* **2011**, *40*, 4563.

(2) Kim, S.; Marelli, B.; Brenckle, M. a.; Mitropoulos, A. N.; Gil, E.-S.; Tsioris, K.; Tao, H.; Kaplan, D. L.; Omenetto, F. G. *Nat. Nanotechnol.* **2014**, *9*, 306.

(3) Amsden, J. J.; Domachuk, P.; Gopinath, A.; White, R. D.; Negro, L. D.; Kaplan, D. L.; Omenetto, F. G. *Adv. Mater.* **2010**, *22*, 1746.

(4) Hu, X.; Cebe, P.; Weiss, A. S.; Omenetto, F.; Kaplan, D. L. *Mater. Today* **2012**, *15*, 208.

(5) A. Gennadios, *Protein-Based Films and Coatings*, CRC Press, **2002**.

(6) Omenetto, F. G.; Kaplan, D. L. *Science* **2010**, *329*, 528.

(7) Perry, H.; Gopinath, A.; Kaplan, D. L.; Negro, L. D.; Omenetto, F. G. *Adv. Mater.* **2008**, *20*, 3070.

(8) Rhim, J. W.; Park, H. M.; Ha, C. S. *Prog. Polym. Sci.* **2013**, *38*, 1629.

(9) Jin, H. J.; Park, J.; Karageorgiou, V.; Kim, U. J.; Valluzzi, R.; Cebe, P.; Kaplan, D. L. *Adv. Funct. Mater.* **2005**, *15*, 1241.

(10) Bettinger, C. J.; Bruggeman, J. P.; Misra, A.; Borenstein, J. T.; Langer, R. *Biomaterials* **2009**, *30*, 3050.

(11) Bigi, A.; Cojazzi, G.; Panzavolta, S.; Rubini, K.; Roveri, N. *Biomaterials* **2001**, *22*, 763.

(12) Zhao, Y.; Jiang, Q.; Xu, H.; Reddy, N.; Xu, L.; Yang, Y. *J. Biomed. Mater. Res. - Part B Appl. Biomater.* **2014**, *102*, 729.

(13) Kundu, B.; Kurland, N. E.; Bano, S.; Patra, C.; Engel, F. B.; Yadavalli, V. K.; Kundu, S. C. *Prog. Polym. Sci.* **2014**, *39*, 251.

(14) Kim, D.-H.; Viventi, J.; Amsden, J. J.; Xiao, J.; Vigeland, L.; Kim, Y.-S.; Blanco, J. A.; Panilaitis, B.; Frechette, E. S.; Contreras, D.; Kaplan, D. L.; Omenetto, F. G.; Huang, Y.; Hwang, K.-C.; Zakin, M. R.; Litt, B.; Rogers, J. A. *Nat. Mater.* **2010**, *9*, 511.

(15) Pritchard, E. M.; Valentin, T.; Panilaitis, B.; Omenetto, F.; Kaplan, D. L. *Adv. Funct. Mater.* **2013**, *23*, 854.

(16) Anyango, J. O.; Taylor, J.; Taylor, J. R. N. *J. Agric. Food Chem.* **2011**, *59*, 12674.

(17) Knowles, T. P. J.; Oppenheim, T. W.; Buell, A. K.; Chirgadze, D. Y.; Welland, M. E. *Nat. Nanotechnol.* **2010**, *5*, 204.

(18) Murphy, A. R.; John, P. S.; Kaplan, D. L. *Biomaterials* **2008**, *29*, 2829.

(19) Wihodo, M.; Moraru, C. I. *J. Food Eng.* **2013**, *114*, 292.

(20) Matsuda, S.; Iwata, H.; Se, N.; Ikada, Y. *J. Biomed. Mater. Res.* **1999**, *45*, 20.

(21) Tsuchiya, H.; Hoshino, Y.; Tajima, K.; Takagi, N. *J. Prosthet. Dent.* **1994**, *71*, 618.

(22) Greenfield, N. J. *Nat. Protoc.* **2006**, *1*, 2876.

(23) Rhim, J. W.; Gennadios, A.; Handa, A.; Weller, C. L.; Hanna, M. A. *J. Agric. Food Chem.* **2000**, *48*, 4937.

(24) Tejaswi Naidu, K.; Prakash Prabhu, N. *J. Phys. Chem. B* **2011**, *115*, 14760.

(25) Liscio, A.; Palermo, V.; Samorì, P. *Acc. Chem. Res.* **2010**, *43*, 541.

(26) Sinensky, A. K.; Belcher, A. M. *Nat. Nanotechnol.* **2007**, *2*, 653.

(27) Lang, N.; Pereira, M. J.; Lee, Y.; Friehs, I.; Vasilyev, N. V; Feins, E. N.; Ablasser, K.; O'Cearbhaill, E. D.; Xu, C.; Fabozzo, A.; Padera, R.; Wasserman, S.; Freudenthal, F.; Ferreira, L. S.; Langer, R.; Karp, J. M.; del Nido, P. J. *Sci. Transl. Med.* **2014**, *6*, 218ra6.

(28) Jiang, S.; Cao, Z. *Adv. Mater.* **2010**, *22*, 920.

(29) Shah, N. J.; Hyder, M. N.; Moskowitz, J. S.; Quadir, M. A.; Morton, S. W.; Seeherman, H. J.; Padera, R. F.; Spector, M.; Hammond, P. T. *Sci. Transl. Med.* **2013**, *5*, 191ra83.

(30) Subramani, C.; Saha, K.; Creran, B.; Bajaj, A.; Moyano, D. F.; Wang, H.; Rotello, V. M. *Small* **2012**, *8*, 1209.

CHAPTER 3

MIXED PROTEIN FILMS AS TUNABLE BIOMATERIAL PLATFORM

3.1. Introduction

Protein derived materials offer an inherently sustainable and structurally diverse platform for the fabrication of functional materials.[1,2,3] Protein films provide particularly attractive scaffolds for biomaterials, combining biodegradability and biocompatibility in versatile materials comprised of natural precursors.[4,5,6] Furthermore, the protein surface creates a molecular template for controlling interactions with biological systems.[7,8,9] These favorable attributes have made these protein-based materials highly amenable to interface with cells for tissue engineering[10,11] and wound healing[12,13] applications.

Recently, we have developed an additive free, nanoimprint lithography (NIL) based method for the generation of water stable protein films.[14] Based on previous studies of patterned and multicomponent thin films,[15,16,17] we hypothesized that inkjet printing of proteins would provide a suitable method for the "direct-writing" of two-dimensional biomolecular patterns to complement our NIL protein film fabrication strategy. Herein, we describe a combined inkjet printing based deposition with nanoimprint lithography stabilization methodology generates materials surfaces with tunable biological interactions. The utility of these films was demonstrated through the controlled adhesion and migration of mammalian fibroblasts as well as bacteria. This versatile nanomanufacturing platform is a promising system for the rapid prototyping of new biomaterials with tunable surface properties.

3.2. Results and Discussion

Inkjet printing provides a reproducible method for controlling the mixing and deposition of nanomaterials.[18] Previous studies have demonstrated that proteins can readily be inkjet printed without vastly altering the intrinsic properties of the protein.[19] We hypothesized that the parametric control offered by inkjet printing would allow us to dial in the biological response to combinatorial protein films. As shown in Figure 3.1, inkjet deposition of protein-based inks generates micron-patterns whose components can be modularly assembled. Following this directed deposition, the proteins are stabilized into a functional film using an additive free, nanoimprint lithography based method that is stable to cell culture conditions as described in Chapter 2. This NIL methodology is crucial for film stabilization as the process is not dependent on the protein precursor used and does not add biologically adverse substances to the film.

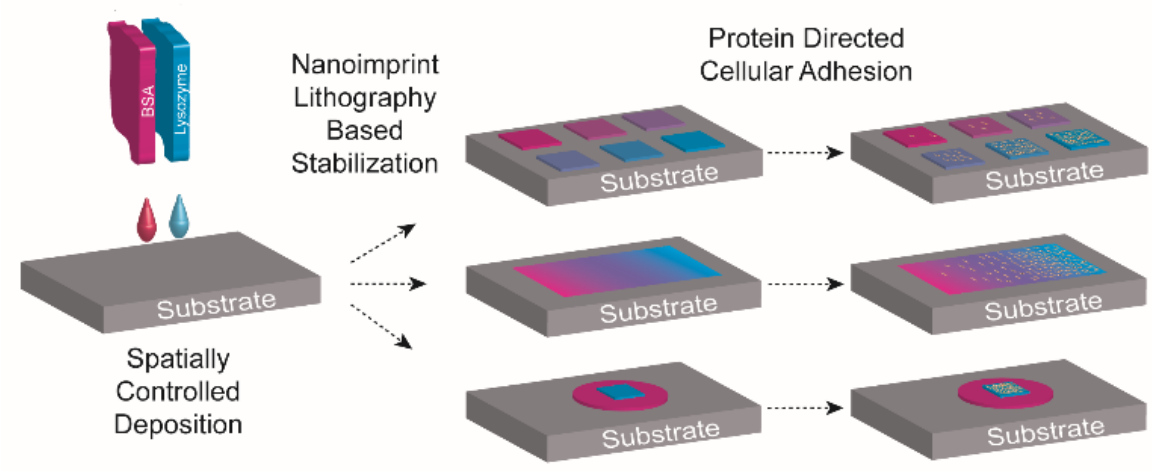

Figure 3.1: Schematic of film processing strategy to generate protein films. Inkjet directed deposition controls both the film composition and spatial presentation of the protein components.

We chose to probe cellular adhesion as a model biological response as the regulation of cellular adhesion/migration has been shown to be a critical factor in a variety of biological processes including cell differentiation.[20] tissue development.[21] and cancer progression.[22] Bovine serum albumin (BSA, MW 66.3 kDa, pI 4.8) and lysozyme (Lyso, MW 14.3 kDa, pI 11) were selected as our model anionic and cationic protein inks, respectively. Films were generated through the deposition of the protein inks in a parametric fashion. Film composition was varied from 100 % BSA to 100 % Lyso in 20 % increments. Each ratio displayed a similar roughness and thickness indicating that the surface interactions of the film with its environment should be entirely electrostatic in nature. (Table 3.1)

Table 3.1: Thickness and roughness of protein films with different ratio of BSA and Lyso. The thickness was measured using ellipsometry (n=5) and the roughness was obtained by AFM.

Composition	**Thickness (nm)**	**Roughness (nm)**
100 % BSA	134.9 ± 0.3	0.55
20 % Lyso	134.2 ± 0.1	1.039
40 % Lyso	136.3 ± 2.6	1.095
60 % Lyso	136.8 ± 3.3	3.144
80 % Lyso	133.6 ± 0.4	4.829
100 % Lyso	134.8 ±1.1	0.72

The deposition of functionalized nanoparticles was quantified using laser ablation inductively coupled plasma mass spectrometric imaging (LA-ICP-MSI) to probe the successful incorporation of protein charge into the properties of the film.[23,24] Surface functionalized gold nanoparticles (AuNPs) are an ideal probe for understanding supramolecular interactions at a biologically relevant scale.[25] We incubated the films

generated from varying ratios of proteins with AuNPs possessing either cationic or anionic headgroups. Using LA-ICP-MSI, we characterized the adhesion of the AuNPs with respect to their complementary interactions with each film constituent. As shown in Figure 3.2a, b, the cationic AuNPs selectively adhere to BSA containing films whereas the anionic AuNPs were adsorbed to the Lyso films. These results indicated that the intrinsic protein charges were successfully incorporated into the film and the overall property of protein film was tunable with respect to complementary electrostatic interactions.

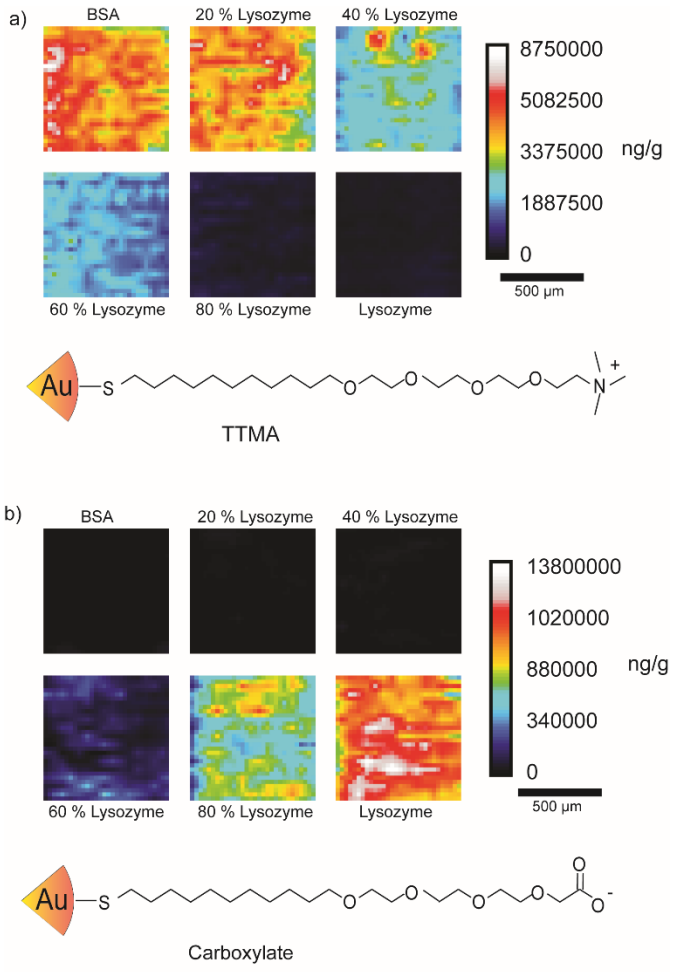

Figure 3.2: Adhesion of a) cationic and b) anionic AuNPs as determined by LA-ICP-MSI. Protein films were generated by varying the BSA:Lyso ratio of the film in 20 % increments. Scale bars are 500 µm.

Next, we determined whether this physiochemical response to nanomaterial interfaces was translatable to biological systems. We quantified the adhesion of mammalian fibroblast cells using films generated from increasing ratios of BSA:Lyso. As shown in Figure 3.3, cells adhere to films generated with greater percentages of Lyso with a drastic increase observed with films comprised of 80 % or more of Lyso. Films

fabricated with higher BSA amounts demonstrated minimal adhesion confirming the incorporation of protein charge into the overall materials properties of the film.

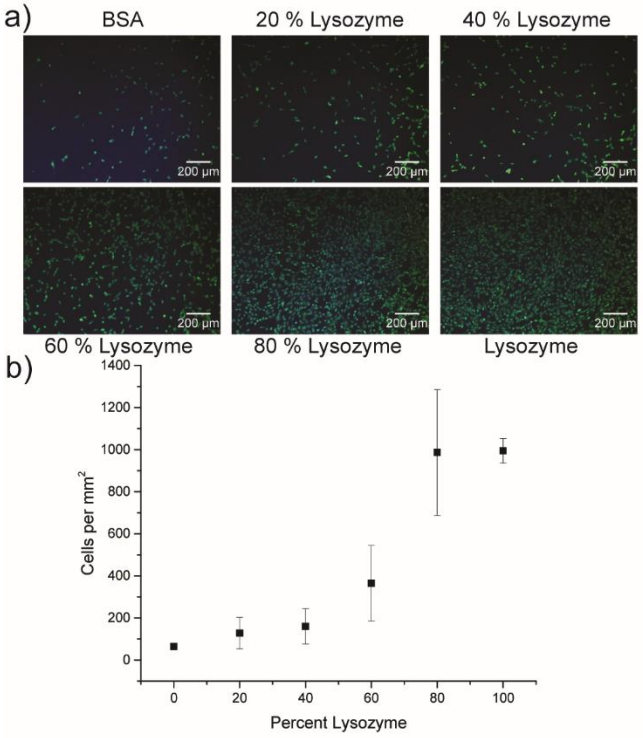

Figure 3.3: Adhesion of mammalian fibroblasts on films with varying ratios of protein components. a) Cells were stained with Hoescht 33342 and Calcein AM to label the cell nuclei and cytosol, respectively. Scale bars are 200 µm. b) Average number of cells per mm^2 as determined using image analysis. (see Figure 3.12)

We generated a gradient where the BSA:Lyso ratio was varied to further probe the adhesion based on the composition of mixed protein component. As shown in Figure 3.4a, c, the cells preferentially adhere to the Lyso containing portion of the film. Notably, the films ratiometric and gradient patterns demonstrate highly correlative results underpinning the robustness with which biomaterial properties can be dialled in through modular assembly.

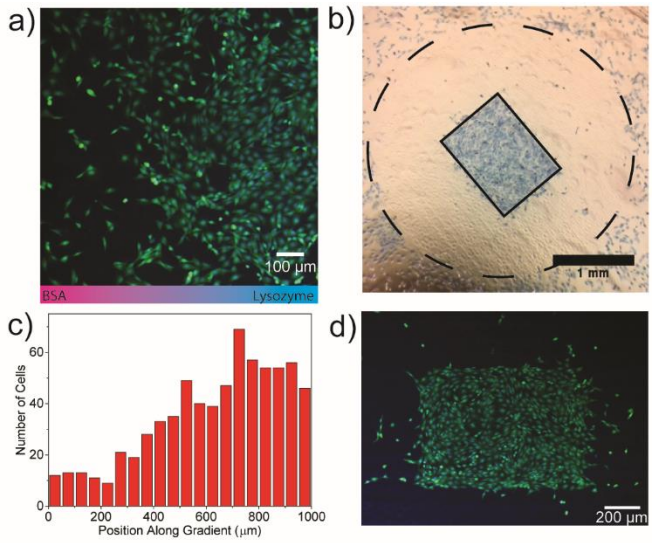

Figure 3.4: Adhesion of mammalian fibroblasts on micropatterned films. a) Cell adhesion to protein film generated with a gradient pattern. Cells were stained with Hoescht 33342 and Calcein AM to label the cell nuclei and cytosol, respectively. b) Cell adhesion to patterned film with discrete Lyso and BSA domains. The solid line (Lyso) and dotted line (BSA) were drawn to aid the eye. c) Number of cells with respect to position along gradient as determined using image analysis. (see Figure 3.13) d) Fluorescence micrograph of cells adhered to Lyso pattern surrounded by BSA. Scale bars are 100 µm for a), 200 µm for d), and 1 mm for b).

Inkjet printing advantageously affords spatial control over the deposition of film components. We deposited a rectangle of Lyso surrounded by a circle of BSA to probe the dependence of cellular adhesion as a function of geometric deposition. As shown in Figure 3.4b, d, the cells preferentially adhere to the Lyso pattern and can be easily washed away from the BSA coated surface. This dynamic process of cellular attachment was also observed at the boundary of BSA and Lyso patterns as shown in Video 3.1.

We next tested the generality of the observed selective adhesion using a model bacteria strain, *Escherichia coli* DH5α (*E. coli)*. The bacteria strain was induced to express the red fluorescent protein td-Tomato in order to readily image the adhered bacteria. As shown in Figure 3.5, the bacteria preferentially adhered to the lysozyme rich

films. This observation is in agreement with previous studies that demonstrate the negatively charged bacterial cell walls adhere to anionic surfaces.[26]

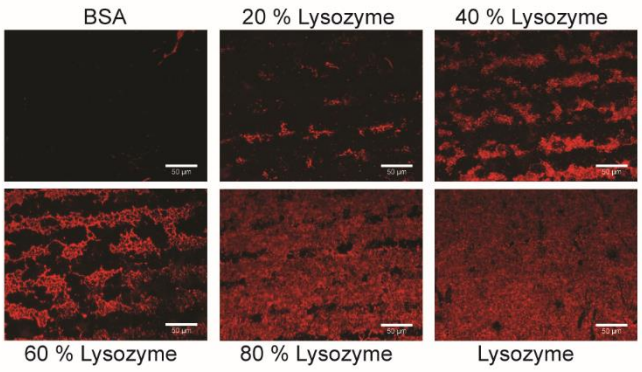

Figure 3.5: Fluorescence micrographs showing the adhesion of *E. coli* DH5α expressing red fluorescent protein after 1 day of incubation. Scale bars are 50 μm.

3.3. Conclusions

In conclusion, we have developed a highly modular method to generate stable protein films in a rapid fashion with diverse components. The environmentally friendly processing taken with the parametric control over the surface chemistry provides a multidimensional platform for understanding and controlling biological interactions with protein coated surfaces. Due to the minimal waste inherent to inkjet deposition incorporating engineered proteins into robust, bioactive films. Additionally, this strategy is readily translatable into a roll-2-roll methodology to generate biomaterials in a high-throughput fashion for potential wound healing and tissue engineering applications.

3.4. Experimental Methods

3.4.1. Materials

Bovine serum albumin (BSA) and lysozyme (Lyso) were purchased from Fisher Scientific and used without further purification. Silica wafers were purchased from WRS

Materials. Glass microscopy slides were purchased from Fisher Scientific. MilliQ water was purified by using a Millipore water purification system.

3.4.2. Synthesis of TTMA and Carboxylate AuNPs

Gold nanoparticles were synthesized according to previously reported methods.[27,28] Briefly, the Brust-Schiffrin two-phase synthesis method was used to synthesize pentanethiol-coated AuNPs with core diameter ca. 2 nm.[29,30] Murray place-exchange method[31] was followed to obtain the ligand-protected AuNPs. Pentanethiol-conjugated AuNPs (20 mg) and thiol ligand (60 mg) were dissolved in a mixture of dry DCM (6 ml) and methanol (2 ml) and stirred under N_2 atmosphere for 3 days at room temperature. The solvents were removed under reduced pressure and the resulting precipitate was washed with hexane (20 ml) three times and DCM:hexane mixture (1:1 v/v, 20 ml) four times. Then the precipitate was dissolved in distilled water (~ 8 ml) and dialyzed for three days (membrane molecular weight cut-off =10,000, volume of the dialysis bucket is 5 L) to remove excess ligands, pentanethiol, acetic acid, and other salts present in the nanoparticle solution. After dialysis, the particle was lyophilized to yield a solid brownish product. The particles were then re-dispersed in deionized water.

3.4.3. Mass Spectrometric Characterization of Ligand Composition

Matrix assisted laser desorption/ionization mass spectroscopy (MALDI-MS) has been performed to characterize the surface ligand on the AuNPs (Figure 3.6 and 3.7).[32] A saturated α-Cyano-4-hydroxycinnamic acid (α-CHCA) stock solution was prepared in 70% acetonitrile, 30% H_2O, and 0.1% trifluoroacetic acid. An equal volume of 2 μM NP solution was added to the matrix stock solution. 2.5 μL of this mixture was applied to the

sample carrier, and then the MALDI-MS analysis was performed on a Bruker Autoflex III mass spectrometer.

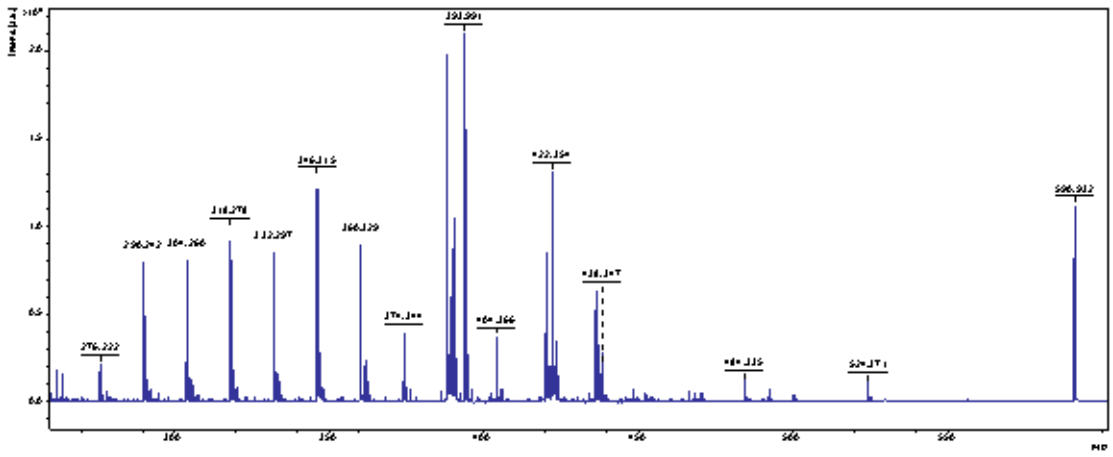

Figure 3.6: Matrix-assisted laser desorption/ionization mass spectroscopy (MALDI-MS) spectrum of TTMA NPs. $[MH]^+$ = 422.33.

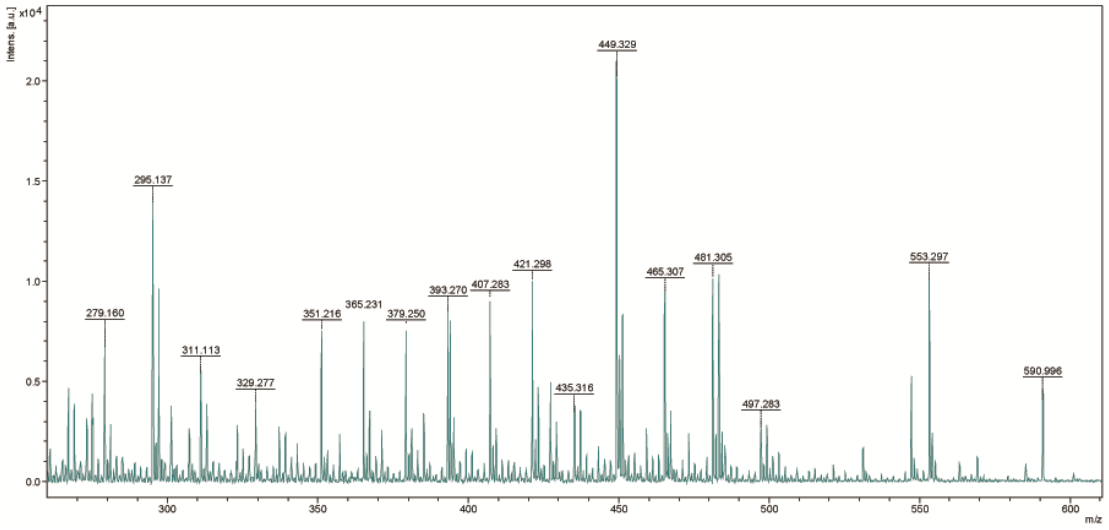

Figure 3.7: Matrix-assisted laser desorption/ionization mass spectroscopy (MALDI-MS) spectrum of carboxylate NPs. $[MH+2Na-H-H_2S]^+$ = 449.25.

3.4.4. Dynamic Light Scattering (DLS)

DLS experiments and zeta potential measurements were performed using a Malvern Zetasizer Nano ZS. Samples were sonicated prior to measurements.

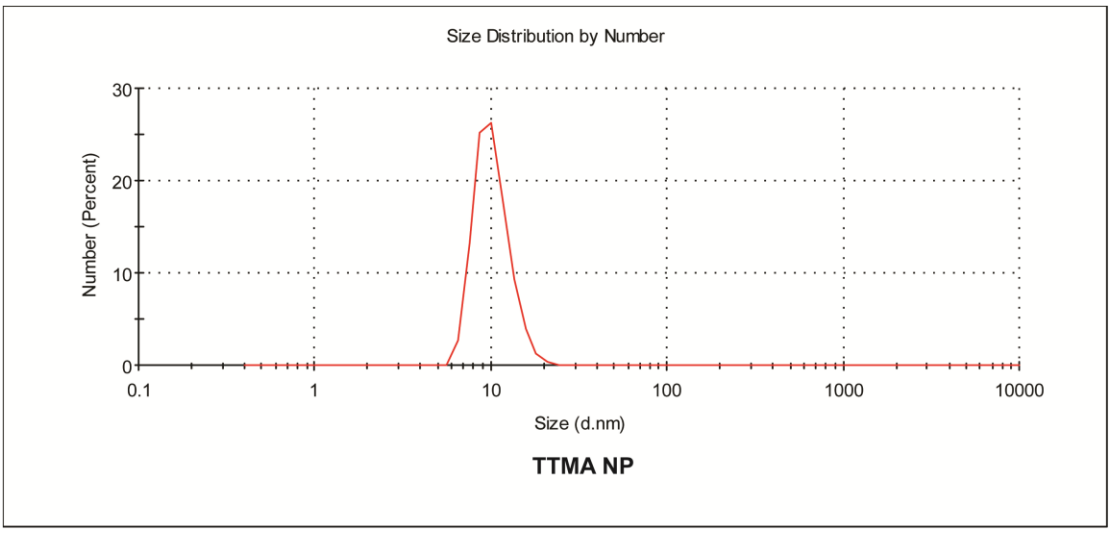

Figure 3.8: DLS measurements of TTMA NPs was obtained in 5 mM phosphate buffer at pH 7.4. The average size was 10.3 ± 2.42 nm.

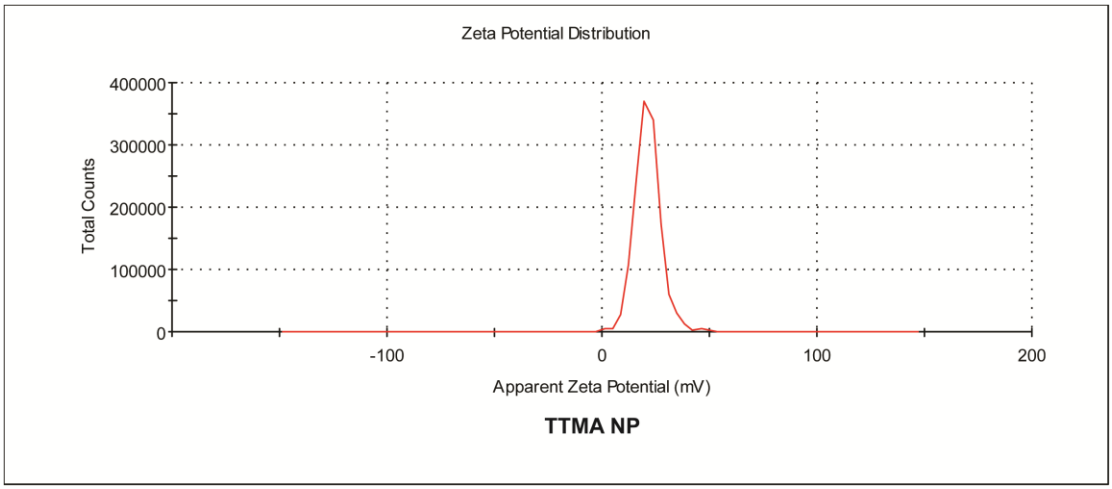

Figure 3.9: Zeta potential of TTMA NP was measured by DLS in 5 mM phosphate buffer at pH 7.4. The overall charge of this cationic TTMA NPs is measured as 21.1 ± 5.93 mV.

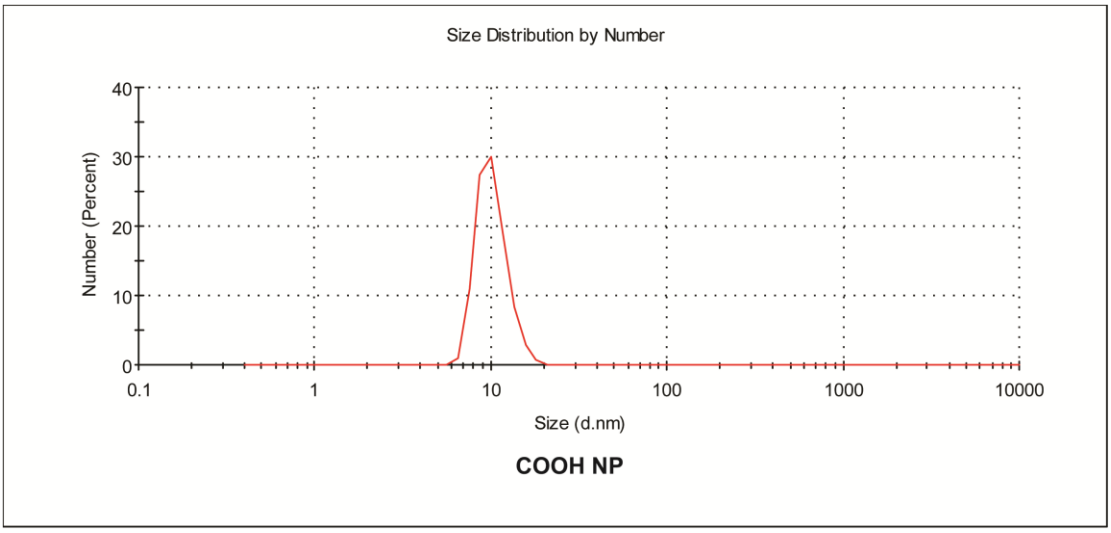

Figure 3.10: DLS measurements of COOH NPs was obtained in 5 mM phosphate buffer at pH 7.4. The average size was 10.2 ± 2.06 nm.

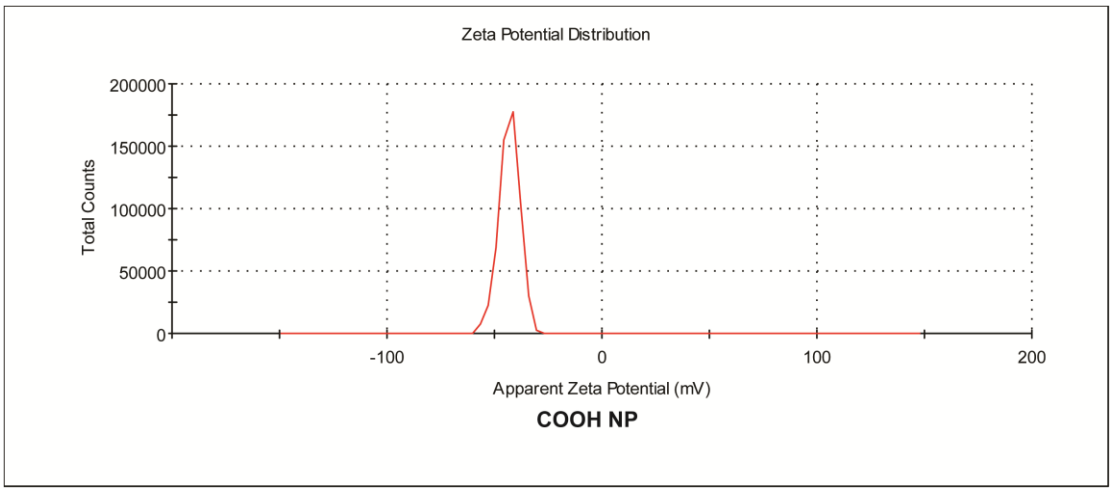

Figure 3.11: Zeta potential of COOH NP was measured by DLS in 5 mM phosphate buffer at pH 7.4. The overall charge of this anionic AuNPs is measured as -43.1 ± 4.71 mV.

3.4.5. Inkjet Deposition of Protein Inks

The inkjet printing was done using an Epson Artisan 50 inkjet printer. The BSA and Lyso were diluted to a concentration of 5 wt% with 80:20 volume ratio of water/ethanol solution, filtered through a 0.2 µm polypropylene membrane (Puradisc 25AS, Whatman),

and syringed into a virgin aftermarket Epson inkjet cartridge for printing (MIS Associates, Auburn Hills, MI USA). For this work, the BSA solution was loaded in magenta channel and the lysozyme solution was loaded in cyan channel. Printing was done using an Epson Artisan 50 inkjet printer (Long Beach, CA USA) which was used as packaged. The glass substrate was loaded into the printer by taping the bottom of the substrate to the included CD tray. Patterning was done by using the Print CD software provided with the Epson printer. In order to print only the channel of interest, the color of the pattern has to match the channel printed. To print only the magenta channel, the RGB value must be set to (255,0,255); the cyan channel, (0,255,255). The ICM color management also must be turned off in the Advanced tab of the printer properties to ensure no mixing of the channels occurs. To print BSA/Lyso mixed patterns, the ratio of magenta/cyan were converted into corresponding RGB value on the website: http://web.forret.com/tools/color.asp. The gradient pattern from 100% BSA to 100% Lyso was made by color gradient tool in the Print CD software. Before printing, the printheads were cleaned two times using the "Head Cleaning" function in the Maintenance tab of the printer properties to ensure that the channels were filled.

3.4.6. Nanoimprint Lithography

Nanoimprinting of protein films was performed by using a Nanonex NX-2000 nanoimprinter with flat silicon molds. Imprinting was performed at 180 °C and 2.8 MPa for 5 min. All molds were treated with heptadecafluoro-1,1,2,2-(tetrahydrodecyl)dimethyl-chlorosilane at 75 °C for 2 days in a vacuum chamber prior to use.

3.4.7. Cell Culture

NIH 3T3 cells were cultured in a humidified atmosphere (5 % CO_2) at 37 °C, and grown in Dulbecco's modified Eagle's medium (DMEM, low glucose) supplemented with 10 % fetal bovine serum (FBS) and 1 % antibiotics (100 U/mL penicillin and 100 μg/mL streptomycin).

Cell adhesion experiments were performed by incubating 150,000 NIH 3T3 cells with protein coated silica wafers placed in a 12-well plate for 1 h. The surfaces were then washed by cold phosphate buffer saline (PBS) 3 times to remove floating cells, followed by incubation with 1 mL of fresh media for 23 h. Cells were then stained with Calcein AM and Hoescht 33342 to label cytosol and nucleus, respectively, for fluorescent microscopic imaging according to the protocol from Life Technology using an Olympus IX51 microscope with excitation wavelengths of 470 nm and 535 nm.

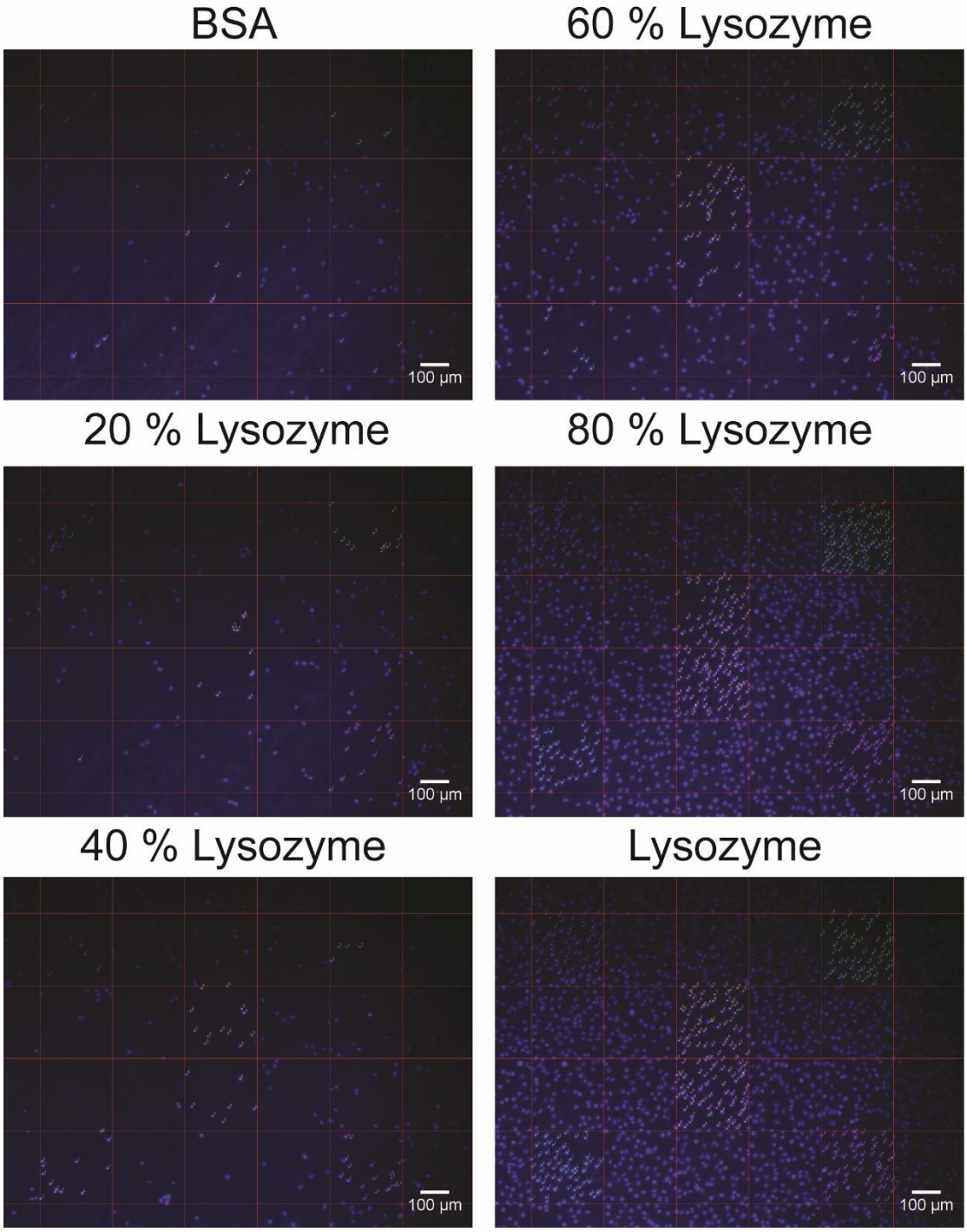

Figure 3.12: Cell counting data on mixed protein films of varying protein ratios were obtained using ImageJ software. Box dimensions are 250 µm x 250 µm.

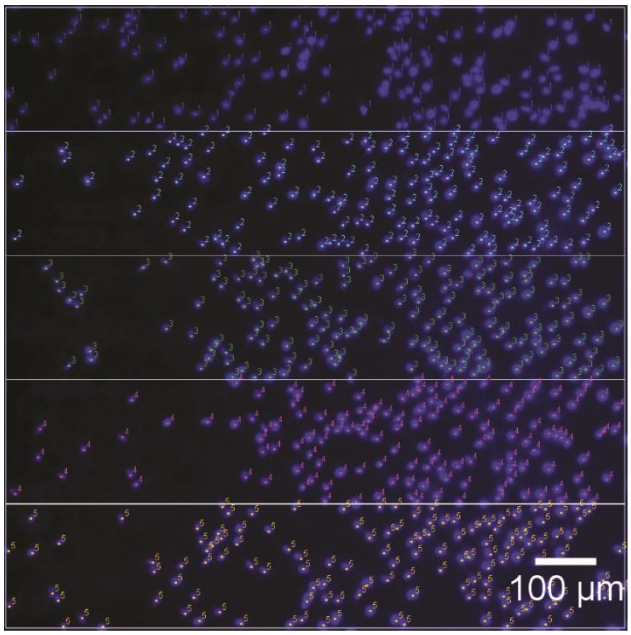

Figure 3.13: Cell counting data on gradients were obtained using ImageJ software. Box dimensions are 1000 µm x 200 µm.

Live cell video imaging was performed by incubating 300,000 NIH 3T3 cells with protein patterned glass slides in a 35 mm petri dish for 1 h. Slides were then washed with PBS 3 times to remove floating cells, the petri dish was filled with 4 mL of fresh media and placed into a CO_2 chamber with temperature control on the microscope. Optical images of cells were then continuously recorded using an Olympus IX51 microscope every 15 min for 8 h.

3.4.8. Bacteria Adhesion Studies

Bacteria were inoculated in 3 mL LB broth and grown to stationary phase at 37 °C. The cultures were then diluted in M9 broth supplemented with 1 mM IPTG (isopropyl β-D-1-thiogalactopyranoside). 2 mL of the dilution was transferred into the wells of a 24 well plate containing Silicon coated surfaces (22 × 22 mm). The 24 well plate was kept at 25

°C and the biofilms were allowed to grow for 24 hours. In general, the surfaces with biofilms were rinsed in deionized water for three times before imaging.

3.4.9. Inductively Coupled Plasma Mass Spectrometry Imaging

For the characterization of the nanoimprinted protein samples, we used laser ablation-inductively coupled plasma mass spectrometry (LA-ICP-MS) imaging. Imaging was done using a CETAC LSX-213 G2 laser ablation system (Photon Machines, Omaha, NE, USA) attached via a 2 m length of tubing to a Perkin Elmer NEXION 300X ICP mass spectrometer. Prior to analysis of the samples, we dropped a 1 µL of TTMA and COOH functionalized AuNPs separately. Then, using imaging, we generated Au map distribution of these AuNPs on the nanoimprinted surfaces. The parameters used for the imaging experiment can be found on Table 3.2.

Table 3.2: Experimental conditions used for LA-ICP-MS analysis.

Laser ablation parameters		ICP-MS parameters	
Spot size	50 µm	Rf power	1.6 kW
Scan rate	10 µm/s	Nebulizer flow rate	0.7 L/min
Laser energy	3.34 J	Plasma flow rate	16.5 L/min
Frequency	10 hz	Auxiliary flow rate	1.4 L/min
Carrier gas flow rate (Helium)	0.6 L/min	Pulse and Analog stage voltages	950 V(Pulse), -1600 V(Analog)
		Deflector voltage	-12 V
		Dwell time	50 ms

Using the parameters show on the Table 3.2, imaging experiments were performed to obtain Au maps of the samples. The results obtained from ICP-MS analysis were further processed using Excel and then images of the samples were generated using ImageJ software. To obtain quantitative images of the samples, chicken breast tissues were purchased from a local market and they were homogenized using PowerGen 125 homogenizer. Homogenized tissues were centrifuged at 12000 rpm for 5 minutes and the

powders precipitated were collected. 5 aliquots of 50 mg of homogenate were weight and placed into 0.5 mL tubes. Different concentration of AuNPs (0, 0.125, 0.25, 0.5 and 1μM) were injected into these 50 mg aliquots and frozen to be sliced. The frozen block of sample then sliced to 12 μm thickness using a LEICA CM1850 cryostat. The sliced tissues were imaged under the same conditions following the analysis of the nanoimprinted samples.

3.5. References

(1) Silva, N. H. C. S.; Vilela, C.; Marrucho, I. M.; Freire, C. S. R.; Pascoal Neto, C.; Silvestre, A. J. D. *J. Mater. Chem. B* **2014**, *2*, 3715.

(2) Kharlampieva, E.; Kozlovskaya, V.; Wallet, B.; Shevchenko, V. V; Naik, R. R.; Vaia, R.; Kaplan, D. L.; Tsukruk, V. V. *ACS Nano* **2010**, *4*, 7053.

(3) Omenetto, F. G.; Kaplan, D. L. *Science* **2010**, *329*, 528.

(4) Hu, X.; Cebe, P.; Weiss, A. S.; Omenetto, F.; Kaplan, D. L. *Mater. Today* **2012**, *15*, 208.

(5) Kim, D.-H.; Viventi, J.; Amsden, J. J.; Xiao, J.; Vigeland, L.; Kim, Y.-S.; Blanco, J. A.; Panilaitis, B.; Frechette, E. S.; Contreras, D.; Kaplan, D. L.; Omenetto, F. G.; Huang, Y.; Hwang, K.-C.; Zakin, M. R.; Litt, B.; Rogers, J. A. *Nat. Mater.* **2010**, *9*, 511.

(6) Gagner, J. E.; Kim, W.; Chaikof, E. L. *Acta0 0Biomater.* **2014**, *10*, 1542.

(7) Knowles, T. P. J.; Oppenheim, T. W.; Buell, A. K.; Chirgadze, D. Y.; Welland, M. E. 1*Nat. Nanotechnol.* **2010**, *5*, 204.

(8) Murphy, A. R.; John, P. S.; Kaplan, D. L. *Biomaterials* **2008**, *29*, 2829.

(9) Zheng, W.; Zhang, W.; Jiang, X. *Adv. Healthc. Mater.* **2013**, *2*, 95.

(10) Gomes, S.; Leonor, I. B.; Mano, J. F.; Reis, R. L.; Kaplan, D. L. *Prog. Polym. Sci.* **2012**, *37*, 1.

(11) Werkmeister, J. A.; Ramshaw, J. A. M. *Biomed. Mater.* **2012**, *7*, 012002.

(12) Gil, E. S.; Panilaitis, B.; Bellas, E.; Kaplan, D. L. *Adv. Healthc. Mater.* **2013**, *2*, 206.

(13) Har-el, Y.; Gerstenhaber, J. a.; Brodsky, R.; Huneke, R. B.; Lelkes, P. I. *Wound Med.* **2014**, *5*, 9.

(14) Jeoung, E.; Duncan, B.; Wang, L.-S.; Saha, K.; Subramani, C.; Wang, P.; Yeh, Y.; Kushida, T.; Engel, Y.; Barnes, M. D.; Rotello, V. M. *Adv. Mater.* **2015**, *27*, 6251.

(15) Tao, H.; Marelli, B.; Yang, M.; An, B.; Onses, M. S.; Rogers, J. a.; Kaplan, D. L.; Omenetto, F. G. *Adv. Mater.* **2015**, *27*, 4273.

(16) Yoon, S.-H.; Kim, Y. K.; Han, E. D.; Seo, Y.-H.; Kim, B. H.; Mofrad, M. R. K. *Lab Chip* **2012**, *12*, 2391.

(17) Chen, X.; Su, Y. D.; Ajeti, V.; Chen, S. J.; Campagnola, P. J. *Cell. Mol. Bioeng.* **2012**, *5*, 307.

(18) Creran, B.; Li, X.; Duncan, B.; Kim, C. S.; Moyano, D. F.; Rotello, V. M. *ACS Appl. Mater. Interfaces* **2014**, *6*, 19525.

(19) Delaney, J. T.; Smith, P. J.; Schubert, U. S. *Soft Matter* **2009**, *5*, 4866.

(20) Park, J. S.; Chu, J. S.; Tsou, A. D.; Diop, R.; Tang, Z.; Wang, A.; Li, S. *Biomaterials* **2011**, *32*, 3921.

(21) Pati, F.; Jang, J.; Ha, D.-H.; Won Kim, S.; Rhie, J.-W.; Shim, J.-H.; Kim, D.-H.; Cho, D.-W. *Nat. Commun.* **2014**, *5*, 3935.

(22) Liou, Y. R.; Torng, W.; Kao, Y. C.; Sung, K. Bin; Lee, C. H.; Kuo, P. L. *PLoS One* **2014**, *9*.

(23) Groseclose, M. R.; Castellino, S. *Anal. Chem.* **2013**, *85*, 10099.

(24) Becker, J. S. *Int. J. Mass Spectrom.* **2010**, *289*, 65.

(25) Tonga, G. Y.; Saha, K.; Rotello, V. M. *Adv. Mater.* **2014**, *26*, 359.

(26) Miller, K. P.; Wang, L.; Benicewicz, B. C.; Decho, A. W. *Chem. Soc. Rev.* **2015**, *44*, 7787.

(27) Mout, R.; Tonga, G. Y.; Ray, M.; Moyano, D. F.; Xing, Y.; Rotello, V. M. *Nanoscale* **2014**, *6*, 8873.

(28) Kim, C. S.; Le, N. D. B.; Xing, Y.; Yan, B.; Tonga, G. Y.; Kim, C.; Vachet, R. W.; Rotello, V. M. *Adv. Healthc. Mater.* **2014**, *3*, 1200.

(29) Kanaras, A. G.; Kamounah, F. S.; Schaumburg, K.; Kiely, C. J.; Brust, M. *Chem. Commun. (Camb).* **2002**, 2294.

(30) Brust, M.; Walker, M.; Bethell, D.; Schiffrin, D. J.; Whyman, R. *J. Chem. Soc. Chem. Commun.* **1994**, 801.

(31) Templeton, A. C.; Wuelfing, W. P.; Murray, R. W. *Acc. Chem. Res.* **2000**, *33*, 27.

(32) Yan, B.; Zhu, Z.-J.; Miranda, O. R.; Chompoosor, A.; Rotello, V. M.; Vachet, R. W. *Anal. Bioanal. Chem.* **2010**, *396*, 1025.

CHAPTER 4

NANOZYME-BASED OLFACTORY SYSTEM ENHANCER (NOSE)

4.1. Introduction

Odorous compounds function as potent sensory agents eliciting almost immediate and primal human responses. The human olfactory system has evolved to be capable of detecting extremely low concentrations of volatile organic compounds present in complex environments.[1] Furthermore, humans can discriminate more than 1 trillion olfactory stimuli, several orders of magnitude greater than their capability of visual discrimination.[2] For example, the aromatic compounds generated during the Maillard reaction offer rare insights into the countless chemical transformations that occur during this redolent process.[3,4] However, a variety of biological and non-volatile chemical interactions are transient and remain undetectable to humans without these small molecule products.[5] Consequently, translating reversible molecular events into a signal that is interpretable by the human olfactory system continues to be an elusive goal.

Nanotechnology provides a unique avenue to redefine the bounds of human perception.[6] In particular, engineering the surface of nanomaterials is a powerful strategy to direct interactions at the molecular level. [7] Previously, surface functionalized gold nanoparticles have been used to generate array-based sensors,[8] regulate enzymatic activity, [9] and influence cellular growth on surfaces.[10] The proximate response to the nanomaterials has been shown to be controlled in a surface moiety dependent fashion.[11] Engineered nanomaterials

have also been shown to influence the behavior of fragrance molecules.[12] In a recent study, Weder *et al*. demonstrated cellulose nanocrystals functionalized with pro-fragrance molecules could be used to control the production of volatile compounds.[13] These covalently bound complexes remain odorless until certain functional groups are cleaved in response to specific external stimuli to generate the pungent aroma molecules.[14] Taken together, we hypothesized that pro-fragrances in combination with surface engineered nanomaterials could behave as reactive constructs to translate molecular interactions into scent.

Herein, we describe a supramolecular-based approach to augment human olfactory perception. The Nanozyme-based Olfactory System Enhancer (NOSE) readily complements the high sensitivity innate with the human olfactory system. The system is comprised of 3 tunable components: 1) pro-fragrance molecules, 2) surface functionalized nanoparticles, and 3) enzymes to cleave the pro-fragrances. The surface moieties of the nanoparticles behave as both selective recognition elements for analytes present in solution and to reversibly inhibit the complexed enzymes. This recognition tactic shifts the primary detection onus from the olfactory bulb to the binding equilibrium established by the nanoparticle with the protein which has been shown to be highly dependent tunable based the surface functionality of the nanoparticle.[15] We assessed the feasibility of our approach to expand human sensory capabilities by developing an olfactory-based bacteria sensor as a model supramolecular interaction. The NOSE allowed human subjects to detect bacteria in solution at levels as low as 10^2 cfu/mL indicating the system could effectively enrich human olfactory faculties.

4.2. Results and Discussion

We first sought to prototype our approach by creating a bacterial biosensor as bacteria-related illnesses from inadequate drinking water sources and improper sanitation practices contribute to over 1.5 million deaths worldwide a year.[16,17] Our sensor design is based on the selective activation of an inhibited enzyme in the presence of bacteria (Figure 4.1). Specifically, the sensor components are a cationic surface functionalized gold nanoparticle (AuNP), anionic *Candida Rugosa* lipase, and a pro-fragrance molecule, succinic acid monophenylethyl ester (SAME). We chose AuNPs possessing ligands with terminal benzyl headgroups as these nanoparticles have been shown to both interact with the anionic cell surface of bacteria as well as inhibit enzymatic activity.[18,19] We used *Candida Rugosa* lipase as a model, industrially relevant enzyme due to its robust characteristics and its ability to cleave ester bonds in a variety of conditions.[20] Pro-fragrances are volatile molecules that have been covalently modified to create a product that will generate the precursor fragrance upon cleavage of the covalent bond.[21] The succinic acid ester of phenylethyl alcohol was chosen as our representative pro-fragrance as it produces a pleasant rose scent upon cleavage and phenylethyl alcohol has a low odor threshold.[22] Figure 4.2 shows the NMR spectra of the synthesized pro-fragrance.

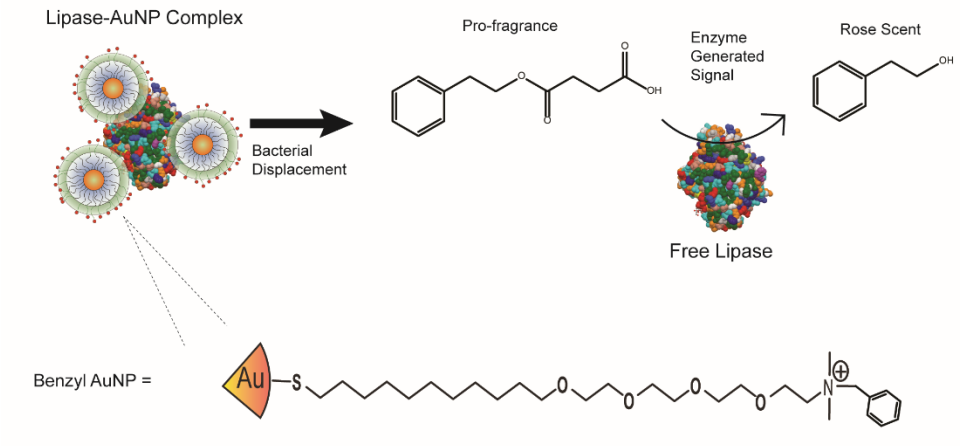

Figure 4.1: Schematic representation of sensor elements used in this study. Cationic AuNPs bind with the anionic enzyme inhibiting the catalysis of the pro-fragrance into scent. Bacteria present in solution compete for the AuNP surface and displace the enzyme inducing the production of the rose fragrance.

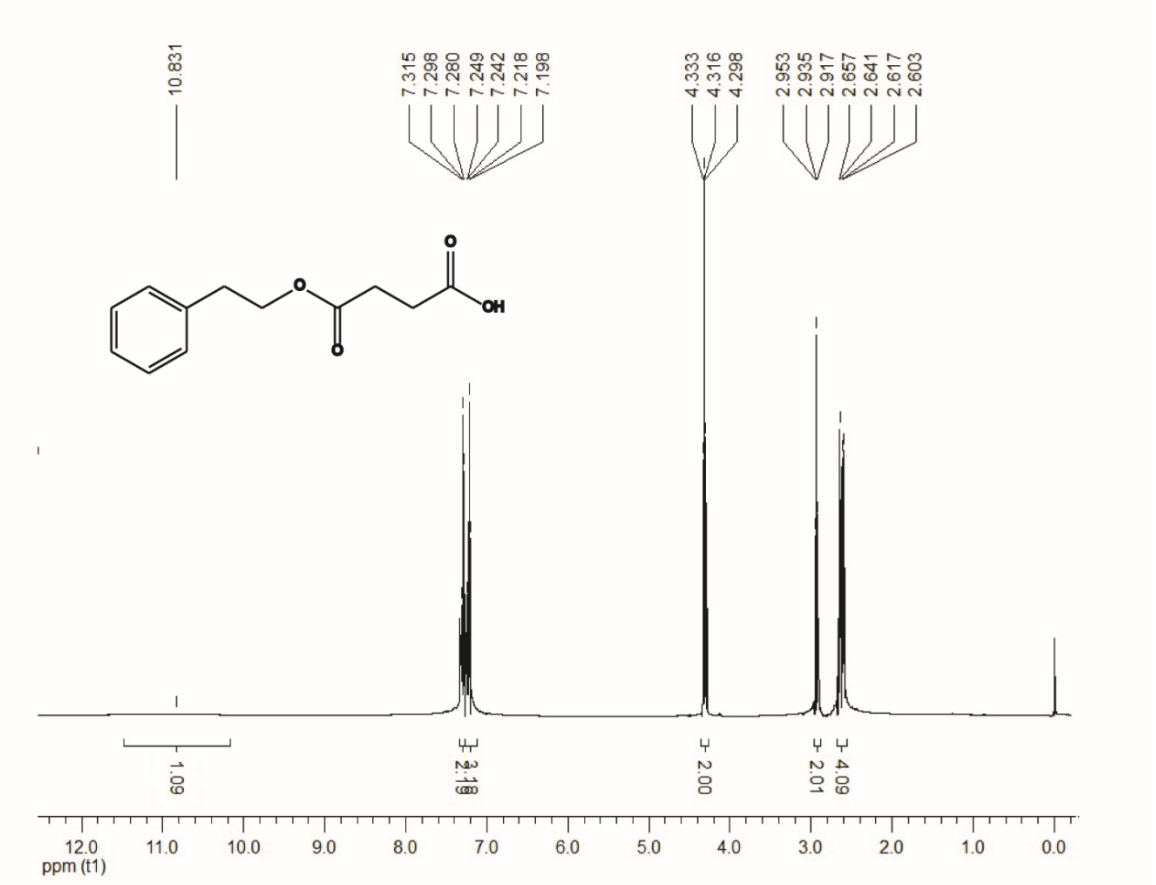

Figure 4.2: 400 MHz 1H NMR spectrum of the pro-fragrance, succinic acid monophenylethyl ester in chloroform-D (D-99.8 %). Spectrum was obtained on a Bruker Avance 400 MHz, 16 scans.

We initially performed a colorimetric assay to optimize the lipase to AuNP ratio needed for inhibition. These studies were performed using a 0.15 nM lipase concentration in sodium phosphate buffer solution (5 mM, pH 7.4) incubated with various concentrations of benzyl AuNP for 30 minutes to generate the sensor complexes. 10 µL of the colorimetric substrate p-nitrophenylbutyrate (pNPB, [0.6 mM], λmax = 405 nm) was added to the sensor complexes. As shown in Figure 4.3, a 3:1 AuNP to lipase

ratio completely inhibited the lipase. This AuNP:lipase ratio was used to generate the nanozyme complex for all further studies.

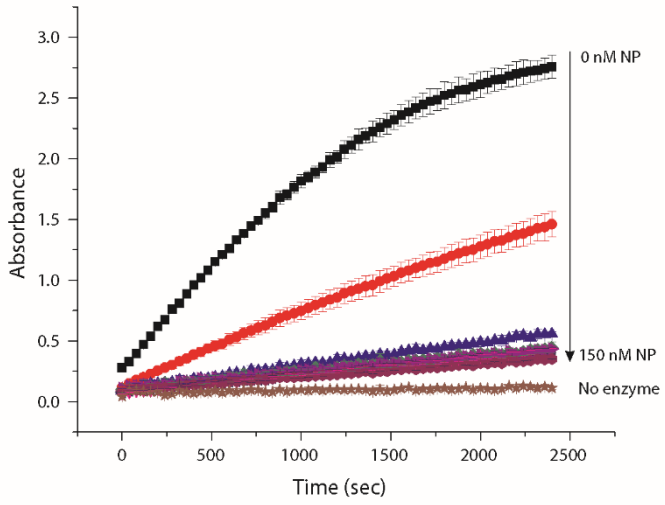

Figure 4.3: Lipase inhibition assay in the presence of benzyl AuNP. The same amount of lipase (15 nM) was incubated with a series of benzyl AuNP (from top to bottom: 0, 20, 40, 60, 80, 100, 125, 150 nM) before adding the colorimetric substrate p-NPB (0.6 mM). After the substrate was added, the activity of lipase was monitored up to 2400 seconds (40 minutes). A control of p-NPB without the enzyme did not produce a signal.

We used *Escherichia coli* XL1 (*E. coli*) as a model bacteria strain for our sensing studies with human participants. Ten volunteers were asked to smell four different glass vials at two time points (1 minute and 15 minutes to ensure olfactory clearance[23]) that contain four conditions: buffer, sensor only (AuNP and lipase), NOSE in a solution of *E. coli* at 10^2 cfu/mL and sensor in a solution of *E. coli* at 10^4 cfu/mL. Solutions of the sensor elements were incubated for 30 minutes prior to the addition of the pro-fragrance and bacteria. Samples were then incubated for 15 minutes in 20 mL glass vials. Each set of samples (four glass vials) was prepared individually for each participant. Volunteers then used rank ordering to indicate the intensity of rose scent within the samples. They ranked the samples in order from lightest smell to strongest smell with a scale from 1 to

5. As shown in Figure 4.4, participants were successfully able to detect the rose scent in the presence of uninhibited lipase. Notably, volunteers were able to detect *E. coli* concentrations at both 10^2 and 10^4 cfu/mL.

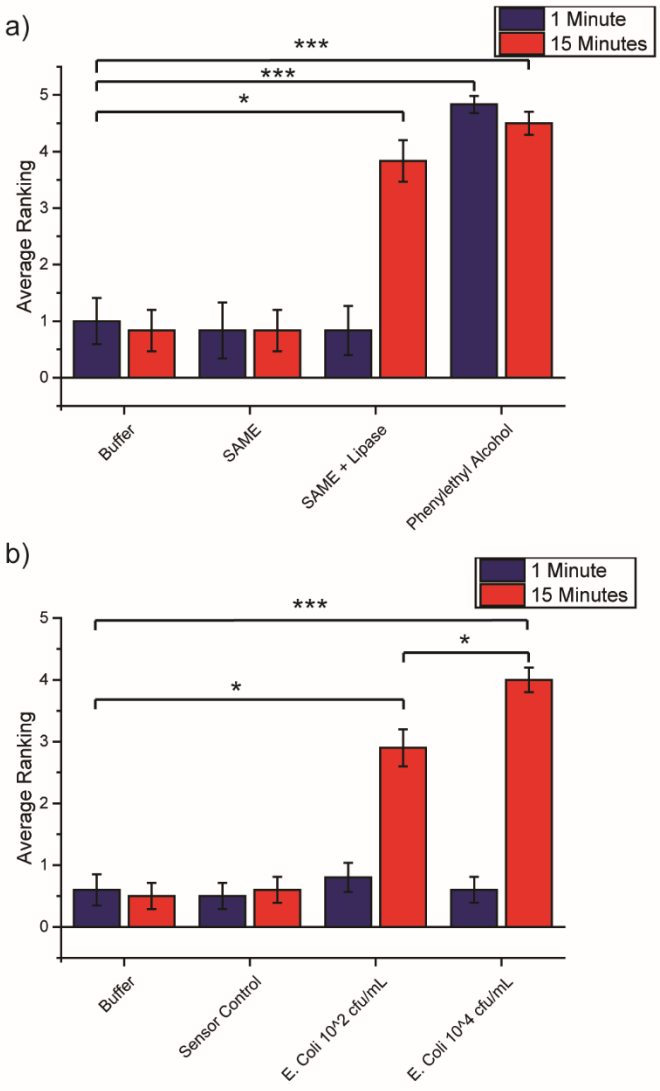

Figure 4.4: Olfactory detection study in human. a) Lipase activity test in the presence of SAME was carried out with six participants. SAME only and 5 mM sodium phosphate buffer were used as the negative control. The hydrolyzed form of SAME was used as the positive control (strong standard). b) With ten participants, olfactory detection of *E. coli* at 10^2 and 10^4 cfu/mL were compared to the controls of just buffer and NOSE only. The olfactory signals from the vials which contained 10^2 and 10^4 cfu/mL of *E. coli* are significantly different from the signal from the NOSE-only vial. Error bars represent the standard error of means for the measurements. *= $p< 0.05$, ***=$p<0.001$.

We next used headspace gas chromatography to quantify the production of scent by our bacterial sensor. The concentration of the volatile product present in the headspace of the sample vial was quantified according to an external calibration curve (see Supporting Information). As shown in Figure 4, the uninhibited lipase cleaves significantly more pro-fragrance than the NOSE and controls. The control samples of the highest bacteria concentration tested with the pro-fragrance molecule and the sensor without bacteria did not produce a signal. The NOSE in the presence of 10^4 and 10^6 cfu/mL of *E. coli* showed a measureable signal that was significantly different. However, 10^2 cfu/mL of *E. coli* did not produce a detectable signal under the conditions tested. We hypothesize this discrepancy with the human studies to be a result of the complexities of human olfactory system.

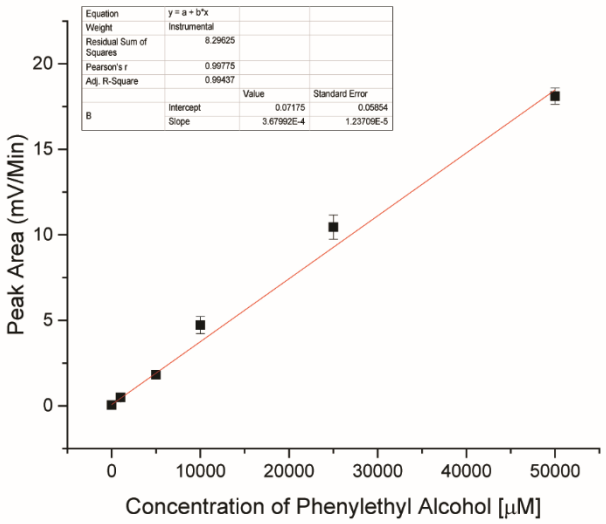

Figure 4.5: Calibration curve used to determine concentration of phenylethyl alcohol present in headspace of vials. Samples were prepared by diluting phenylethyl alcohol into 5 mM sodium phosphate buffer. Peak areas were determined using Origin 9.1 software.

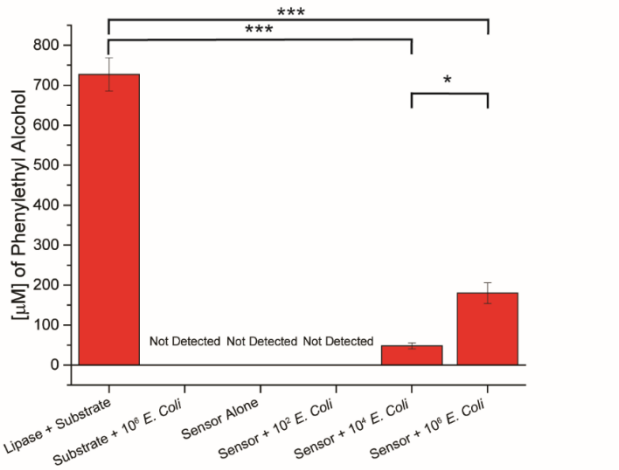

Figure 4.6: Headspace gas chromatography analysis of sensor response to increasing concentrations of bacteria. Samples were prepared in triplicate. Error bars represent standard deviations of the measurements. *= $p < 0.05$, ***=$p<0.001$.

4.3. Conclusions

In summary, we report the development a supramolecular-based strategy to perceive molecular interactions with the human olfactory system. As a proof of concept, our NOSE was shown to be an effective bacterial sensor based on the selective production of olfactory detectable compounds. These studies demonstrated that by controlling the behavior at the molecular level of responsive nanomaterials we can alter how human beings observe their surroundings in a manner that is otherwise impossible. We believe this responsive strategy can be broadly applied to other surface functionalized nanoparticles and enzymes to generate arrays of reversibly bound enzyme-nanoparticle complexes. Further expanding this methodology allows the crafting of an almost limitless number of aroma profiles by using the readily available multitude of fragrance and enzyme combinations.

4.4. Experimental Methods

4.4.1. Materials

All reagents/materials were purchased from Fisher Scientific and used as received. Benzyl functionalized AuNPs were synthesized according to previous reports.[24]

4.4.2. Synthesis of Pro-fragrance

0.05 g of 4-dimethylaminopyridine and 0.983 g of succinic anhydride were dissolved in dry dichloromethane. 1 gram of phenylethyl alcohol was added to the reaction. The reaction was heated and refluxed overnight. Solvent was then removed and the product was dissolved in a saturated sodium bicarbonate solution. Aqueous layer was extracted with ethyl acetate. (2x) Aqueous layer was then acidified and extracted with dichloromethane. (3x) Dichloromethane layers were combined and dried over sodium sulfate. Solvent was removed and the obtained product was a white crystalline solid. Yield = 1.655 grams, 91%, m.p. = 68-70 ºC.

4.4.3. Bacteria Growth Conditions

Bacteria were cultured in LB medium at 37 °C and 275 rpm until stationary phase. The cultures were then harvested by centrifugation and washed with 0.85 % sodium chloride solution for three times. Concentrations of resuspended bacterial solution were determined by optical density measured at 600 nm. 5 mM sodium phosphate buffer was used to make dilutions of bacterial solutions of 10^8,10^6, and 10^4 cfu/mL.

4.4.4. Plate Reader Assay Conditions

Lipase inhibition assay was done at 25 °C with the final concentrations in Costar clear 96 well plate of 15 nM Lipase, 0.6 mM pNPB, and 20, 40, 60, 80, 100, 125, 150 nM benzyl

AuNP. Lipase and benzyl AuNP were first incubated for 30 minutes in 96 well plate to insure their interaction reaches equilibrium, then 10 µL of substrate p-NPB was added into the well. The activity of lipase was monitored every 30 seconds for a total of 40 minutes time frame at the absorbance of 405 nm.

4.4.5. Human Trial Assays

4.4.5.1. Olfactory Detection of Lipase Activity

Four different solutions were made in 20 mL glass vials with a final volume of 1 mL each. 5 mM sodium phosphate buffer and 4 mM SAME were used as the negative controls and the rose scent (2-Phenylethyl ethanol) was used as the positive control, a strong standard. The activity of lipase was assessed by incubating 100 nM of lipase with 4 mM of SAME for 20 minutes. The participants were asked to smell these samples and rank them in the order from 1 to 5 with 1 has the lightest smell and 5 has the strongest smell.

4.4.5.2. Olfactory Detection of *E. Coli*

The same procedure was followed as above for buffer and sensor samples. For the *E. Coli*-containing vials, 100 nM Lipase was incubated with 300 nM Benzyl AuNP for 30 minutes, and then 10 µL of *E. Coli* was added into each vial so that the final concentrations of *E. Coli* in each vial are 10^2 and 10^4 cfu/mL.

4.4.6. Gas Chromatography Head-Space Analysis

Headspace phenylethyl alcohol was measured using a gas chromatograph (model GC-17A, Shimadzu Co., Tokyo, Japan) equipped with a solid-phase microextraction (SPME) auto injector (model AOC-5000, Shimadzu Co., Tokyo, Japan). Samples (1 mL) in 20

mL glass vials capped with aluminum caps with polytetrafluoroethylene (PTFE)/silicone septa. Samples were prepared using 500 nM lipase, 1.5 μM benzyl AuNP, and 4 mM of SAME. A 50/3 μm divinylbenzene (DVB)/carboxen/polydimethylsiloxane (PDMS) stable flex (SPME) fiber (Supelco Co., Bellefonte, PA) was then inserted into the vial headspace for 2 min to absorb volatiles. The fiber was transferred to the GC injector port (250 °C) for 3 min. The injection port was operated in split mode, and the split ratio was set at 20:1. Volatiles were separated on a fused-silica capillary Equity-1 Supelco column (30 × 0.25 mm inner diameter × 25 μm) coated with 100% PDMS at an initial oven temperature of 70 °C to final temperature of 220 °C over 10 min (step rate 15 °C/min). A flame ionization detector was used at a temperature of 250 °C. Phenylethyl alcohol concentrations were determined from peak areas using a standard curve made from dilutions of phenylethyl alcohol in 5 mM sodium phosphate buffer. Each measurement was performed in triplicate and results were expressed as mean values ± standard deviation.

4.5. References

(1) Sela, L.; Sobel, N. *Exp. Brain Res.* **2010**, *205*, 13.

(2) Bushdid, C.; Magnasco, M. O.; Vosshall, L. B.; Keller, A. *Science* **2014**, *343*, 1370.

(3) Dunkel, A.; Steinhaus, M.; Kotthoff, M.; Nowak, B.; Krautwurst, D.; Schieberle, P.; Hofmann, T. *Angew. Chem. Int. Ed.* **2014**, *53*, 7124.

(4) Hellwig, M.; Henle, T. *Angew. Chem. Int. Ed.* **2014**, *53*, 10316.

(5) Solov'yov, I. A.; Chang, P.-Y.; Schulten, K. *Phys. Chem. Chem. Phys.* **2012**, *14*, 13861.

(6) Whitesides, G. M. *Angew. Chem. Int. Ed.* **2015**, *54*, 3196.

(7) Saha, K.; Bajaj, A.; Duncan, B.; Rotello, V. M. *Small* **2011**, *7*, 1903.

(8) Miranda, O. R.; Creran, B.; Rotello, V. M. *Curr. Opin. Chem. Biol.* **2010**, *14*, 728.

(9) Miranda, O. R.; Li, X.; Garcia-Gonzalez, L.; Zhu, Z.; Yan, B.; Bunz, U. H. F.; Rotello, V. M. *J. Am. Chem. Soc.* **2011**, *133*, 9650.

(10) Tang, R.; Moyano, D. F.; Subramani, C.; Yan, B.; Jeoung, E.; Tonga, G. Y.; Duncan, B.; Yeh, Y.-C.; Jiang, Z.; Kim, C.; Rotello, V. M. *Adv. Mater.* **2014**, *26*, 3310.

(11) Tonga, G. Y.; Saha, K.; Rotello, V. M. *Adv. Mater.* **2014**, *26*, 359.

(12) Duncan, B.; Landis, R. F.; Jerri, H. a; Normand, V.; Benczédi, D.; Ouali, L.; Rotello, V. M. *Small* **2015**, *11*, 1302.

(13) Kuhnt, T.; Herrmann, A.; Benczédi, D.; Foster, E. J.; Weder, C. *Polym. Chem.* **2015**, *6*, 6553.

(14) Kuhnt, T.; Herrmann, A.; Benczédi, D.; Weder, C.; Foster, E. J. *RSC Adv.* **2014**, *4*, 50882.

(15) You, C.-C.; Miranda, O. R.; Gider, B.; Ghosh, P. S.; Kim, I.-B.; Erdogan, B.; Krovi, S. A.; Bunz, U. H. F.; Rotello, V. M. *Nat. Nanotechnol.* **2007**, *2*, 318.

(16) WHO, UNICEF (2014) Progress on drinking water and sanitation: 2014 Update. Geneva, Switzerland: WHO Press.

(17) WHO (2011) Guidelines for drinking-water quality -4th ed. Geneva, Switzerland: WHO Press.

(18) Li, X.; Robinson, S. M.; Gupta, A.; Saha, K.; Jiang, Z.; Moyano, D. F.; Sahar, A.; Riley, M. A.; Rotello, V. M. *ACS Nano* **2014**, *8*, 10682.

(19) Miller, K. P.; Wang, L.; Benicewicz, B. C.; Decho, A. W. *Chem. Soc. Rev.* **2015**, *44*, 7787.

(20) Jeong, Y.; Duncan, B.; Park, M.-H.; Kim, C.; Rotello, V. M. *Chem. Commun. (Camb).* **2011**, *47*, 12077.

(21) Herrmann, A. *Angew. Chem. Int. Ed.* **2007**, *46*, 5836.

(22) Tsukatani, T.; Miwa, T.; Furukawa, M.; Costanzo, R. M. *Chem. Senses* **2003**, *28*, 25.

(23) Philpott, C. M.; Wolstenholme, C. R.; Goodenough, P. C.; Clark, A.; Murty, G. E. *J. Laryngol. Otol.* **2008**, *122*, 912.

(24) Tonga, G. Y.; Jeong, Y.; Duncan, B.; Mizuhara, T.; Mout, R.; Das, R.; Kim, S. T.; Yeh, Y.-C.; Yan, B.; Hou, S.; Rotello, V. M. *Nat. Chem.* **2015**, *7*, 597.

CHAPTER 5

HYBRID ORGANIC-INORGANIC COLLOIDAL COMPOSITE 'SPONGES' VIA INTERNAL CROSSLINKING

5.1. Introduction

Hybrid organic-inorganic nanocomposites have emerged as promising materials for a variety of applications such as photonic devices,[1] proton exchange membranes,[2] emulsifiers,[3] and encapsulation vehicles.[4] The intimate interactions between the organic and inorganic components on the nanometer scale produce structures that display improved stability and generate materials with properties not achievable using the individual components alone.[5,6] Modulation of the individual component compositions prior to composite formation provides further structural versatility arising from the 'bottom-up' assembly process.[7,8] Additionally, nanocomposites are readily amenable to post-functionalization, providing access to highly diverse functional structures on the nano and micro scales.[9,10, 11,12,13]

The *in situ* generation of porous nanocomposites of controlled sizes with functional payloads, however, remains a challenge.[14] Three widely used strategies for the creation of colloidal nanocomposites are *in situ* polymerization,[15] sol-gel based approaches,[16] and self-assembly.[17] Previously, Armes *et al.* have created interfacially active nanocomposites through the polymerization of monomer emulsions stabilized with silica sols.[18] van Blaaderen and coworkers developed a generalized method to produce hybrid colloids through the sol-gel deposition of inorganic precursors onto nanoparticles with adsorbed poly(vinylpyrrolidone).[19] The work of Möhwald and Caruso harnessed the self-assembly of polystyrene beads with silica nanoparticles to form composite

structures.[20] Pickering emulsions can also be used as self-assembled templates to generate complex functional materials.[21,22,23] These hybrid systems, however, are generally used to form core/shell structures as opposed to solid nanocomposite structures.

Herein, we describe a supramolecular/covalent strategy for the generation of hybrid organic-inorganic composites (Figure 5.1). In this process, hydrophilic amine-functionalized silica nanoparticles are assembled at the oil/water interface. Reaction of the particles with a hydrophobic copolymer increases the hydrophobicity of the particles, resulting in particle migration into the oil phase and confining the covalent bond formation to the interior of the emulsions. These covalent linkages between nanoparticles and polymers induces a change in configuration from a reservoir system to a network composite while preserving the discrete microparticle morphology generated by the emulsion process. These organic/inorganic hybrid systems are very robust, and show substantial retention of encapsulated hydrophobic payloads in the presence of ethanol without the need for post-functionalization or annealing after assembly. Furthermore, the use of non-toxic maleic anhydride-based polymers[24] facilitates the potential use of these robust systems for a variety of medical and personal care applications.

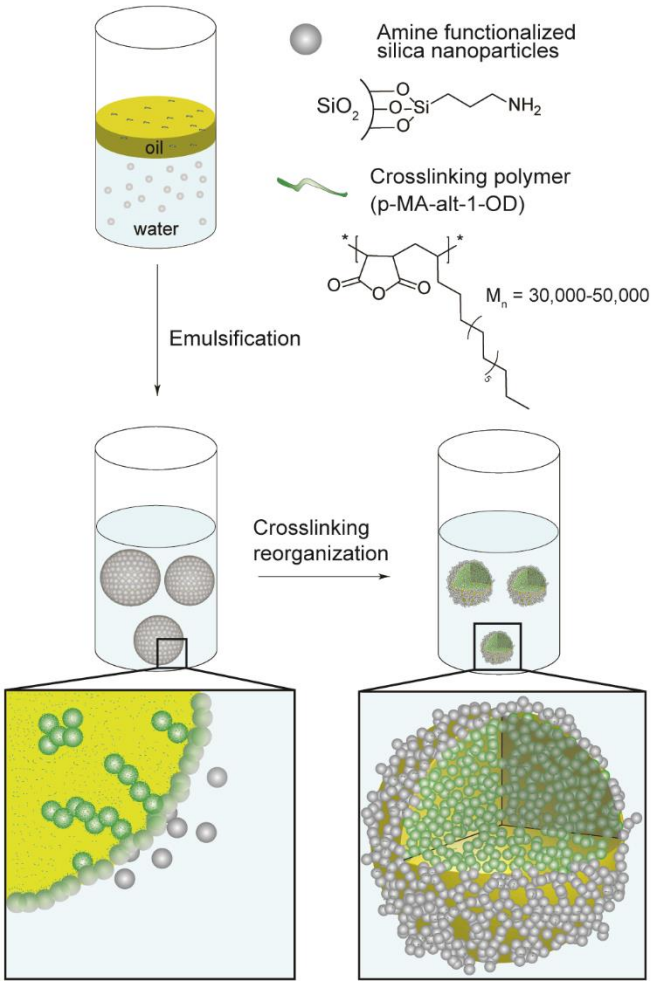

Figure 5.1: Schematic depiction of the method used to generate the crosslinked composites. Water-soluble silica nanoparticles go to the oil/water interface to generate particle-stabilized Pickering emulsions. The dissolved polymer in the oil phase reacts with the nanoparticles from the inside of the emulsion via a ring-opening reaction. The crosslinking reaction simultaneously pulls the nanoparticles into the oil phase as the nanoparticle surface becomes more hydrophobic, generating an oil-containing composite structure.

5.2. Results and Discussion

5.2.1. Formulation of hybrid inorganic-organic nanocomposites

Emulsions were generated according to the route depicted in Figure 5.1. Briefly, the hydrophobic polymer was dissolved in the oil prior to emulsification, with limonene used as a model hydrophobic oil. Concurrently, silica nanoparticles were suspended in

Milli-Q water and the solution was adjusted to a pH of 10 with sodium hydroxide to deprotonate the surface amines and promote covalent attachment to the polymer.[25] The oil phase was added to the aqueous phase and homogenized at 24,000 rpm for two minutes. Homogenization speeds lower than 24,000 rpm produced larger emulsions with higher degrees of polydispersity (Figure 5.2). Stable emulsions could be formed at silica loadings ranging from 0.6 to 2.0 wt % (Figure 5.3, 5.4, 5.5). Polymer loading into the oil phase did not appear to alter the emulsion morphology or size (Figure 5.6). Emulsions were then allowed to crosslink overnight at room temperature.

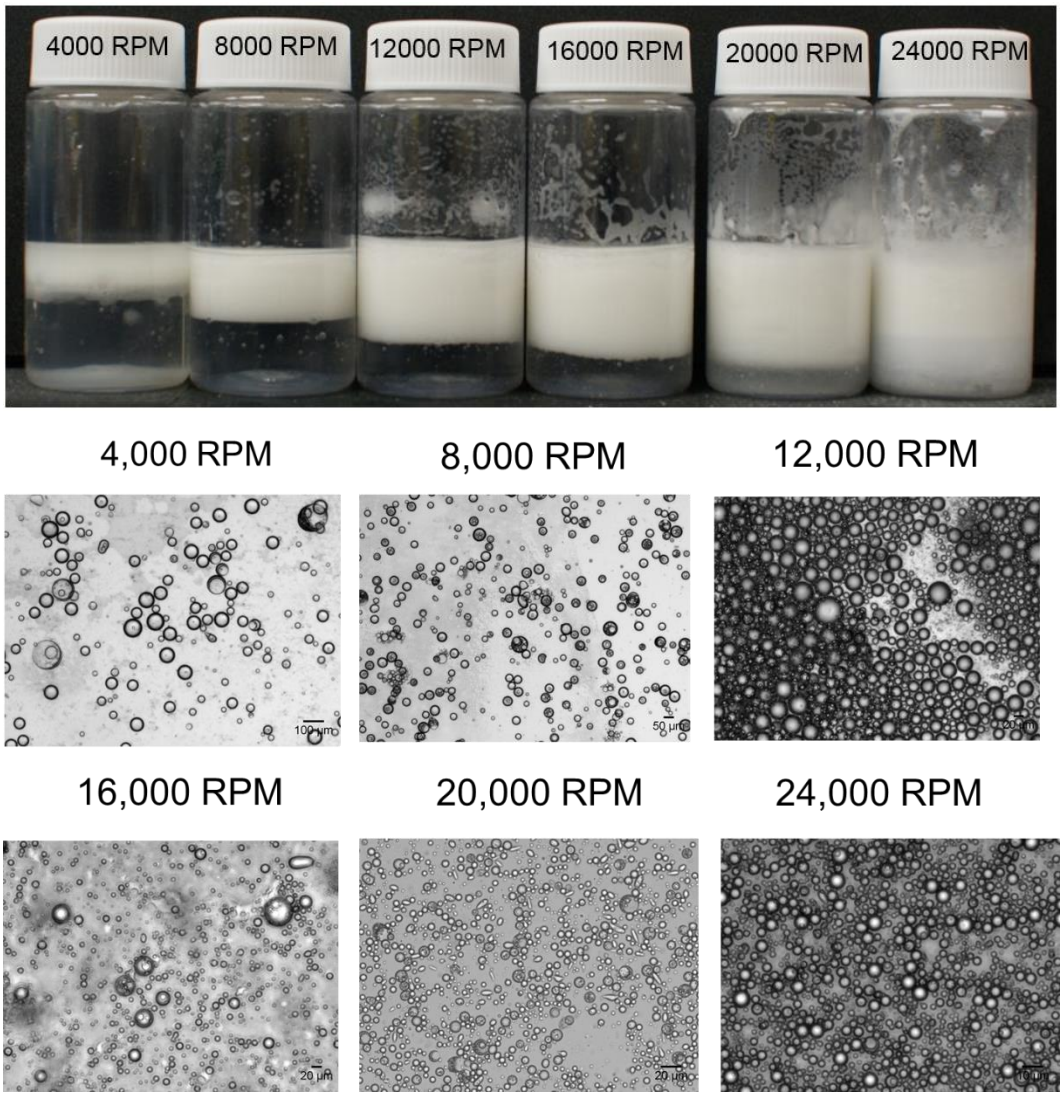

Figure 5.2: Photograph and bright field microscopy images of composites generated using different homogenization speeds. Composites were generated by emulsifying 2 mL of 5 wt % p-MA-alt-1-OD in limonene into 8 mL of 1.5 wt % silica nanoparticles in Milli-Q adjusted to pH 10 for 2 minutes. Homogenization speeds lower than 24,000 rpm resulted in larger emulsions with more polydispersity.

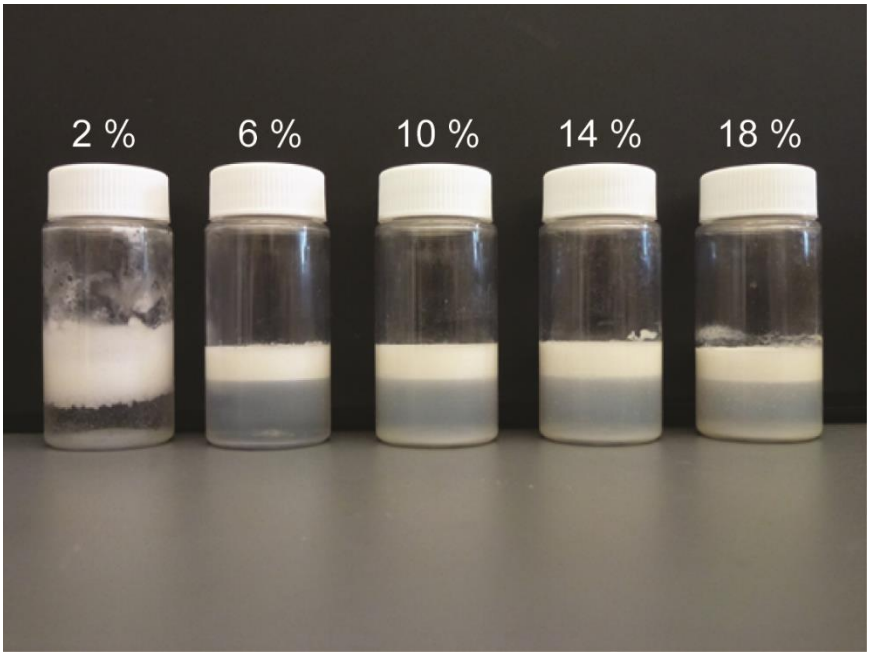

Figure 5.3: Image of composites after one week of storage. Composites were generated by emulsifying 2 mL of varying wt % p-MA-alt-1-OD in limonene into 8 mL of 0.6 wt % silica nanoparticles in Milli-Q adjusted to pH 10 for 2 minutes at 24,000 RPM.

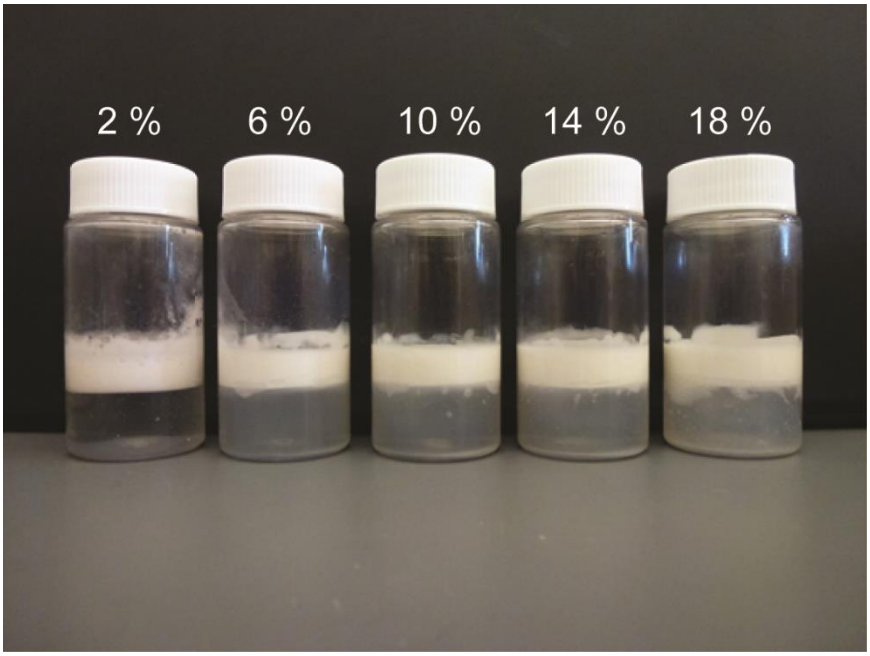

Figure 5.4: Image of composites after one week of storage. Composites were generated by emulsifying 2 mL of varying wt % p-MA-alt-1-OD in limonene into 8 mL of 1.2 wt % silica nanoparticles in Milli-Q adjusted to pH 10 for 2 minutes at 24,000 RPM.

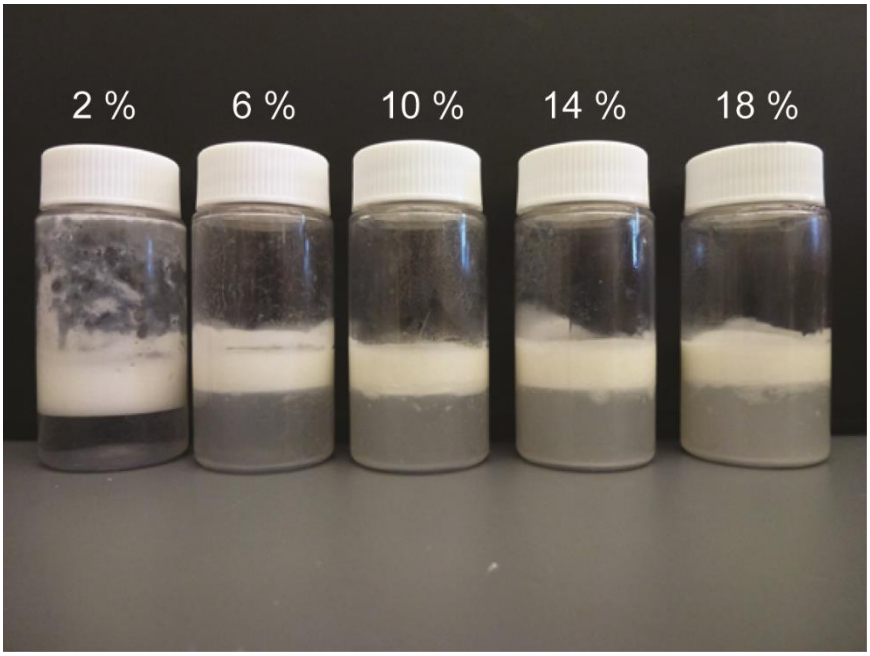

Figure 5.5: Image of composites after one week of storage. Composites were generated by emulsifying 2 mL of varying wt % p-MA-alt-1-OD in limonene into 8 mL of 2.0 wt % silica nanoparticles in Milli-Q adjusted to pH 10 for 2 minutes at 24,000 RPM.

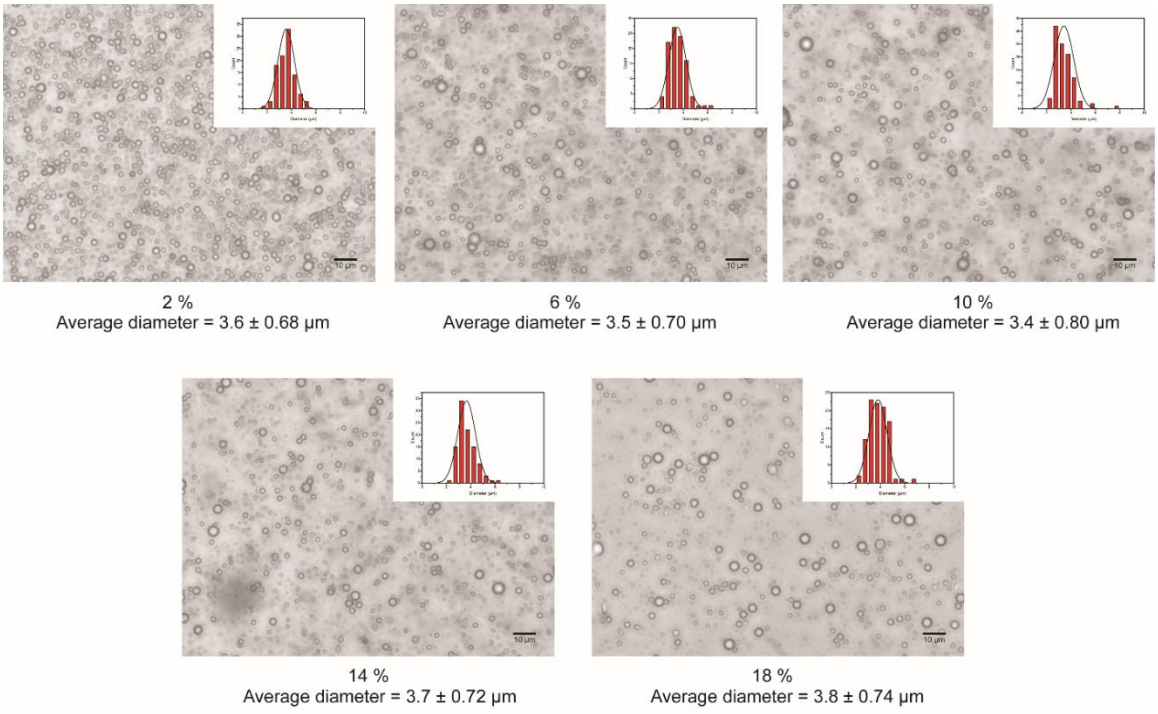

Figure 5.6: Bright field microscopy images of composites generated with increasing polymer loadings in the oil phase. Composites were generated by emulsifying 2 mL of varying wt % p-MA-alt-1-OD in limonene into 8 mL of 1.5 wt % silica nanoparticles in Milli-Q adjusted to pH 10 for 2 minutes at 24,000 RPM.

5.2.2. Composite characterization

Confocal microscopy was used to probe the structure of the particle-stabilized emulsion droplets and visualize the assembly of nanoparticles at the oil/water interface. Amine-functionalized silica nanoparticles with cores containing fluorescein isothiocyanate (FITC) were used to track the location of the silica nanoparticles. An aqueous dispersion of these nanoparticles was emulsified with the organic phase comprising limonene, hydrophobic Nile Red dye and p-MA-alt-1-OD crosslinking polymer. Figure 5.7a-d shows the co-distribution of the nanoparticles and the Nile Red containing oil phase, suggesting this system does not have the typical core shell structure of a Pickering emulsion. The average size of the generated composites (2 mL of 5 wt % p-MA-alt-1-OD in Nile Red loaded limonene: 8 mL of 1.5 wt % silica nanoparticles in Milli-Q adjusted to pH 10) was 4.2 ± 1.2 μm as determined using microscopy image analysis. As shown in Figure 5.7e, control studies performed without the crosslinking polymer in the oil phase formed structures with a core-shell morphology.

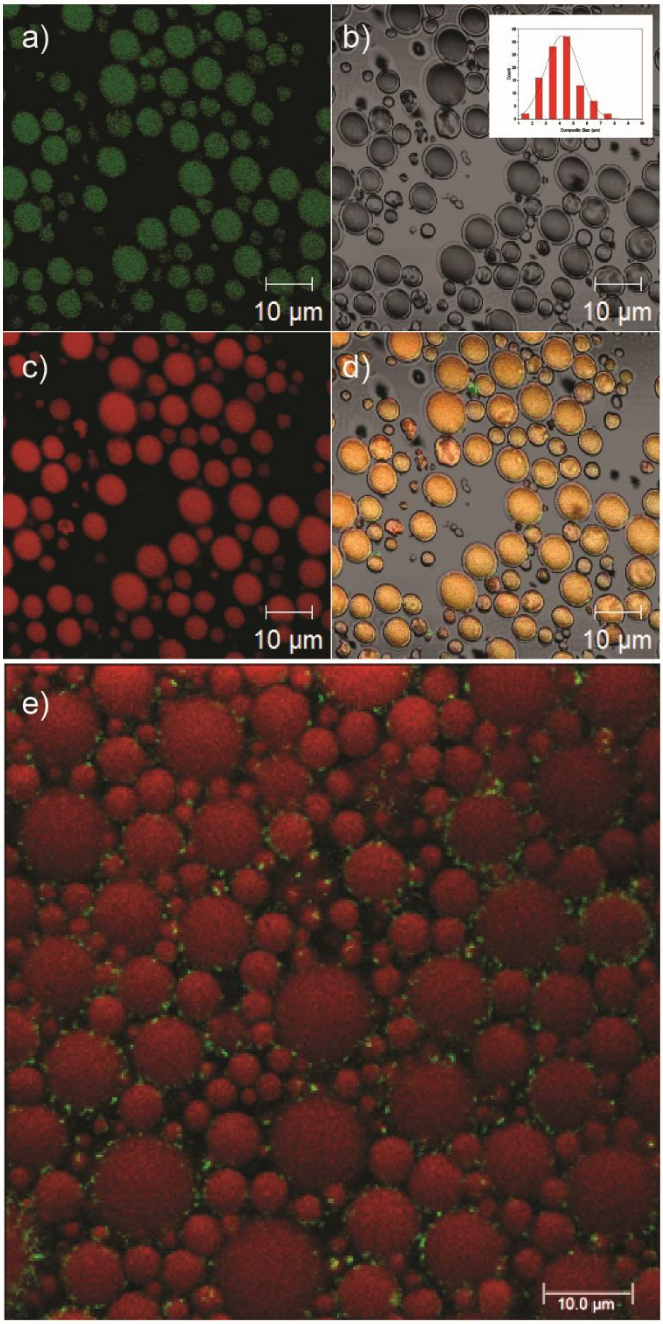

Figure 5.7: Confocal images of FITC-labeled nanoparticles with Nile Red loaded oil phase. a) The green fluorescence channel shows the FITC-labeled silica nanoparticles are present at the surface and in the core of the composite. b) Bright field image of the composite. Inset shows composite size distribution. c) Red fluorescence channel shows the Nile Red-loadedorganic phase containing limonene and crosslinking polymer p-MA-alt-1-OD . d) The merged fluorescence image provides an overlay of the co-localized green fluorescent nanoparticles with the red fluorescent oil core. e) Merged fluorescence image of uncrosslinked Pickering emulsions, showing core-shell morphology.

The colocalization of the hydrophobic dye and nanoparticle fluorescence signals in Figure 5.7d suggested that structures distinct from core-shell Pickering emulsions were produced during the crosslinking step. Further demonstration of this morphological transition was provided using Z-stacked confocal microscopy (Figure 5.8) and optically cross-sectioning crosslinked microparticles immobilized in an agar medium. The polymer crosslinked structures displayed a 3D composite structure consistent with the images in Figure 5.7, where the nanoparticles (green) and Nile red containing oil are co-distributed throughout the composite as confirmed by the sequential series of optical slices in Figure 5.8.

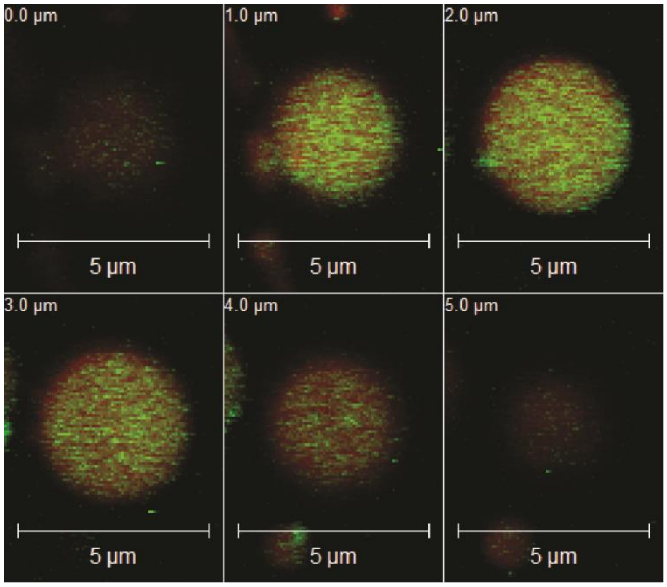

Figure 5.8: Confocal microscopy cross-sections of a composite structure. Images were taken in 1 µm slices. Green fluorescence from the nanoparticles and red fluorescence from the Nile red was colocalized in the oil core of the composite.

Scanning electron microscopy (SEM) and transmission electron microscopy (TEM) were used to further study the structure of the composite and the morphological stability of these crosslinked composites under drying conditions. SEM of the

crosslinked composites (2 mL 5 wt % p-MA-alt-1-OD in Limonene: 8 mL 1.5 wt % silica nanoparticles in Milli-Q water) dried from aqueous solution show silica nanoparticles densely packed into spherical structures (Figure 5.9a, b, Figure 5.10). TEM images show intact spheres that are in agreement with SEM results (Figure 5.9c, d).

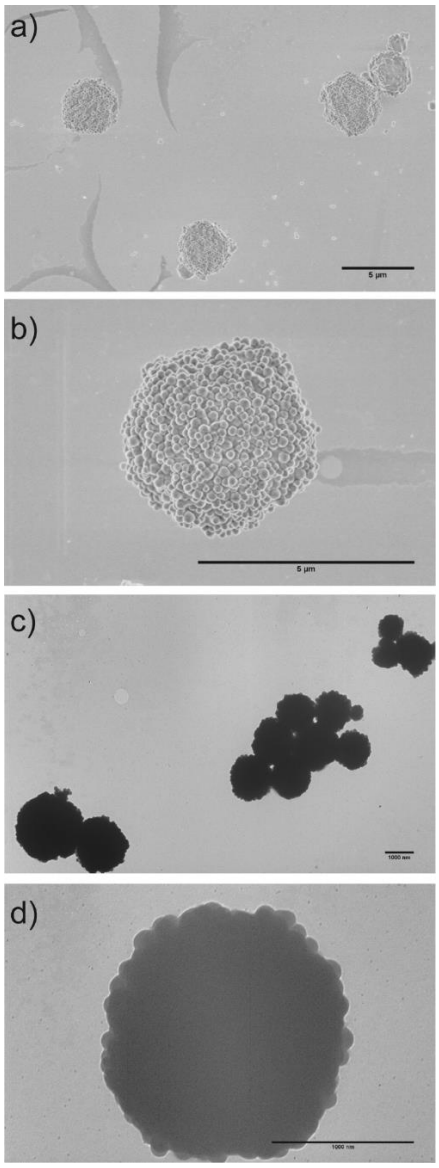

Figure 5.9: a,b) SEM images show densely packed silica nanoparticle and polymer composites. c,d) TEM images of dried composites show intact spheres, studded with silica nanoparticles. Composites were formed by emulsifying 2 mL of 5 wt % p-MA-alt-1-OD in limonene into 8 mL of 1.5 wt % silica nanoparticles in Milli-Q water.

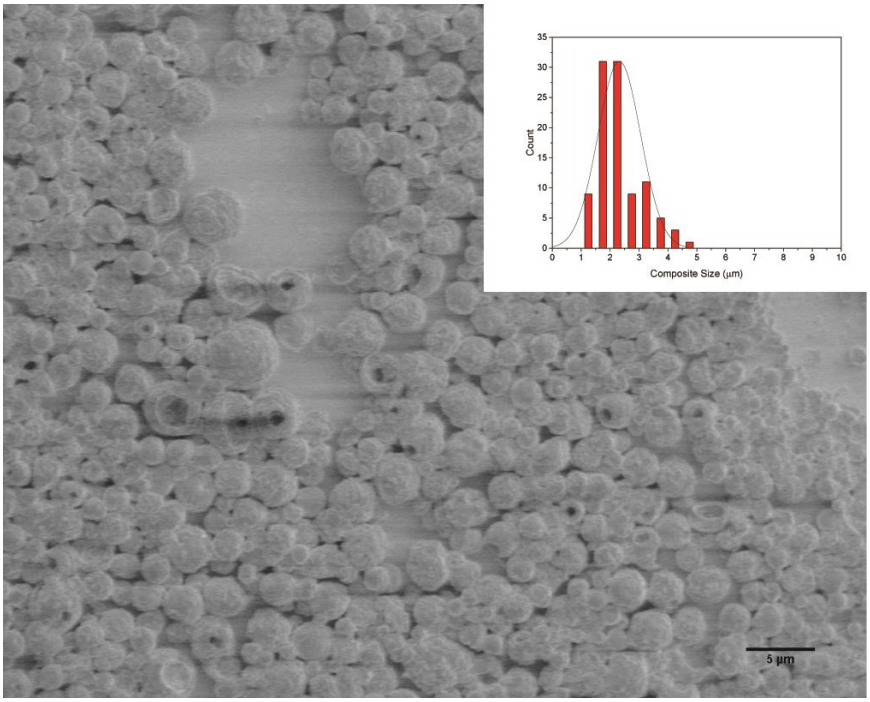

Figure 5.10: Scanning electron microscopy image of dried composite structure. Inset displays composite size distribution. Composites have an average diameter of 2.3 ± 0.72 μm. Composites were generated by emulsifying 2 mL of 5 wt % p-MA-alt-1-OD in limonene into 8 mL of 1.5 wt % silica nanoparticles in Milli-Q adjusted to pH 10 for 2 minutes at 24,000 RPM.

Having established the morphology of the composites, we next focused on characterizing the chemical processes involved in the crosslinking step. Infrared attenuated total reflectance Fourier transform (ATR-FT-IR) spectroscopy was performed on the amine-functionalized silica nanoparticles, p-MA-alt-1-OD, and the crosslinked composites (2 mL of 12 wt % p-MA-alt-1-OD in limonene: 8 mL of 1.5 wt % silica nanoparticles in Milli-Q adjusted to pH 10) to confirm crosslinking between the nanoparticles and the polymer backbone (Figure 5.11). The crosslinked composites displayed spectra in agreement with the absorbance spectra shown by both the nanoparticles and polymer individually. The composites, however, showed a loss of the maleic anhydride peak and the formation of an absorbance at 1712 cm^{-1} attributed to the

carboxylic acid functionality arising from the ring opening of the maleic anhydride. Broad absorption around 2500 - 3250 cm^{-1} likewise supports formation of a carboxylic acid functional group.

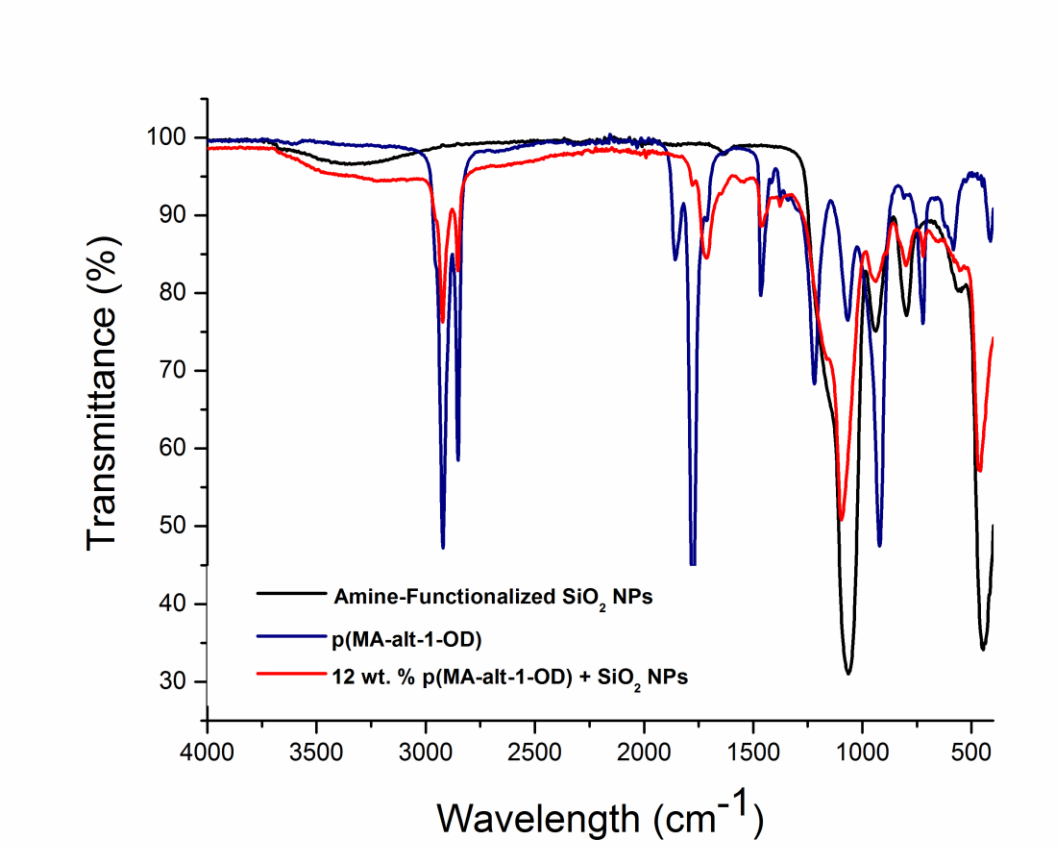

Figure 5.11: ATR-FT-IR characterization of the silica nanoparticles, p-MA-alt-1-OD, and crosslinked composites after composite formation and freeze-drying. Amine functionalized silica nanoparticles show characteristic peaks at 3280 cm^{-1}, 1063 cm^{-1}, and 936 cm^{-1} attributed to the Si-O and Si-OH frequencies. Maleic anhydride frequencies at 1856 cm^{-1} and 1774 cm^{-1} were identified in the polymer along with the octadecane at 2920 cm^{-1} and 2851 cm^{-1}. The crosslinked composites possessed peaks at frequencies similar to both the nanoparticles and polymer. The ring opening of the maleic anhydride in the polymer was confirmed by the appearance of a peak 1712 cm^{-1} and the loss of the peak at 1856 cm^{-1}. Broad absorption around 2500 - 3250 cm^{-1} is attributed to the presence of the generated carboxylic acid functionality.

Further characterization of the crosslinking reaction was done by measuring the amount of remaining free amines on the surface of the nanoparticles after crosslinking.28 The quantification was done through a modified ninhydrin reaction and the external

calibration curve shown in Figure 5.12. The emulsions were generated through the emulsification of dichloromethane (to allow easy separation from the aqueous phase) with increasing amounts of dissolved polymer. The emulsions were reacted overnight to ensure the ring opening reaction had gone to completion. As shown in Figure 5.13, the amount of free amines decreases rapidly with increasing polymer concentrations, showing an almost complete reaction of the amines at higher polymer ratios. Amine-functionalized silica nanoparticles show 4 amines per square nanometer, in agreement with literature findings.[28] As the amine functionalities present on the surface of the nanoparticles react with the polymer, the colorimetric reaction with ninhydrin is reduced. The amine groups are nearly fully crosslinked by 18 wt % p-MA-alt-1-OD in the oil phase, with a greater extent of crosslinking corresponding to a lower particle loading.

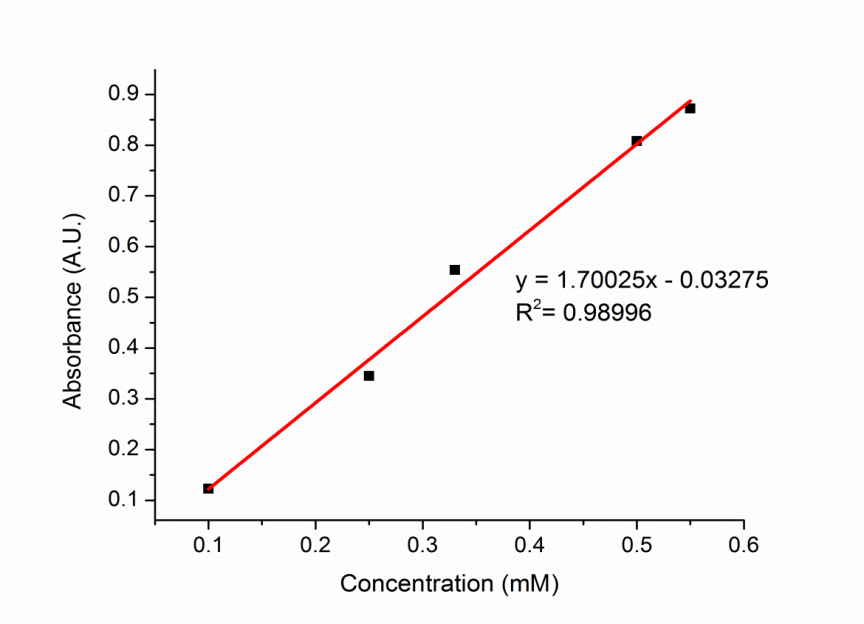

Figure 5.12: Calibration curve used to quantify amines was generated using 3-aminopropyltriethoxysilane (APS) and ninhydrin.

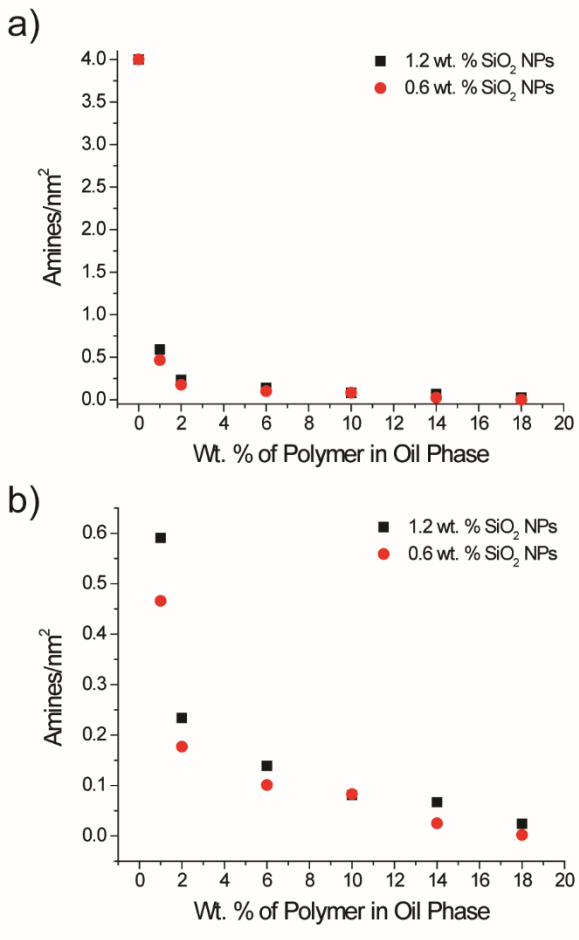

Figure 5.13: Remaining free amine concentration determined using a modified ninhydrin reaction with 2 silica loadings as a function of crosslinking polymer concentration. a) Amine-functionalized silica nanoparticles show 4 amines/nm^2 are available for crosslinking, and amines are readily crosslinked by the polymer with near complete consumption of the functional groups by 18 wt % p-MA-alt-1-OD. b) Expanded view of the near complete loss of amine functionality as polymer concentration increases.

The extent of the crosslinking reaction was also examined as a function of pH (Figure 5.14, 5.15, 5.16). We hypothesized that an increase in maleic anhydride units within the oil would form more carboxylic acid units and decrease the pH of the system. To test this hypothesis, the polymer concentration in the oil phase was increased with the amount of silica held constant and the pH of the emulsified mixture was then monitored over time. As expected, an increase in polymer concentration induces the pH of the total

system to lower. The greatest degree of pH change was observed for the highest polymer loading of 15 wt % p-MA-alt-1-OD in the limonene oil phase with the pH after emulsification being reduced from 8.5 to 5.5. Taken together, the IR results, the ninhydrin assay, and the generation of acid all support amine-anhydride crosslinking between the particles and polymer.

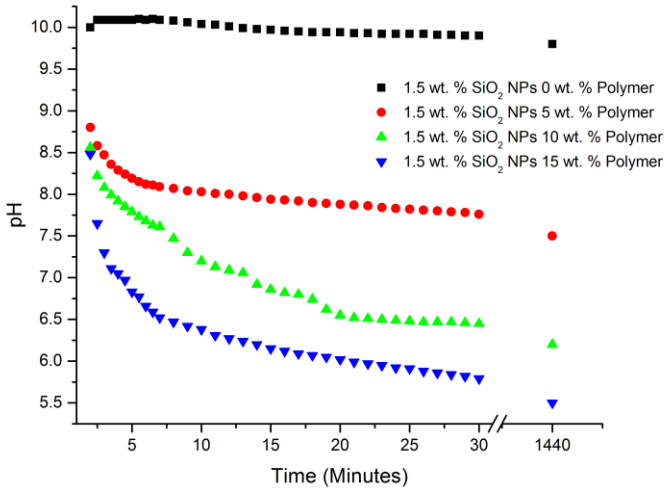

Figure 5.14: Tracking crosslinking kinetics by monitoring the decrease in pH due to formation of carboxylic acid groups during crosslinking of amine-functionalized silica nanoparticles by p-MA-alt-1-OD polymer in the oil phase. An increase in polymer concentration resulted in an appreciably lower pH once equilibrium was established, indicating that pH is a sensitive probe for reaction kinetics.

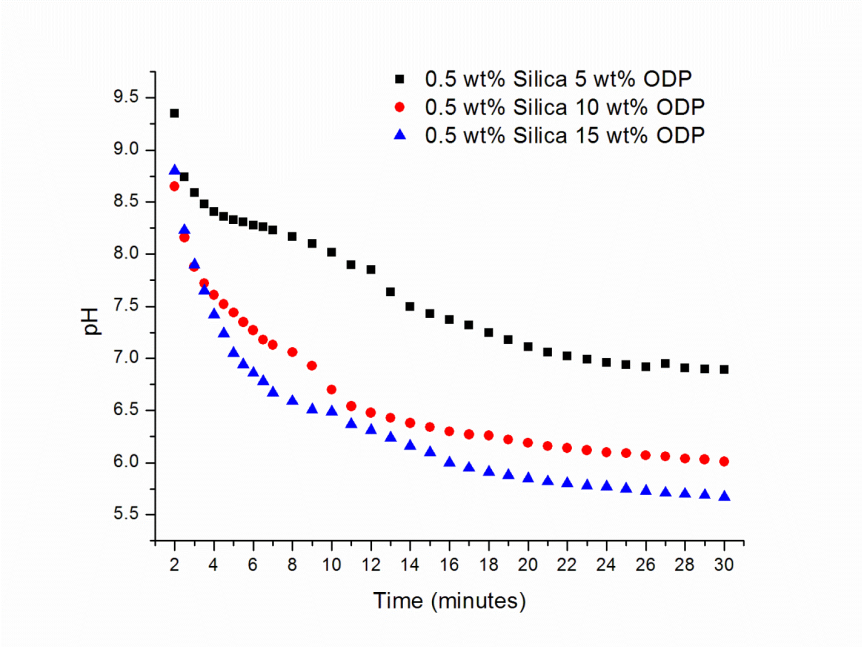

Figure 5.15: Plot of the decrease in pH over time with varying amounts p-MA-alt-1-OD in limonene. Composites were generated by emulsifying 2 mL of varying wt % p-MA-alt-1-OD in limonene into 8 mL of 0.5 wt % silica nanoparticles in Milli-Q adjusted to pH 10 for 2 minutes at 24,000 RPM. The reactions were measured by immersing a pH probe into the solution following emulsification.

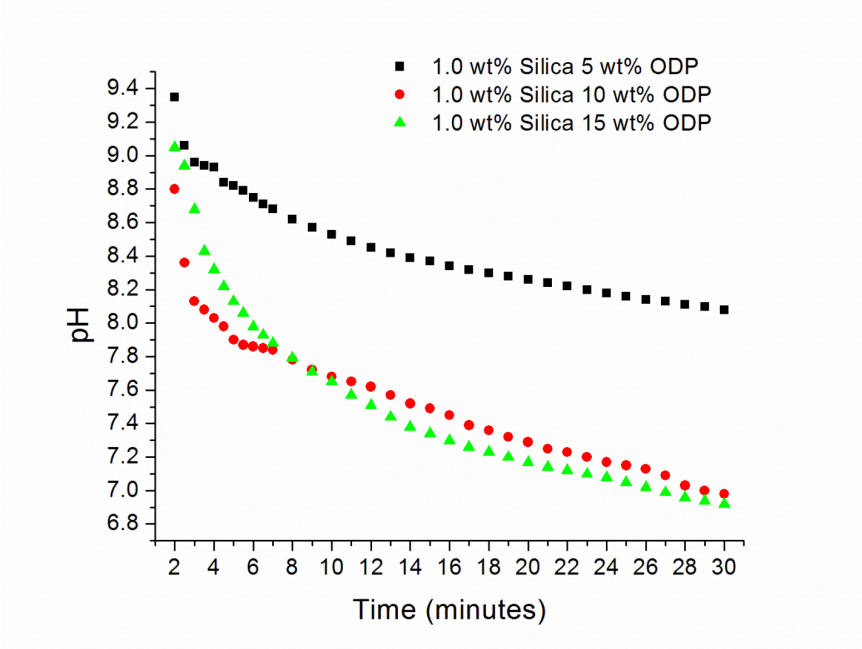

Figure 5.16: Plot of the decrease in pH over time with varying amounts p-MA-alt-1-OD in limonene. Composites were generated by emulsifying 2 mL of varying wt % p-MA-alt-1-OD in limonene into 8 mL of 1.0 wt % silica nanoparticles in Milli-Q adjusted to pH 10 for 2 minutes at 24,000 RPM. The reactions were measured by immersing a pH probe into the solution following emulsification.

5.2.3. Stability of Composites

To determine robustness and durability, the crosslinked composites were stored for one month. Figure 5.17a shows the composites prior to storage. After storage for one month, the composites do not undergo visible phase separation, indicating effective entrapment of the oil within the hybrid matrix. Additionally, the average size of the composites does not change significantly as shown in Figure 5.17b, though some change in distribution is observed. Although the composites creamed over time, this is attributed to the lower density, 0.8411 g/mL, of the limonene core compared to the continuous aqueous phase and is not indicative of leakage or instability (Figure 5.18). Polymer

loading did not significantly alter the particle size distributions of the resulting assemblies.

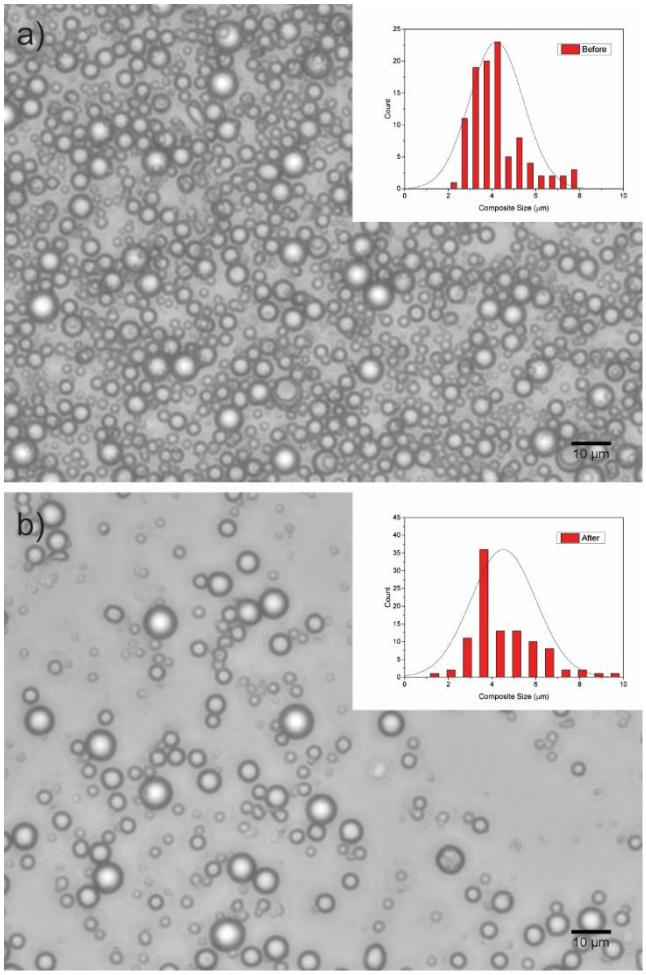

Figure 5.17: a) Bright field image of composites prior to storage. Inset shows distribution of composite sizes determined by image analysis. Composites had an average diameter of 4.2 ± 1.2 μm. b) Bright field image of composites after one month of storage. Inset shows distribution of composite size. Composites had an average diameter of 4.5 ± 1.5 μm.

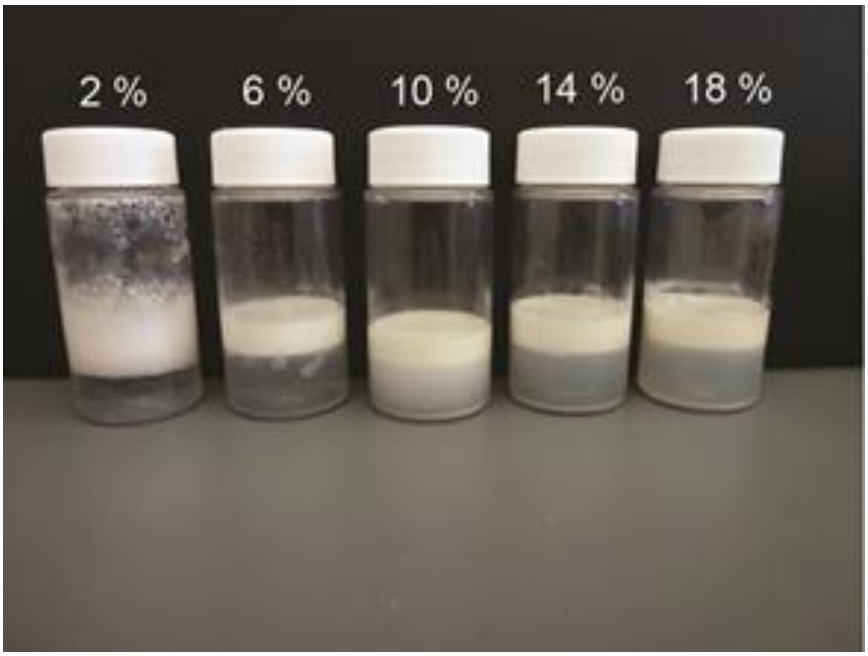

Figure 5.18: Image of the composites with varying wt. % of polymer dissolved in the limonene phase after one month of storage. Composites were generated by emulsifying 2 mL of varying wt % p-MA-alt-1-OD in limonene into 8 mL of 1.5 wt % silica nanoparticles in Milli-Q adjusted to pH 10 for 2 minutes at 24,000 RPM. Composite were sealed and stored for one month at room temperature.

5.2.4. Payload release by the crosslinked composites

Based on the structural studies above, we postulated that these materials should behave as porous 'sponges', retaining payload in competitive environments without dissociating. To test this possibility, we explored the release of payload from the nanocomposites in ethanol, using diphenyl ether as a tracer molecule. Diphenyl ether was chosen as an appropriate tracer due to its closely matching logP value of 4.21 compared to 4.23 for limonene. The addition of diphenyl ether (13 wt %) to the limonene did not affect the overall structure of the composite as determined by optical microscopy (Figure 5.19). There was no change in composite size upon incubation with ethanol as observed by optical microscopy, demonstrating the stability of these systems in an

environment of intermediate polarity (Figure 5.20). To quantify the leaching of payload in a model competitive medium, the composites were incubated for one hour in absolute ethanol. The composites were subsequently centrifuged and the UV-absorbance spectra of the supernatant was recorded to quantify release. As expected, an increase in polymer concentration increases the crosslinking density thereby reducing oil release, with capsules containing 5 wt % of polymer in the oil phase displaying maximum payload retention (Figure 5.21). At higher polymer concentrations, there was no additional payload retention, consistent with the complete reaction of the surface amines found in the ninhydrin assay. These results further support the hypothesis that the increasing number of covalent nanoparticle-polymer bonds reduces the permeability through the composite matrix.

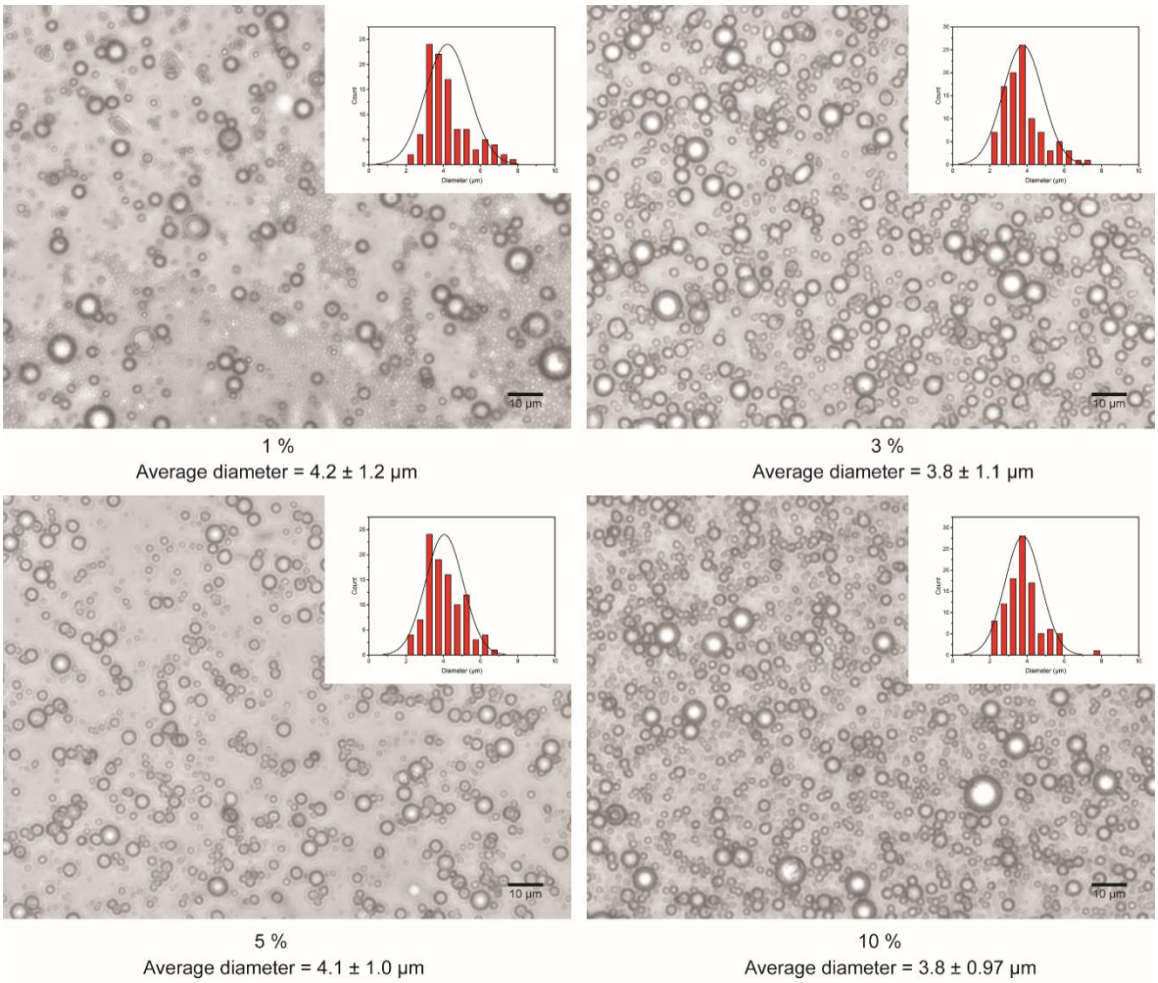

Figure 5.19: Bright field microscopy images of composites generated with increasing polymer loadings in the oil phase used for release quantification. Composites were generated by emulsifying 2 mL of varying wt % p-MA-alt-1-OD in a 13 % v/v mixture of diphenyl ether in limonene into 8 mL of 1.5 wt % silica nanoparticles in Milli-Q adjusted to pH 10 for 2 minutes at 24,000 RPM.

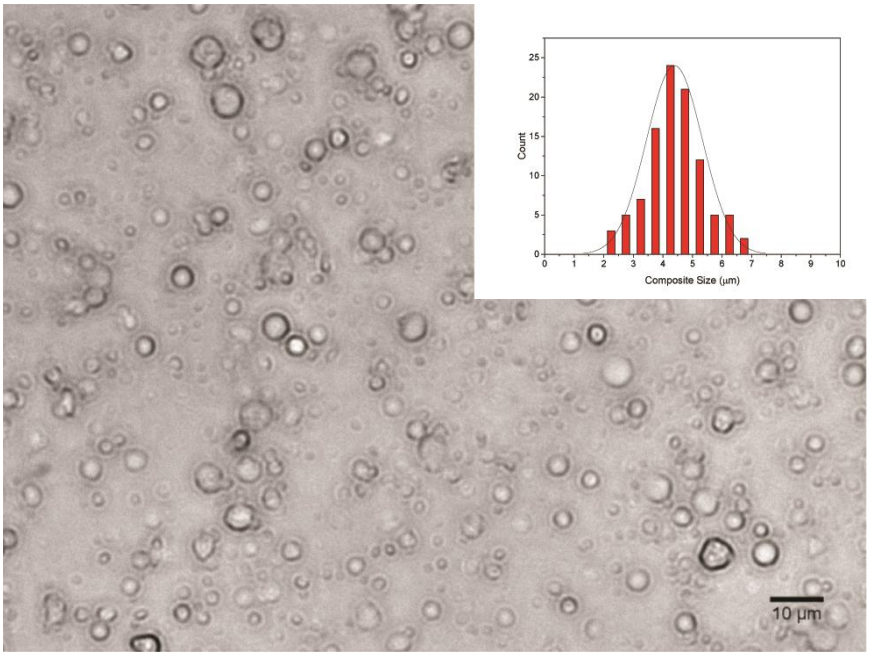

Figure 5.20: Bright field image of composites incubated with ethanol. Inset displays composite size distribution. Composites had an average diameter of 4.4 ± 0.9 μm. Composites were generated by emulsifying 2 mL of 5 wt % p-MA-alt-1-OD in a 13 % v/v mixture of diphenyl ether in limonene into 8 mL of 1.5 wt % silica nanoparticles in Milli-Q adjusted to pH 10 for 2 minutes at 24,000 RPM.

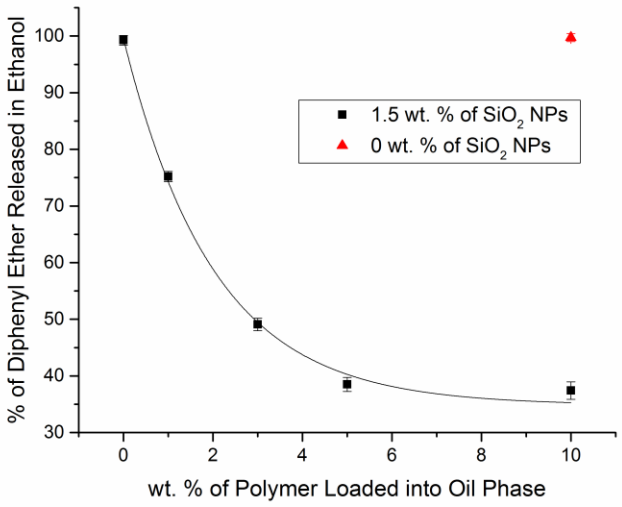

Figure 5.21: Release of diphenyl ether tracer from composites as a function of wt. % polymer dissolved in the limonene oil phase. Greater tracer retention was achieved by higher polymer loadings. The control capsules generated with the individual components showed complete release of payload. The curve was drawn to assist the eye.

5.3. Conclusions

We have shown that amine functionalized silica nanoparticles and maleic anhydride copolymers form stable size-controlled organic-inorganic hybrid composites from an oil/water emulsion template. Due to the alternating structure of the hydrophobic polymer used for the crosslinking, we hypothesize that this inside-out crosslinking method extensively connects the nanoparticles and alters the nanoparticles hydrophobicity at the oil/water interface, with the nanoparticles pulled into the oil core as their surfaces become more hydrophobic. These hybrid composites showed considerable resistance to the generally interface disrupting influence of ethanol. Future experiments will explore tuning the porosity of the structure through modification of the component precursors. The ability to parametrically vary the polymeric and inorganic components to tune the release behavior without greatly altering the vehicle's size is a particular

advantage over other porous delivery vehicles. These systems will also be probed for their effectiveness in multicomponent fragrance formulations and their ability to incorporate biomolecules into the composite structure for delivery and catalytic applications. Moreover, this Pickering emulsion-based strategy provides a potentially generalizable strategy to generate *in situ* reservoirs of hydrophobic molecules for multiple controlled release and delivery applications.

5.4. Experimental Methods

5.4.1. Materials

Tetraethyl orthosilicate (purity of 99%), 3-aminopropyl triethoxysilane (purity of 99%), ammonium hydroxide (28% ACS Plus), sodium hydroxide (purity of 97%), Nile Red (purity of 99%), fluorescein isothiocyanate isomer I (purity of 90%), agar (granulated, Fisher BioReagents^{TM}), diphenyl ether (purity of 99%), and 200 proof ethanol were purchased from Fisher Scientific and used as received. Poly(maleic anhydride-*alt*-1-octadecene) (p-MA-alt-1-OD; average M_n of 30,000-50,000) was purchased from Sigma-Aldrich and used as received. Limonene was provided by Firmenich Inc. Milli-Q water with a resistivity of 18.2 MΩ·cm was used for all experiments.

5.4.2. Synthesis and Functionalization of Silica Nanoparticles

The silica nanoparticles were synthesized using an adapted Stober method.[26] Briefly, to synthesize 150 nm amine functionalized silica nanoparticles, 24 mL of ammonium hydroxide were added to 300 mL of absolute ethanol and stirred for five minutes in a 500 mL round-bottom flask. Then 12 mL of tetraethyl orthosilicate were added to the reaction flask and stirred overnight at room temperature. To functionalize the surface of the nanoparticles, 1.22 mL of 3-aminopropyl triethoxysilane were added and the reaction was

stirred for an additional 24 hours. The nanoparticles were purified by centrifuging and re-dispersing in water and ethanol (3x each). The washed silica nanoparticles were lyophilized and used in powdered form. The nanoparticles had an average diameter of 150 ± 13 nm determined by transmission electron microscopy (TEM) and 165.1 ± 3.5 nm determined by dynamic light scattering (DLS), (Figure 5.22, 5.23). The nanoparticles had a zeta potential of +16.3 ± 3.6 mV in 5 mM sodium phosphate buffer (pH = 7.4), (Figure 5.24). Synthesis of fluorescein labeled nanoparticles[27] was performed following a similar method wherein 5.25 mg of fluorescein isothiocyanate were reacted with 69.0 mg of 3-aminopropyl triethoxysilane in one mL of absolute ethanol under nitrogen overnight. This fluorescent conjugate mixture was added to the nanoparticle reaction solution 5 minutes after the addition of tetraethyl orthosilicate. The procedure then proceeded as described above.

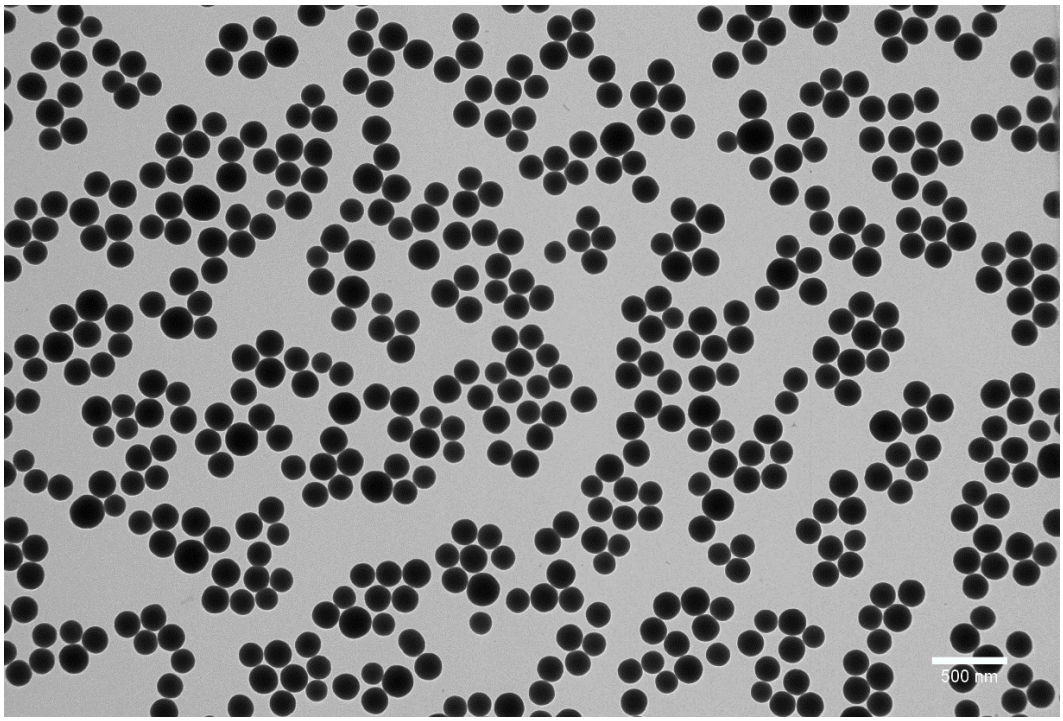

Figure 5.22: Transmission electron microscopy image of silica nanoparticles used throughout the study. Nanoparticles had an average diameter of 154 ± 13 nm.

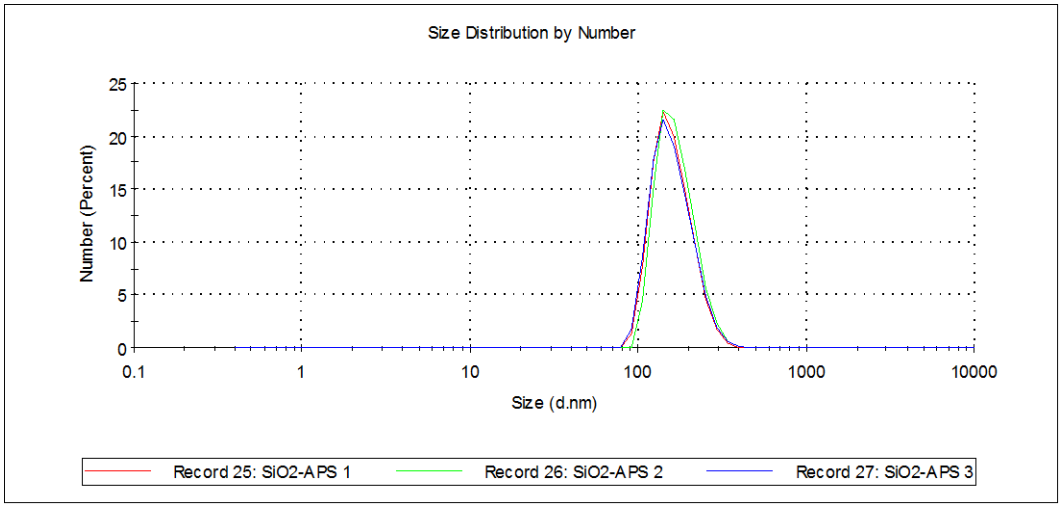

Figure 5.23: Average diameter by number of silica nanoparticles in MilliQ water as determined by dynamic light scattering was 165.1 ± 3.5 nm.

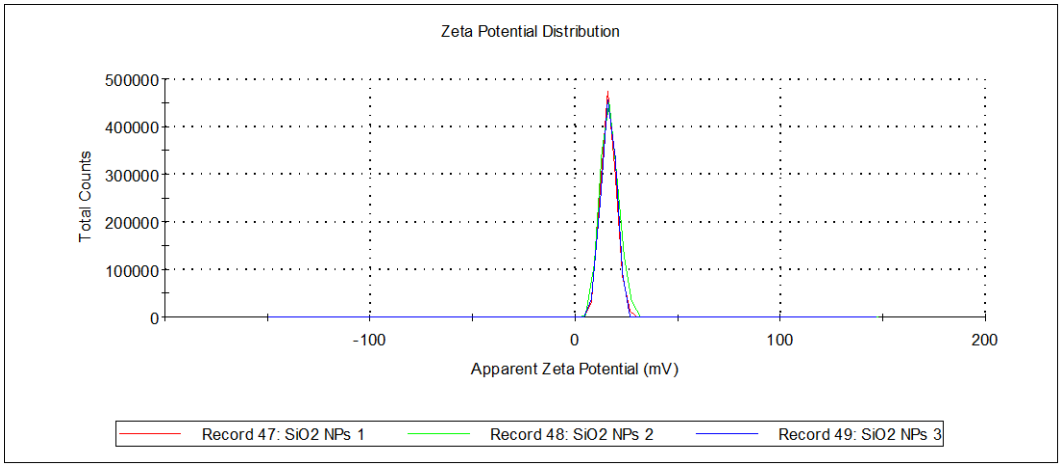

Figure 5.24: The average zeta potential of the silica nanoparticles was 16.3 ± 3.64 mV in 5 mM phosphate buffer adjusted to pH 7.4.

5.4.3. Microscopy and Particle Characterization

TEM samples were prepared on 300 square mesh nickel grids with Formvar film purchased from Electron Microscopy Sciences. TEM images were acquired on a JEOL 100CX operating at 100 keV. Scanning electron microscopy (SEM) data were obtained

using a FEI Magellan 400 field emission scanning electron microscope operated at 1.0 kV with 13 µA of beam current. Samples were prepared by drying diluted sample onto a boron-doped Si wafer purchased from WRS Materials. DLS data were measured with a Malvern Zetasizer Nano ZS. Optical and fluorescence images of the capsules were taken on an Olympus IX51 microscope. Confocal experiments were performed on a Zeiss LSM510 meta confocal microscope. Nile Red, a lipophilic fluorophore, was loaded into the oil phase at 0.05 wt. % to facilitate fluorescence microscopy. For the z-stack images the capsules were diluted into a 0.5 % w/w agar in water solution to reduce the Brownian motion of the matrix microparticles. ImageJ software was used to determine average diameters of composites for all microscopy methods.

5.4.4. Emulsification

Emulsions were generated using an IKA T 25 digital ultra-turrax disperser with an S25N-10G dispersing element. The 20 % v/v oil in water emulsions were made by emulsifying 2 mL of hydrophobic oil containing the hydrophobic polymer into 8 mL of pH 10 adjusted water with dispersed 150 nm amine functionalized silica nanoparticles at a homogenization speed of 24,000 RPM for two minutes. The as-formed emulsions were allowed to react for one day before characterization.

The formulation used for characterization unless otherwise specified was 2 mL of 5 wt % p-MA-alt-1-OD in limonene emulsified into 8 mL of 1.5 wt % silica nanoparticle solution in Milli-Q adjusted to pH 10.

5.4.5. ATR-FT-IR of Silica Nanoparticles, Polymer, and Freeze-dried Crosslinked Composite

IR was performed on a Bruker Alpha FT-IR spectrophotometer fitted with a Platinum ATR QuickSnap sampling module. The silica nanoparticles and polymer were analyzed as neat solids. The crosslinked composites were freeze-dried in order to obtain a dry solid that was analyzed in the same fashion.

5.4.6. Ninhydrin Assay for Amine Quantification

One mL of the crosslinked nanoparticle-stabilized composite solution was added to one mL of the generated stock ninhydrin solution (0.35 w/v % in pure ethanol) in a 7 mL glass vial and sealed. The vial was heated for 60 seconds; thereafter a blue/purple color was obtained. The vial was centrifuged at 14,000 rpm for 20 minutes, the supernatant was transferred to a cuvette, and the absorbance at 588 nm was recorded. This absorbance was compared to a generated calibration curve using 3-aminopropyl triethoxysilane and ninhydrin to determine the amount of free amine.[28]

5.4.7. Release Studies

Diphenyl ether was selected to be a tracer within the limonene core. The hydrophobic oil comprised 13 wt. % of diphenyl ether in limonene, and emulsions were formed in the same fashion as previously described. After the emulsions were allowed to react for one day, 100 µL of the emulsion slurry were incubated in 4 mL of absolute ethanol for one hour. The absorbance of the solution at 270 nm (the observed maximum absorbance of diphenyl ether) was recorded. A calibration curve was generated and used to determine the amount of diphenyl ether released into the ethanol.

5.5. References

(1) Wang, D.; Salgueiriño-Maceira, V.; Liz-Marzán, L. M.; Caruso, F. *Adv. Mater.* **2002**, *14*, 908.

(2) Saxena, A.; Tripathi, B. P.; Shahi, V. K. *J. Phys. Chem. B* **2007**, *111*, 12454.

(3) Fujii, S.; Read, E. S.; Binks, B. P.; Armes, S. P. *Adv. Mater.* **2005**, *17*, 1014.

(4) Arora, A.; Padua, G. W. *J. Food Sci.* **2010**, *75*, R43.

(5) Sanchez, C.; Shea, K. J.; Kitagawa, S. *Chem. Soc. Rev.* **2011**, *40*, 471.

(6) Balmer, J. A.; Schmid, A.; Armes, S. P. *J. Mater. Chem.* **2008**, *18*, 5722.

(7) Warren, S. C.; Perkins, M. R.; Adams, A. M.; Kamperman, M.; Burns, A. a; Arora, H.; Herz, E.; Suteewong, T.; Sai, H.; Li, Z.; Werner, J.; Song, J.; Werner-Zwanziger, U.; Zwanziger, J. W.; Grätzel, M.; DiSalvo, F. J.; Wiesner, U. *Nat. Mater.* **2012**, *11*, 460.

(8) Wahba, L.; D'Arienzo, M.; Donetti, R.; Hanel, T.; Scotti, R.; Tadiello, L.; Morazzoni, F. *RSC Adv.* **2013**, *3*, 5832.

(9) Yang, K.; Hu, L.; Ma, X.; Ye, S.; Cheng, L.; Shi, X.; Li, C.; Li, Y.; Liu, Z. *Adv. Mater.* **2012**, *24*, 1868.

(10) Park, M.-H.; Agasti, S. S.; Creran, B.; Kim, C.; Rotello, V. M. *Adv. Mater.* **2011**, *23*, 2839.

(11) Maeda, H.; Okada, M.; Fujii, S.; Nakamura, Y.; Furuzono, T. *Langmuir* **2010**, *26*, 13727.

(12) Behrens, S. *Nanoscale* **2011**, *3*, 877.

(13) Xu, P.; Han, X.; Zhang, B.; Du, Y.; Wang, H.-L. *Chem. Soc. Rev.* **2014**, *43*, 1349.

(14) Jancar, J.; Douglas, J. F.; Starr, F. W.; Kumar, S. K.; Cassagnau, P.; Lesser, A. J.; Sternstein, S. S.; Buehler, M. J. *Polymer (Guildf).* **2010**, *51*, 3321.

(15) Zou, H.; Wu, S.; Shen, J. *Chem. Rev.* **2008**, *108*, 3893.

(16) Ciriminna, R.; Fidalgo, A.; Pandarus, V.; Béland, F.; Ilharco, L. M.; Pagliaro, M. *Chem. Rev.* **2013**, *113*, 6592.

(17) Chen, T.; Colver, P. J.; Bon, S. A. F. *Adv. Mater.* **2007**, *19*, 2286.

(18) Fielding, L. A.; Armes, S. P. *J. Mater. Chem.* **2012**, *22*, 11235.

(19) Graf, C.; Vossen, D. L. J.; Imhof, A.; van Blaaderen, A. *Langmuir* **2003**, *19*, 6693.

(20) Caruso, F.; Caruso, R. A.; Möhwald, H. *Science* **1998**, *282*, 1111.

(21) Hsu, M. F.; Nikolaides, M. G.; Dinsmore, A. D.; Bausch, A. R.; Gordon, V. D.; Chen, X.; Hutchinson, J. W.; Weitz, D. A.; Marquez, M. *Langmuir* **2005**, *21*, 2963.

(22) Niu, Z.; He, J.; Russell, T. P.; Wang, Q. *Angew. Chemie Int. Ed.* **2010**, *49*, 10052.

(23) Jeong, Y.; Duncan, B.; Park, M.-H.; Kim, C.; Rotello, V. M. *Chem. Commun. (Camb).* **2011**, *47*, 12077.

(24) Qiu, G.-M.; Zhu, L.-P.; Zhu, B.-K.; Xu, Y.-Y.; Qiu, G.-L. *J. Supercrit. Fluids* **2008**, *45*, 374.

(25) Westcott, S. L.; Oldenburg, S. J.; Lee, T. R.; Halas, N. J. *Langmuir* **1998**, *14*, 5396.

(26) Stöber, W.; Fink, A.; Bohn, E. *J. Colloid Interface Sci.* **1968**, *26*, 62.

(27) Santra, S.; Liesenfeld, B.; Bertolino, C.; Dutta, D.; Cao, Z.; Tan, W.; Moudgil, B. M.; Mericle, R. a. *J. Lumin.* **2006**, *117*, 75.

(28) Soto-Cantu, E.; Cueto, R.; Koch, J.; Russo, P. S. *Langmuir* **2012**, *28*, 5562.

CHAPTER 6

NANOPARTICLE STABILIZED CAPSULES FOR THE TREATMENT OF BACTERIAL BIOFILMS

6.1. Introduction

Bacterial biofilms are highly resilient microbial assemblies that are difficult to eradicate.[1] These robust biofilms frequently occur on synthetic implants and indwelling medical devices including urinary catheters,[2] arthro-prostheses,[3] and dental implants.[4] Biofilm proliferation can also occur on dead or living tissues, leading to endocarditis,[5] otitis media,[6] and chronic wounds.[7] The persistent infections and their concomitant diseases are challenging to treat, as biofilms develop a high resistance to host immune responses and the extracellular polymeric substances limit antibiotic penetration into biofilms.[8,9] Current techniques to remove biofilms on man-made surfaces include disinfecting the surface with bleach or other caustic agents.[10] Biofilms in biomedical contexts are very challenging, with therapies based on excising infected tissues combined with long-term antibiotic therapy, incurring high health care costs and low patient compliance due to the invasive treatment.[11] This issue is exacerbated by the exponential rise in antibiotic resistant bacteria.[12]

Phytochemicals have emerged as an promising alternative to traditional antimicrobials to treat antibiotic resistant bacteria.[13,14] These essential oils and natural compounds are of particular interest as “green” antimicrobial agents due to their low-cost, biocompatibility, and potential anti-biofilm properties.[15,16,17] The generally poor aqueous solubility and stability of these oils has substantially limited their widespread

application.[18] Engineering nanomaterials provides a potential platform to prevent payload degradation and to tune molecular interactions with bacteria.[19,20,21,22] Previous reports have shown that encapsulating essential oils into surfactant-stabilized colloidal delivery vehicles improves their aqueous stability and increases the antimicrobial activity of small molecule payloads.[23,24,25] However, these carriers often induce adverse hemolytic or irritating effects restricting their compatibility with biological tissues.[26,27] Pickering emulsions provide an analogous route to encapsulate hydrophobic molecules within a self-assembled colloidal shell that is highly resistant to coalescence.[28,29] The multivalent nanoparticles embedded at the oil/water interface can also be post-functionalized to create structurally diverse carriers not achievable when using surfactant stabilized emulsions.[30,31]

Herein, we describe the fabrication of a multifunctional essential oil-based Pickering emulsion for the treatment of bacterial biofilms. The self-assembly strategy relies on hydrophobic phytochemicals playing both antimicrobial and structural roles for the drug delivery vehicle. Peppermint oil droplets provide the main hydrophobic core template for nanoparticle assembly. Dissolved cinnamaldehyde plays a dual role within the oil core by covalently reacting with the nanoparticles at the interface to modify the shell of the capsules from within and acting as a potent antimicrobial agent once delivered into the biofilm. These microcapsules effectively eradicate both laboratory and pathogenic biofilms. The inclusion of cinnamaldehyde also enhanced fibroblast proliferation[32] promoting therapeutic behavior of the capsules as demonstrated in an *in vitro* co-culture model. This work presents a versatile colloidal strategy for

multicomponent essential oil formulations with potential use as a general topical antimicrobial and disinfectant.

6.2. Results and Discussion

6.2.1. Generation and characterization of capsules

Silica nanoparticles (SiO_2 NPs) were chosen to stabilize the emulsions as they are biocompatible, surface functionalization can be easily introduced, and their diameters can be readily tuned.[31,33,34] Control over the size is especially important as nanomaterials smaller than 70 nm have been shown to readily penetrate the skin causing detrimental side-effects.[35,36,37] Therefore, we synthesized cationic amine-functionalized SiO_2 NPs with an average diameter of ~150 nm. (Figure 6.1, 6.2, 6.3) Antimicrobial capsules were generated using a Pickering emulsion template as shown in Figure 6.4. Capsules were created by emulsifying either peppermint oil or a mixture of cinnamaldehyde dissolved in peppermint oil into MilliQ H_2O adjusted to a pH of 10 containing the nanoparticles. The nanoparticles self-assemble at the oil/water interface to stabilize the peppermint oil droplets. Surface amines on the nanoparticles then react with the cinnamaldehyde within the oil phase. Silica loadings in the aqueous phase were varied to determine the amount needed to minimize capsule dispersity. At loadings above of 1.2 wt. % SiO_2 NPs or greater, capsules were found to have a minimum dispersity and therefore this amount was chosen for all further studies. (Figure 6.5) It was also observed that capsules generated with higher than 5 % v/v cinnamaldehyde were unstable which corresponds to 52-fold excess of cinnamaldehyde to available amines on the nanoparticle surface. (Figure 6.6) These peppermint oil based capsules (P-Cap) and capsules containing 5 % v/v of

cinnamaldehyde dissolved in peppermint oil (CP-Cap) were found to have average diameters of 6.8 ± 1.9 µm and 6.7 ± 1.9 µm, respectively. (Figure 6.7)

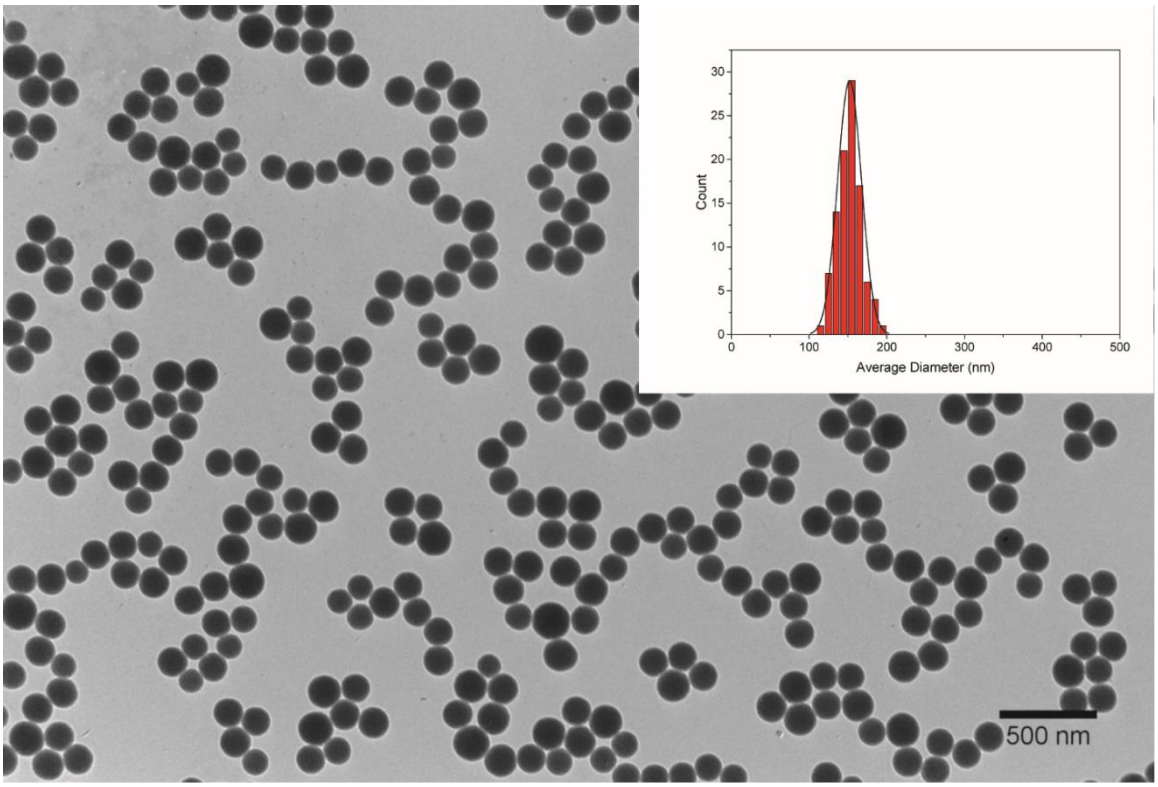

Figure 6.1: Transmission electron microscopy (TEM) image of silica nanoparticles. The nanoparticles had an average diameter of 152 ± 15 nm. Inset is a histogram of the measured nanoparticle diameters. Scale bar is 500 nm.

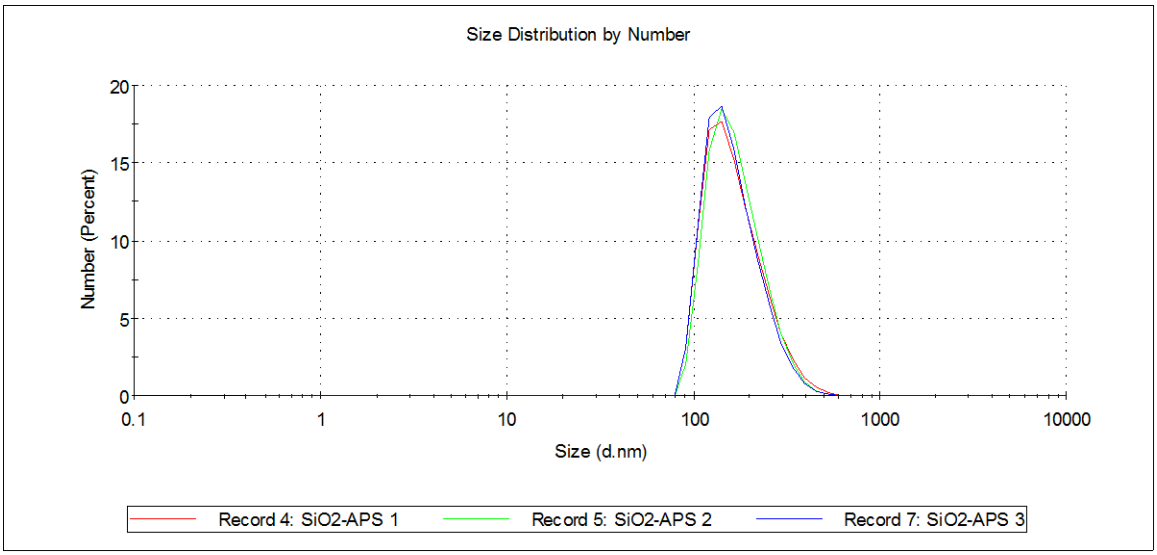

Figure 6.2: Average diameter of the silica nanoparticles in MilliQ H_2O was determined to be 171.5 ± 2.8 nm by dynamic light scattering (DLS).

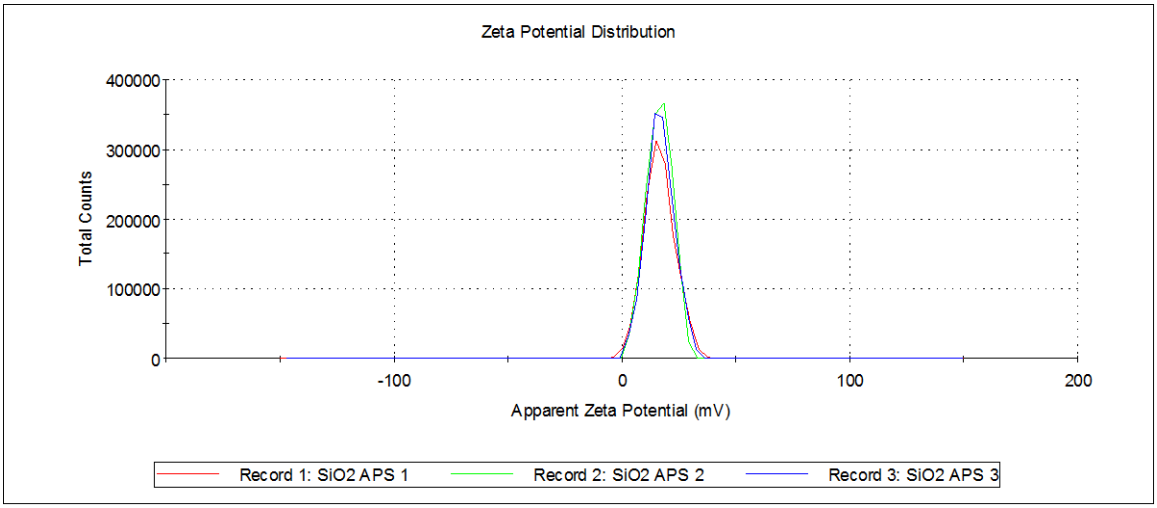

Figure 6.3: Zeta potential of the silica nanoparticles in 5 mM sodium phosphate buffer adjusted to pH 7.4 was found to be 16.7 ± 0.1 mV.

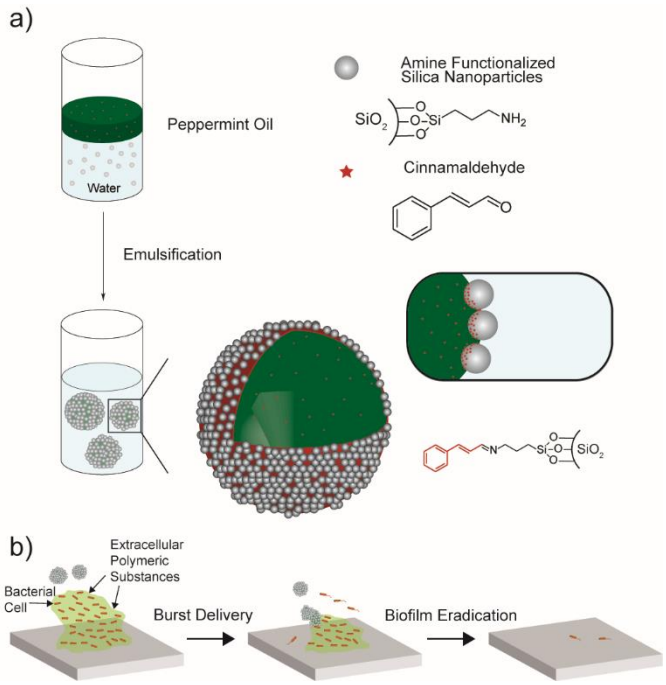

Figure 6.4: a) Schematic depiction of the strategy used to generate antimicrobial capsules. Peppermint oil with dissolved cinnamaldehyde is emulsified into an aqueous suspension of amine functionalized silica nanoparticles. Cinnamaldehyde within the oil reacts with the amines on the nanoparticles at the oil/water interface to create a multimodal delivery vehicle. b) Capsules interact with biofilm through electrostatic complementarity. Capsules release their payload disrupting the biofilm, eliminating the bacteria.

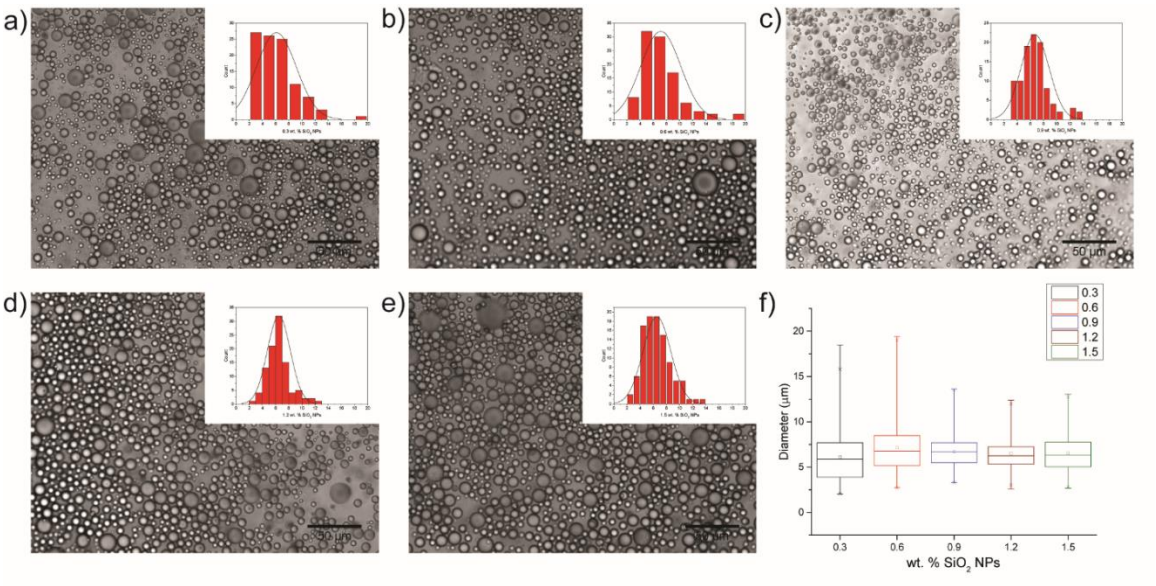

Figure 6.5: Optical microscopy images of P-Caps with increasing amounts of silica loading. P-Caps were generated using aqueous phases comprised of a) 0.3 wt. % silica (average diameter = 6.1 ± 3.0 µm), b) 0.6 wt. % silica (average diameter = 7.1 ± 3.0 µm), c) 0.9 wt. % silica (average diameter = 6.7 ± 2.1 µm), d) 1.2 wt. % silica (average diameter = 6.5 ± 1.7 µm), and e) 1.5 wt. % silica (average diameter = 6.6 ± 2.1 µm), respectively. Insets are histograms of the capsule diameter measurements. Scale bars are 50 µm. f) Box plot of the P-Caps at various silica loadings demonstrating capsule dispersity minimizes with increasing wt. % of silica.

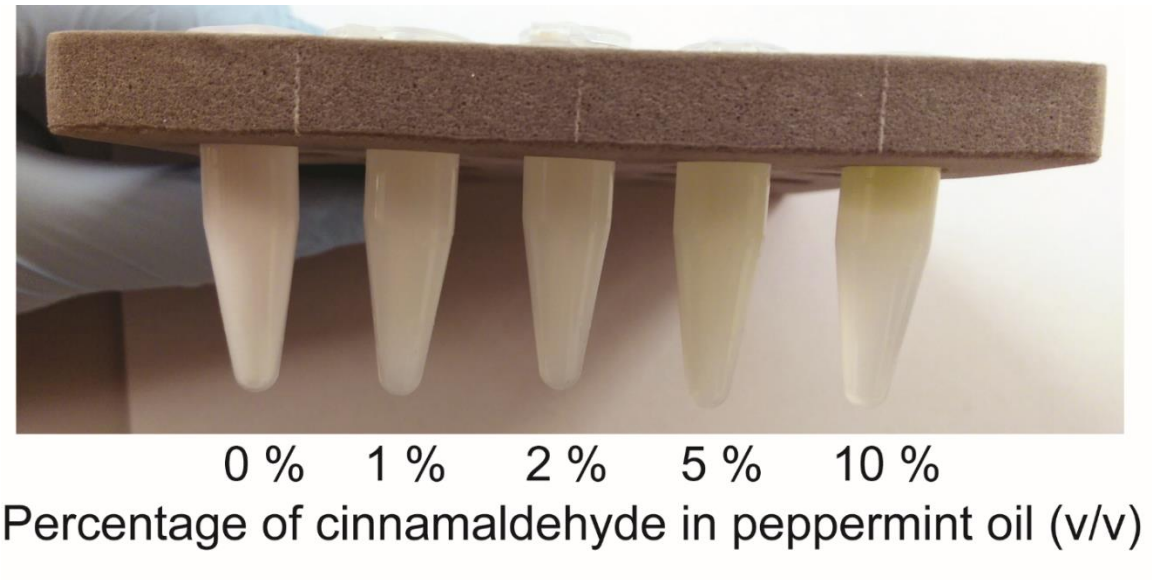

Figure 6.6: Capsules generated with increasing concentrations of cinnamaldehyde. Capsules were generated by adding 300 µL of peppermint oil or a cinnamaldehyde-peppermint oil mixture to 1.2 mL of MilliQ H_2O adjusted to a pH of 10 containing 1.2 wt. % of silica nanoparticles and emulsifying for 50 seconds.

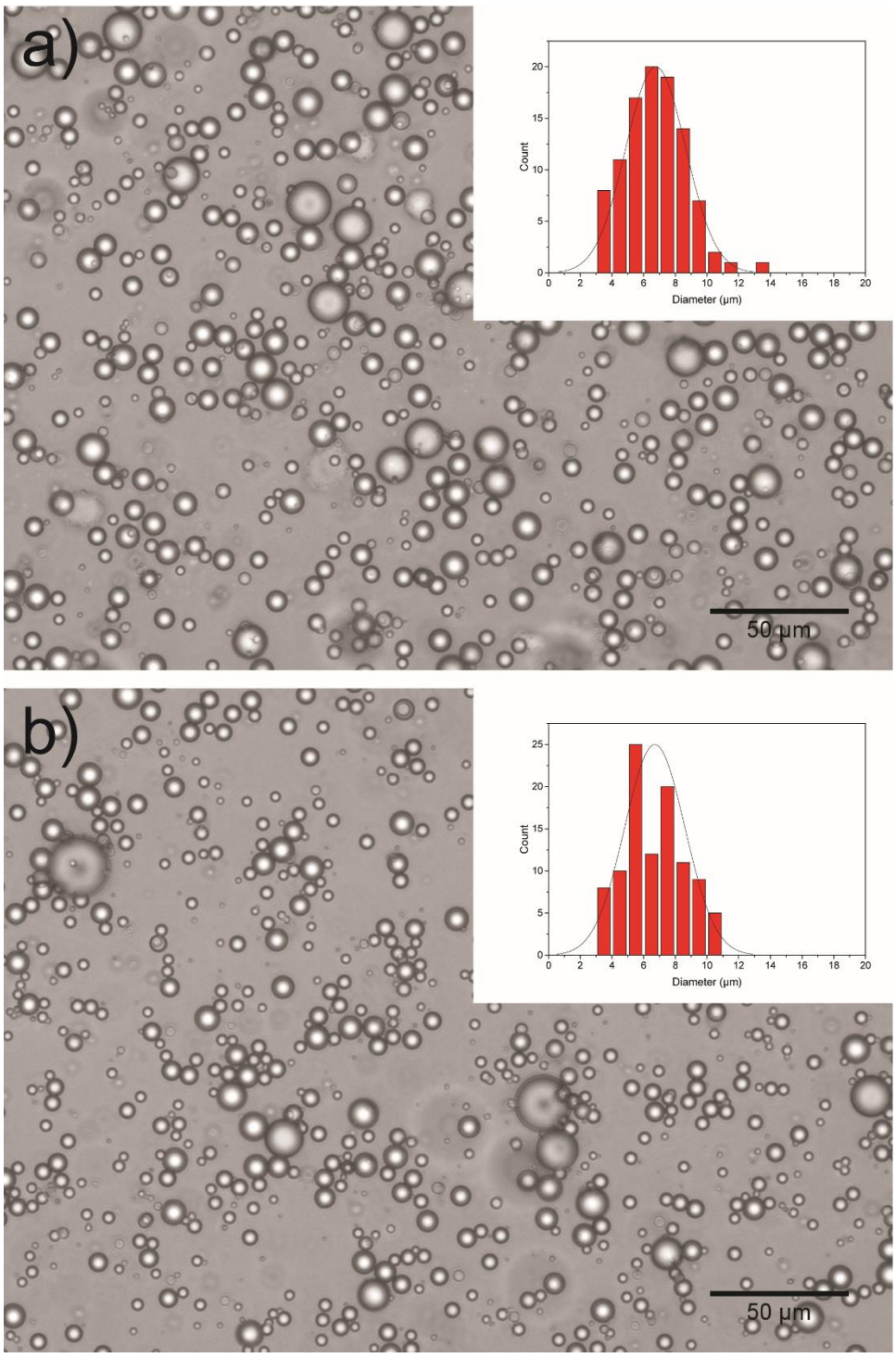

Figure 6.7: Optical microscopy images of a) P-Cap and b) CP-Cap. P-Cap had an average diameter of 6.8 ± 1.9 μm and CP-Cap had an average diameter of 6.7 ± 1.9 μm. Insets are histograms of the capsule diameter measurements. Scale bars are 50 μm.

We used confocal microscopy, X-ray photoelectron spectroscopy (XPS), attenuated total reflection Fourier transform infrared spectroscopy (ATR-FTIR), and contact angle goniometry to probe the cinnamaldehyde-nanoparticle interaction. Reactive molecules within the oil core of Pickering emulsions have been previously demonstrated to affect capsule morphologies by modulating the hydrophobicity of the nanoparticles.[38,39] To determine if structural reorganization occurs with our mixed oil system, capsules were generated using a Nile red loaded oil core and nanoparticles possessing cores labeled with fluorescein isothiocyanate (FITC). As shown in Figure 6.8a, b, and Figure 6.9, both capsules with and without cinnamaldehyde possess core-shell morphologies. This result indicates that the 5 % v/v loading of cinnamaldehyde into the peppermint oil does not alter the capsule structure.

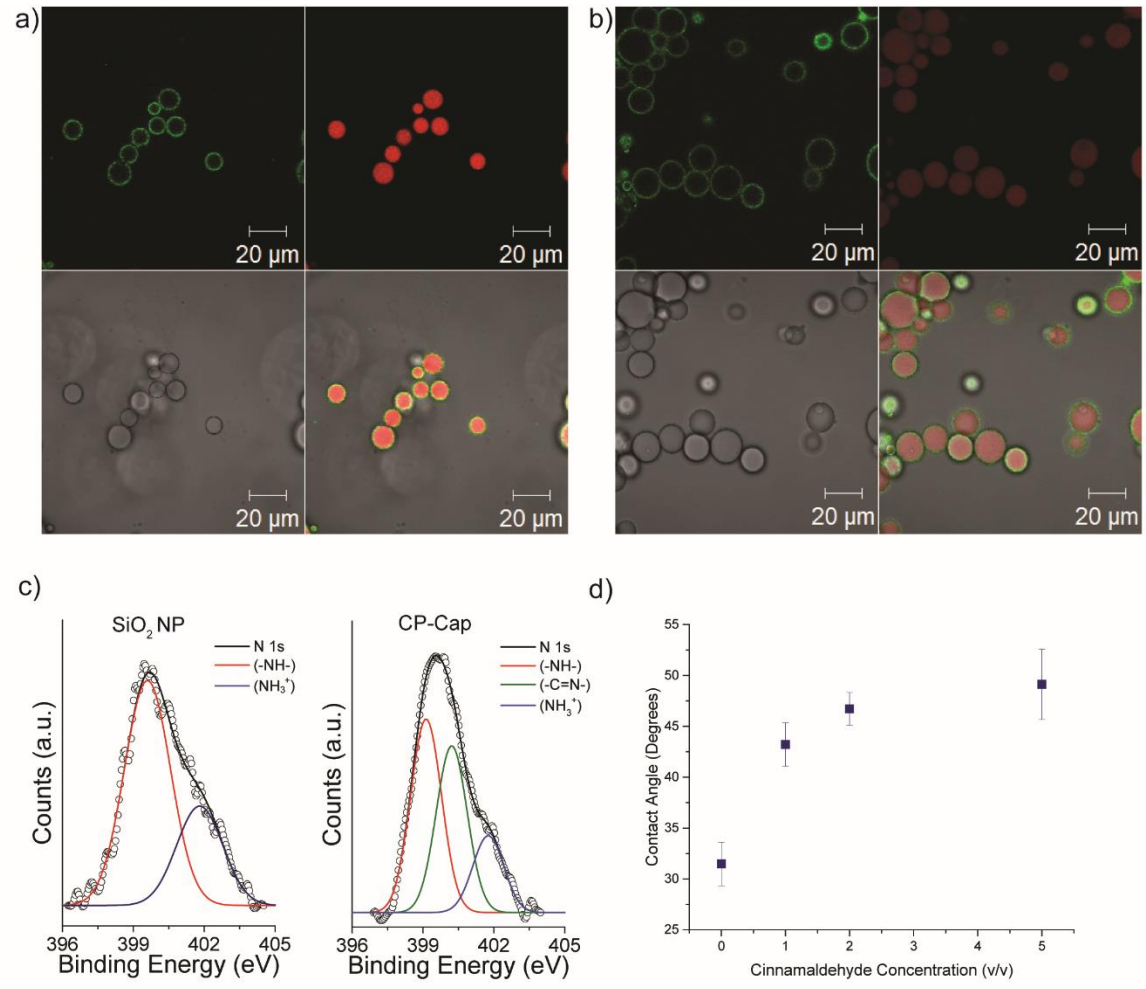

Figure 6.8: Confocal micrographs of a) P-Cap and b) CP-Cap. The nanoparticles' cores are labeled with fluorescein (green fluorescence) and the oil phases are loaded with Nile red (red fluorescence). Scale bars are 20 µm. c) XPS spectra showing N 1s core levels arising from SiO_2 NPs and CP-Cap. d) Water contact angles of silica nanoparticles following incubation with varying concentrations of cinnamaldehyde.

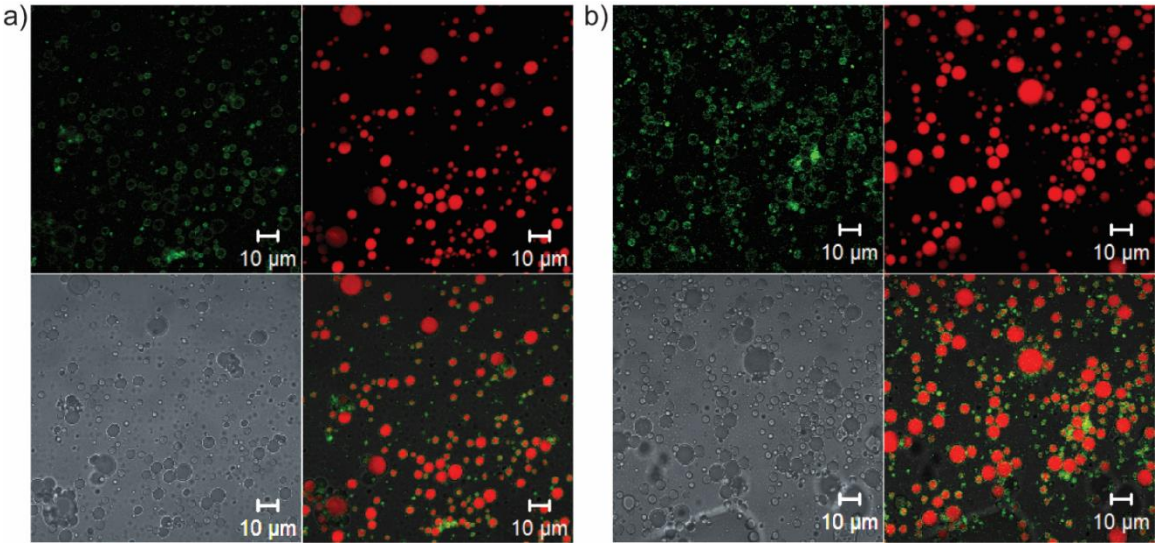

Figure 6.9: Confocal microscopy images of a) P-Cap and b) CP-Cap. The nanoparticles' cores are labeled with fluorescein (green fluorescence) and the oil phases are loaded with Nile red (red fluorescence). Scale bars are 10 µm.

We next used XPS and ATR-FTIR to elucidate the reactivity of the nanoparticles with the dissolved cinnamaldehyde of the capsules. Prior to analysis, CP-Caps were disrupted with ethanol, centrifuged, and lyophilized to remove any adsorbed cinnamaldehyde. The Schiff base of 3-aminopropyltriethoxysilane and cinnamaldehyde was also synthesized for comparison. (Figure 6.10) As shown in Figure 6.8c, the SiO_2 NPs showed two chemically distinct species with a lower binding energy (BE) component at ca. 399.5 eV and a higher BE component at ca. 401.8 eV. These correspond to amine (-NH-) and protonated amine (NH_3^+) present on the surface of SiO_2 NPs that is consistent with previously reported values.[40] The N 1s spectra of CP-Cap shows three distinct chemical species. In addition to the two N 1s BE components observed in the SiO_2 NPs, a new peak centered at ca. 400.1 eV indicates the formation of an imine functional (-C=N-) group which corroborates well with literature values.[41] The N 1s spectra from the synthesized Schiff base showed a single chemically distinct N 1s

species centered at ca. 400.2 eV, which corresponds to the imine functional group (-C=N-).[41] Similarly, the chemically distinct species of the C 1s spectra obtained from CP-Cap matches well with the synthesized Schiff base further providing evidence on the covalent linkage of the amine and cinnamaldehyde (Figure 6.11). Additionally, the Si 2p and O 1s peak shows typical BEs centered at ca. 103.2 eV and 532.6 eV, respectively that matches with reported values for SiO_2 NPs (Figure 6.11).[42] ATR-FTIR analysis further supported the formation of the cinnamaldehyde Schiff base (Figure 6.12).

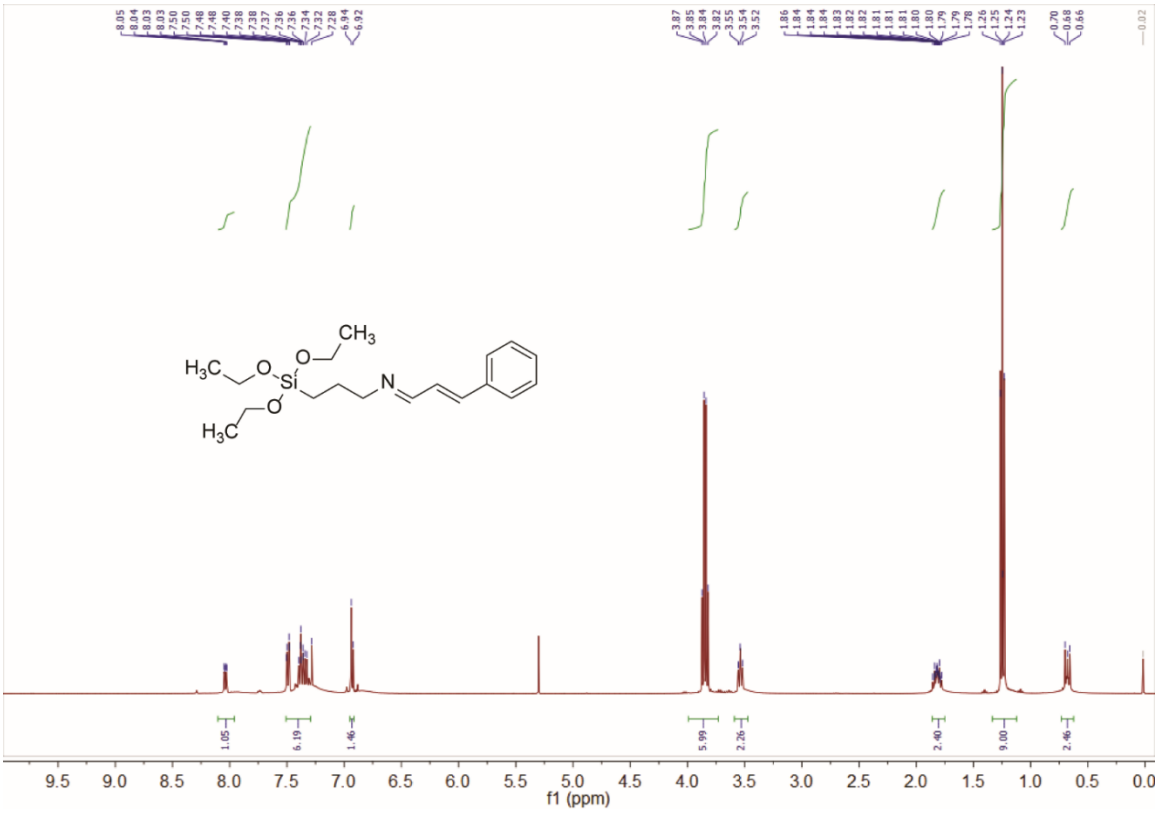

Figure 6.10: 400 MHz 1H NMR spectrum of the Schiff base, 3-phenyl-N-(3-triethoxysilylpropyl)prop-2-en-1-imine, in chloroform-D (D-99.8 %). Spectrum was obtained on a Bruker Avance 400 MHz, 16 scans.

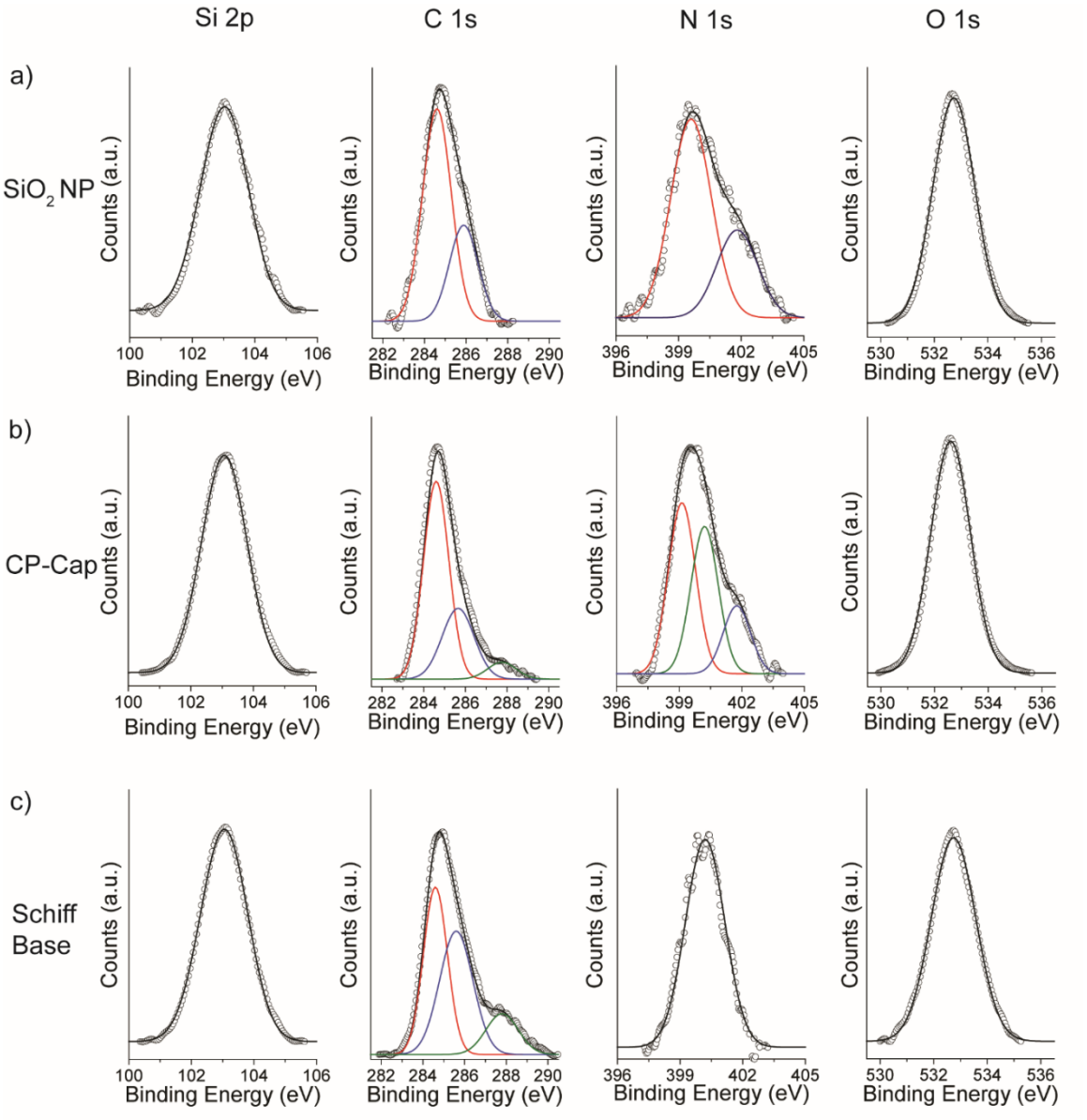

Figure 6.11: XPS spectra of a) amine functionalized SiO2 NPs, b) CP-Caps, and c) Schiff base.

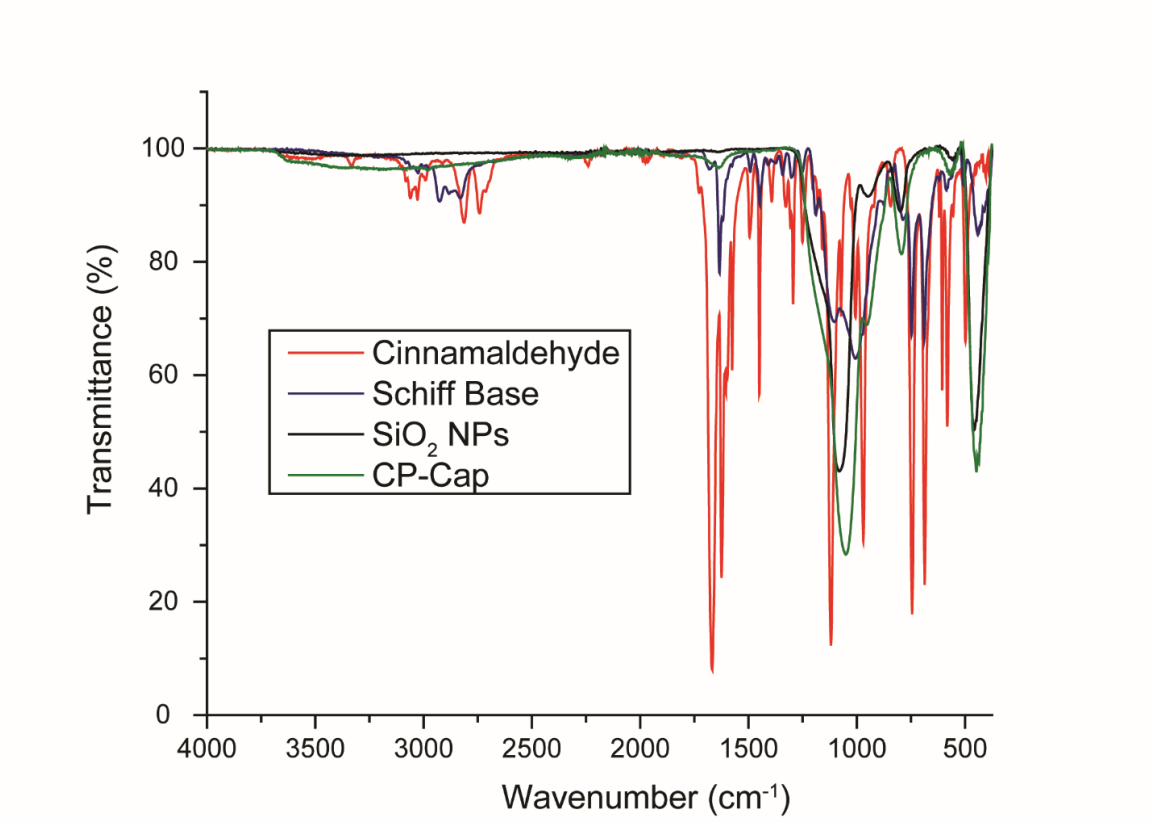

Figure 6.12: ATR-FT-IR characterization of cinnamaldehyde, the cinnamaldehyde-silane Schiff base, the silica nanoparticles, and CP-Caps after freeze drying. Cinnamaldehyde displayed characteristic peaks at 1667 cm^{-1} and 1624 cm^{-1} attributed to the C=O and C=C frequencies. The Schiff base possessed peaks at 1681 cm^{-1} and 1633 cm^{-1} attributed to C=N and C=C bonds, respectively. The Schiff base also displayed peaks at 1102 cm^{-1} and 1006 cm^{-1} attributed to the Si-O and Si-OEt frequencies. Amine-functionalized silica nanoparticles showed characteristic peaks at 1080 cm^{-1} and 947 cm^{-1} attributed to the Si-O and Si-OH frequencies. CP-Caps displayed peaks at frequencies similar to the SiO_2 NPs and the Schiff base confirming the formation of the Schiff base complex on the nanoparticles.

An *in situ* covalent reaction of the primary amine groups on the nanoparticles with cinnamaldehyde should alter the hydrophobicity of the nanoparticle surface improving the stabilization behavior of the Pickering emulsifiers.[43] Contact angle goniometry was used to measure the change in nanoparticle hydrophobicity. Nanoparticles were deposited onto silicon wafers and briefly incubated in

dichloromethane solutions with varying amounts of dissolved cinnamaldehyde. The surfaces were then rinsed with dichloromethane, dried, and the water contact angles were obtained. (Figure 6.13) Figure 6.8d shows that as the percentage of cinnamaldehyde by volume increases from 0 % to 5 %, the water contact angle of the nanoparticles increases from 31° to 49°. This increase in water contact angle, taken together with the XPS data, the ATR-FTIR data, and confocal images, indicates that the inclusion of cinnamaldehyde within the peppermint oil core generates a distinct, multi-component capsule structure.

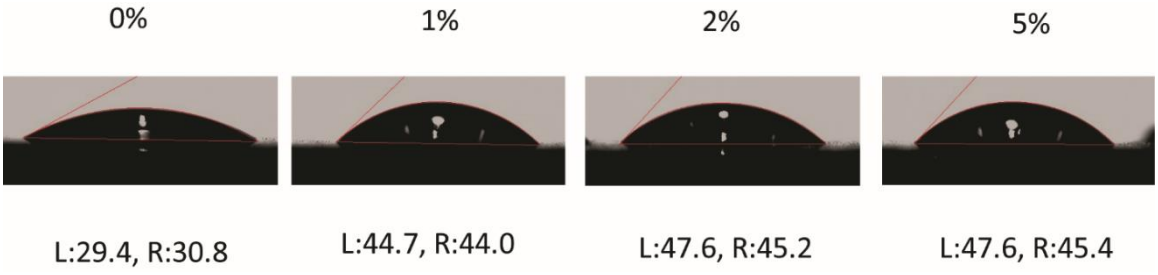

Figure 6.13: Representative digital images of water droplets used to determine contact angles.

6.2.2. Capsule penetration into the biofilms

Biofilms produce extracellular polymeric substances that prevent effective delivery of therapeutics.[44] Having established that the capsules have core-shell morphologies and the cinnamaldehyde is successfully incorporated into the capsules, we set out to determine whether these capsules could effectively penetrate into biofilms. Using fluorescently labeled nanoparticles to track the delivery of the emulsions, we treated biofilms from *E. coli* that had been modified to express E2-Crimson, a far-red fluorescent protein. As shown in Figure 6.14, both P-Cap and CP-Cap diffuse into the biofilm matrix and efficiently disperse throughout the biofilm whereas the unassembled

nanoparticles displayed minimal penetration. These data indicate the capsules deliver their payload in a burst release fashion and that both the oil core and nanoparticle shell are operative for effective delivery.

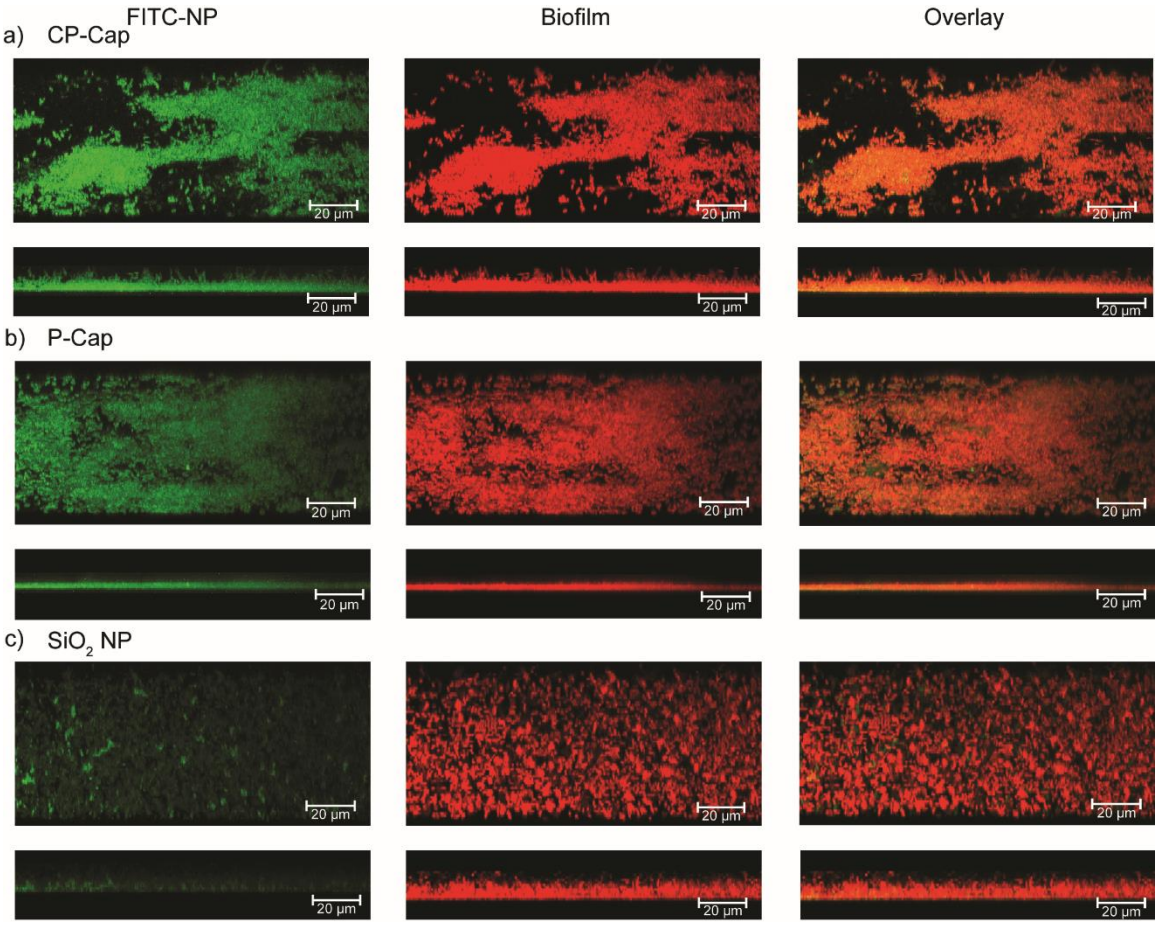

Figure 6.14: Representative 3D projection of confocal image stacks of 1 day-old *E. coli* DH5α biofilm after 3 hrs treatment with a) CP-Cap containing FITC-labeled SiO2 NP, b) P-Cap containing FITC-labeled SiO2 NP, and c) FITC-labeled SiO2 NP at 20 % (v/v % of 2 % emulsion) concentration. Upper panels are projection at 247° angle turning along Y axis and lower panels are at 270° angle turning along Y axis. Scale bars are 20 µm.

6.2.3. Antimicrobial activity of capsules against biofilms

Next, we investigated the therapeutic behavior of the capsules against established bacterial biofilms. One laboratory strain, *E. coli* DH5α, and 3 pathogenic bacteria strains of clinical isolates, *P. aeruginosa* (CD-1006), *S. aureus* (CD-489, a methicillin-resistant

strain), and *E. cloacae complex* (CD-1412), were chosen to test our system. As shown in Figure 6.15, both the CP-Cap and P-Cap vehicles effectively were able to kill bacteria cells in all four biofilms, with CP-Cap possessing greater activity. The capsules demonstrated a dramatically enhanced efficacy compared with the unencapsulated oil, supporting the hypothesis that the cationic nanoparticle shell of the capsules increases interaction with the biofilms.[45] In addition, the acidic pH of the biofilm environment[46] should promote the hydrolysis of Schiff bases, enhancing the sustained release of cinnamaldehyde. These capsules were able to treat both Gram negative (*E. coli*, *P. aeruginosa*, and *E. cloacae* complex) and Gram positive (*S. aureus*) bacteria. Notably, the capsules demonstrated a similar efficacy against the multi-drug resistant *S. aureus* stain when compared to the non-resistant strains, supporting that these capsules present a viable treatment alternative to traditional antibiotics.

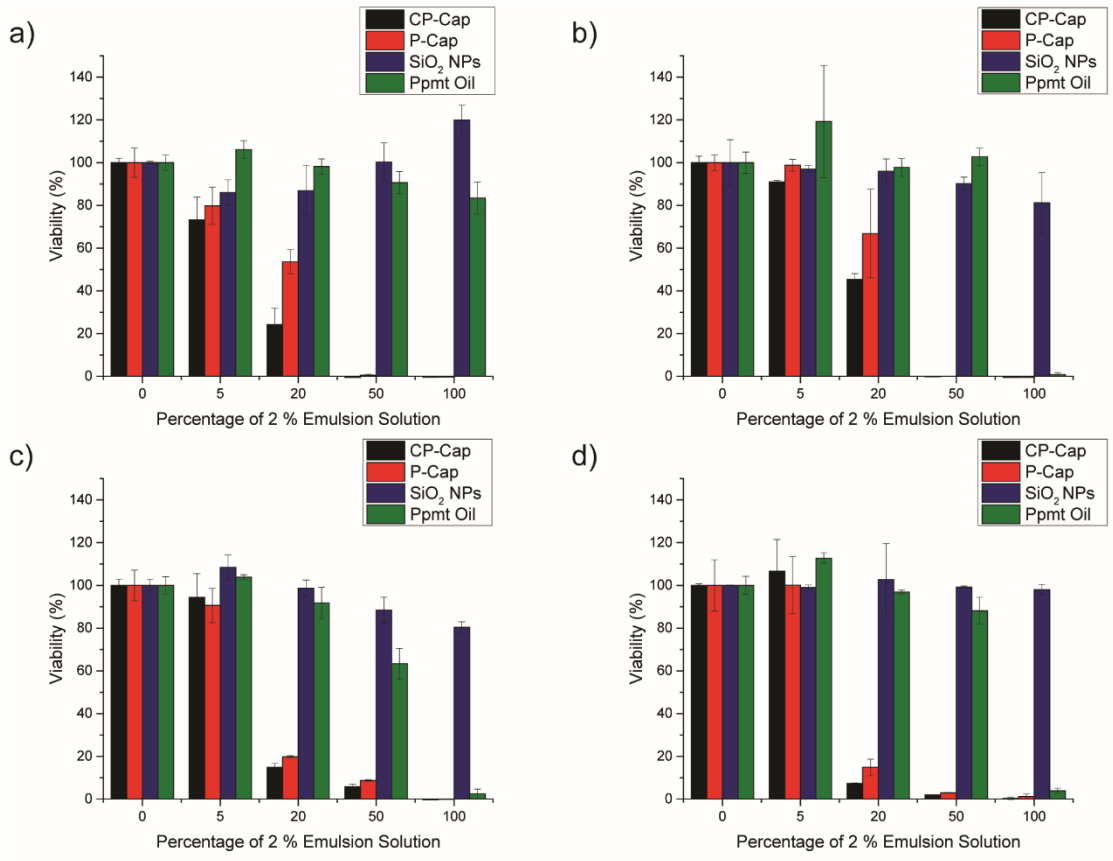

Figure 6.15: Viability of 1 day-old a) P. aeruginosa (CD-1006) b) E. coli DH5α c) S. aureus (CD-489) d) E. cloacae complex (CD-1412) biofilms after 3 hrs treatment with CP-Cap, P-Cap, SiO2 NP, and peppermint oil at different emulsion concentrations (v/v % of 2 % emulsion). The data are average of triplicates and the error bars indicate the standard deviations.

6.2.4. Co-culture treatment of biofilms

Biofilm infections within wounds interfere with the ability of the host to regenerate damaged tissue.[47] Fibroblasts in particular play a vital role in the wound healing process, helping to close the injury and redevelop the extracellular matrix within the skin.[48,49] We used an *in vitro* co-culture model comprised of mammalian fibroblasts and a biofilm to determine whether our capsules could successfully treat a biofilm in the presence of host cells. [50] *E. coli* DH5α bacteria were seeded with a confluent NIH 3T3 fibroblast cell monolayer overnight to generate biofilms prior to treatment. The co-

cultures were treated with capsules for 3 hrs, washed, and the viabilities of both fibroblasts and bacteria were measured. As shown in Figure 6.16, CP-Cap effectively treated the biofilm infection whereas P-Cap and the controls did not. The capsule structure also prevented the toxic effects shown by the unencapsulated peppermint oil to the fibroblasts. Notably, CP-Cap enhanced 3T3 cell growth in agreement with studies that cinnamaldehyde can promote insulin-like growth factor-I signaling, increasing cell proliferation.[32]

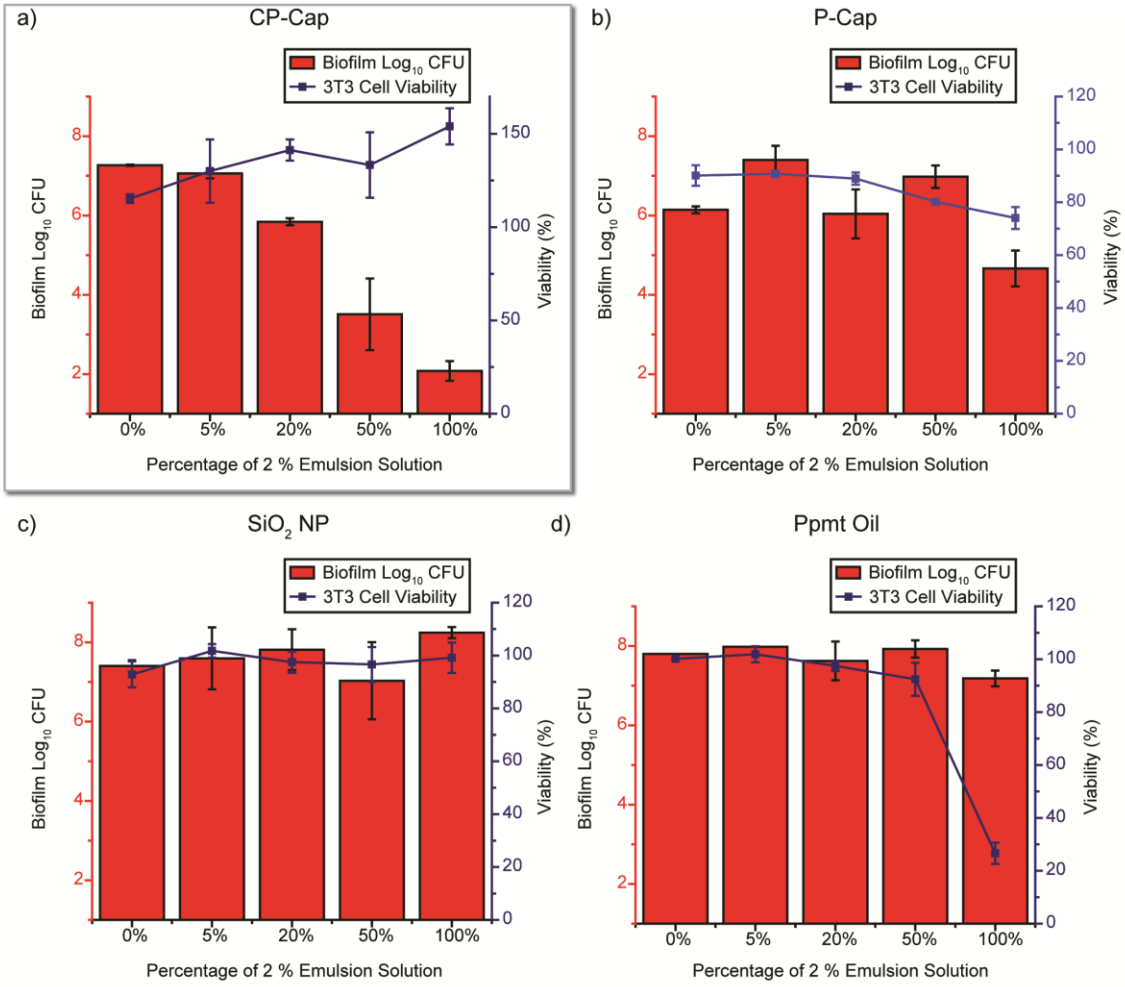

Figure 6.16: Viability of 3T3 fibroblast cells and E. coli biofilms in the co-culture model after 3 hrs treatment with a) CP-Cap, b) P-Cap, c) SiO2 NP, and d) peppermint oil at different emulsion concentrations (v/v % of 2 % emulsion). Scatters and lines represent

3T3 fibroblast cell viability. Bars represent $\log_{10}$ of colony forming units in biofilms. The data are average of triplicates and the error bars indicate the standard deviations.

6.3. Conclusions

In summary, we report the development of a multimodal antimicrobial delivery vehicle. The nanoparticle stabilized capsules demonstrated highly effective therapeutic behavior, successfully eradicating pathogenic biofilm strains of clinical isolates. Furthermore, the capsules effectively eliminated a biofilm infection while promoting fibroblast viability in an *in vitro* co-culture model. Future studies will probe capsule performance in combating *in vivo* biofilms. These capsules have potential applications as a general surface disinfectant as well as an antiseptic for wound treatment. The reactive self-assembly based strategy provides a promising platform to create effective delivery vehicles to combat bacterial biofilms.

6.4. Experimental Methods

6.4.1. Materials

All reagents/materials were purchased from Fisher Scientific and used as received. Boron-doped Si wafers were purchased from WRS Materials. NIH-3T3 cells (ATCC CRL-1658) were purchased from ATCC. Dulbecco's Modified Eagle's Medium (DMEM) (DMEM; ATCC 30-2002) and fetal bovine serum (Fisher Scientific, SH3007103) were used in cell culture. Pierce LDH Cytotoxicity Assay Kit was purchased from Fisher Scientific.

6.4.2. Synthesis of Silica Nanoparticles

Silica nanoparticles were synthesized according to the reported procedure.[33,38] Briefly, to synthesize 150 nm amine functionalized silica nanoparticles, 24 mL of ammonium hydroxide were added to 300 mL of absolute ethanol and stirred for five minutes in a 500

mL round-bottom flask. Then 12 mL of tetraethyl orthosilicate were added to the reaction flask and stirred overnight at room temperature. To functionalize the surface of the nanoparticles, 1.22 mL of 3-aminopropyl triethoxysilane were added and the reaction was stirred for an additional 24 hours. The nanoparticles were purified by centrifuging and re-dispersing in water and ethanol (3x each).

Synthesis of fluorescein labeled nanoparticles[51] was performed following a similar method wherein 5.25 mg of fluorescein isothiocyanate were reacted with 69.0 mg of 3-aminopropyl triethoxysilane in one mL of absolute ethanol under nitrogen overnight. This fluorescent conjugate mixture was added to the nanoparticle reaction solution 5 minutes after the addition of tetraethyl orthosilicate. The procedure then proceeded as described above.

6.4.3. Transmission Electron Microscopy (TEM)

TEM samples were prepared on 300 square mesh nickel grids with Formvar film purchased from Electron Microscopy Sciences. TEM images were acquired on a JEOL 100CX operating at 100 keV.

6.4.4. Dynamic Light Scattering (DLS)

DLS experiments and zeta potential measurements were performed using a Malvern Zetasizer Nano ZS. Samples were sonicated prior to measurements.

6.4.5. Preparation of Capsules

Stock capsules solutions were prepared in 1.5 mL Eppendorf tubes. To prepare the stock P-Cap emulsions, 300 µL of peppermint oil was added to 1.2 mL of a 1.2 % wt. solution of SiO_2 NPs in MilliQ H_2O adjusted to pH 10 and was emulsified in an amalgamator for 50 seconds. To prepare the stock CP-Cap emulsions, 15 µL of cinnamaldehyde was

dissolved in 285 µL of peppermint oil prior to emulsification as described. The emulsions were allowed to rest overnight prior to use. Optical images of the capsules were taken on an Olympus IX51 microscope.

6.4.6. Synthesis of Schiff Base

Cinnamaldehyde (3.8 mL, 30 mmol) was dissolved in 150 mL of toluene and 3-aminopropyl triethoxysilane (7.0 mL, 30 mmol) was added to the stirring reaction. The flask was then equipped with a Dean-Stark trap, heated to 110 °C, and stirred overnight. After the reaction was complete (monitored by water volume collected in Dean-Stark trap), the mixture was cooled to room temperature and the solvent removed under reduced pressure. The crude product was dissolved in dichloromethane and filtered to remove brown precipitates. The filtrate was dried over anhydrous sodium sulfate and the dichloromethane was removed under reduced pressure. The product was obtained as an amber colored oil, yield = 8.78 g, 87 %.

6.4.7. XPS Determination of Cinnamaldehyde Reaction

To determine whether cinnamaldehyde reacted with the surface amines of the nanoparticle, 500 µL of CP-Cap with 5 % v/v of cinnamaldehyde were diluted into 1.0 ml of ethanol. Capsules were then broken by sonicating for 5 minutes and centrifuging at 14,000 rpm to release all unreacted cinnamaldehyde. Capsule were redispersed in ethanol, sonicated, and centrifuged three times to completely remove the oil phase. The CP-Cap pellet was then freeze dried in order to obtain a dry solid for analysis.

Samples were prepared by drop-casting the sample on a 100 nm gold-coated silicon substrate. XPS measurements were carried out using Physical Electronics Quantum 2000 spectrometer at a pressure below 1×10^{-9} Torr. The survey scan, C 1s, N 1s, O 1s and Si

2p core level spectra for all samples were recorded with un-monochromatized Al Kα radiation (photon energy of 1486.6 eV) at a pass energy of 46.95 eV and electron takeoff angle of 15°. The overall resolution was 0.2 eV for the XPS measurements. Chemically distinct species were resolved using a Gaussian-Lorentzian function with non-linear least-square fitting procedure. All XPS spectra were background corrected using the Shirley algorithm and aligning the elemental binding energies to the adventitious carbon (C1s) binding energy of 284.6 eV.[42]

6.4.8. ATR-FT-IR Determination of Cinnamaldehyde Reaction

IR was performed on a Bruker Alpha FT-IR spectrophotometer fitted with a Platinum ATR QuickSnap sampling module. Cinnamaldehyde was analyzed as a pure liquid. The silica nanoparticles and Schiff base were analyzed as neat solids. The CP-Caps were dissolved in ethanol, sonicated, and centrifuged three times to remove the oil phase. The CP-Cap pellet was then freeze dried in order to obtain a dry solid that was analyzed.

6.4.9. Contact Angle Goniometry

Samples were prepared by immersing a clean silicon wafer (1 cm x 1 cm) into 1 mL of a 1.2 % wt. solution of SiO_2 NPs in MilliQ H_2O adjusted to pH 10 for 5 minutes. Wafers were then washed with MilliQ H_2O to removed excess nanoparticles and dried under a N_2 stream. Samples were then incubated in 1 mL solutions of dichloromethane with varying amounts (0, 1, 2, 5 % v/v) of dissolved cinnamaldehyde for 5 minutes. Wafers were then washed with dichloromethane and dried under a N_2 stream. Static water contact angles were measured using a VCA Optima surface analysis/goniometry system with water droplets size of 2 µL.

6.4.10. Biofilm Formation

Biofilms were grown as previously reported.[50] Bacteria were inoculated in lysogeny broth (LB) medium at 37 °C until stationary phase. The cultures were then harvested by centrifugation and washed with 0.85 % sodium chloride solution three times. Concentrations of resuspended bacterial solution were determined by optical density measured at 600 nm. LB medium was supplemented with 0.1 % glucose, 1 mM $MgSO_4$, 0.15 M ammonium sulfate, and 34 mM citrate and buffered to pH 7 to ensure bacterial adherence to the microplate. Seeding solutions were then made in this modified LB medium to reach an OD_{600} of 0.1. A 100 μL amount of the seeding solutions was added to each well of the 96 well microplate. The plates were covered and incubated at room temperature under static conditions for 1 day.

A 2 % v/v emulsion stock solution made by diluting the generated capsules into LB medium. The stock solution was then diluted to the desired level and incubated with the biofilms for 3 hrs. Biofilms were washed with phosphate buffer saline (PBS) three times and viability was determined using an Alamar Blue assay.[52] Modified LB medium without bacteria was used as a negative control.

6.4.11. Biofilm-3T3 Fibroblast Cell Co-culture

Co-culture was performed as previously described.[50] Briefly, a total of 20,000 NIH 3T3 (ATCC CRL-1658) cells were cultured in Dulbecco's modified Eagle medium (DMEM; ATCC 30-2002) with 10 % bovine calf serum and 1% antibiotics at 37 °C in a humidified atmosphere of 5 % CO_2. Cells were kept for 24 h to reach a confluent monolayer. Bacteria were inoculated and harvested as described above, and seeding solutions were made in buffered DMEM supplemented with glucose to reach an OD_{600} of 0.1. Old medium was removed from 3T3 cells followed by addition of 100 μL of seeding solution.

The co-cultures were then stored in a box with damp paper towels at 37 °C overnight without shaking.

Testing solutions at different concentrations were made by diluting capsules into DMEM prior to use. Media was removed from co-culture, replaced with testing solutions, and incubated for 3 hrs at 37 °C. Co-cultures were then analyzed using a LDH cytotoxicity assay to determine mammalian cell viability according the manufacturer's instructions.[53] To determine bacteria viability in biofilms, the testing solutions were removed and co-cultures were washed with PBS. Fresh PBS was then added to disperse remaining bacteria from biofilms in co-culture by sonication for 20 minutes and mixing with pipette. The solutions containing dispersed bacteria were then plated onto agar plates and colony forming units were counted after incubation at 37 °C overnight.

6.4.12. Calculation of Cinnamaldehyde to Amine Ratio

Diameter of SiO_2 NP = 152 nm

Total number of NPs in solution:

$$N_{NP} = \frac{Mass\ of\ NPs\ in\ solution\ /\ Density\ of\ silica\ NPs}{Volume\ of\ individual\ NP}$$

$$N_{NP} = \frac{(0.0144\ g)\ /\ \left(1.96\ \frac{g}{cm^{-3}}\right)}{1.84\times10^{-15}\ cm^{-3}}$$

$$N_{NP} = 4.00 \times 10^{12}$$

Moles of amine in solution:

$$Moles\ of\ NH_2 = \frac{N_{NP}\times Surface\ area\ of\ individual\ NP\times \#\ of\ amine\ groups\ per\ nm^2}{6.02\times10^{23}\ \frac{amine\ molecules}{mol}}$$

$$Moles\ of\ NH_2 = \frac{(4.00\times10^{12})\times(72600\ nm^2)\times\left(4.0\frac{amine\ molecules}{nm^2}\right)}{\left(6.02\times10^{23}\ \frac{amine\ molecules}{mol}\right)}$$

$$Moles\ of\ NH_2 = 1.9 \times 10^{-6}\ moles$$

Moles of cinnamaldehyde (CA) in solution:

$$Moles\ of\ CA = \frac{Volume\ of\ cinnamaldehyde\ in\ solution \times Density\ of\ cinnamaldehyde}{Molar\ mass\ of\ cinnamaldehyde}$$

$$Moles\ of\ CA = \frac{(0.0150\ mL) \times \left(1.05\ \frac{g}{mL}\right)}{132.16\ \frac{g}{mol}}$$

$$Moles\ of\ CA = 1.20 \times 10^{-4}\ moles$$

Ratio of CA to NH_2:

62

6.5. References

(1) Costerton, J. W.; Stewart, P. S.; Greenburg, E. P. *Science* **1999**, *284*, 1318.

(2) Lindsay, D.; von Holy, A. *J. Hosp. Infect.* **2006**, *64*, 313.

(3) Costerton, J. W.; Montanaro, L.; Arciola, C. R. *Int. J. Artif. Organs* **2005**, *28*, 1062.

(4) Busscher, H. J.; Rinastiti, M.; Siswomihardjo, W.; van der Mei, H. C. *J. Dent. Res.* **2010**, *89*, 657.

(5) Costerton, W.; Veeh, R.; Shirtliff, M.; Pasmore, M.; Post, C.; Ehrlich, G. *J. Clin. Invest.* **2003**, *112*, 1466.

(6) Ehrlich, G. D.; Veeh, R.; Wang, X.; Costerton, J. W.; Hayes, J. D.; Hu, F. Z.; Daigle, B. J.; Ehrlich, M. D.; Post, J. C. *JAMA* **2002**, *287*, 1710.

(7) James, G. A; Swogger, E.; Wolcott, R.; Pulcini, E. deLancey; Secor, P.; Sestrich, J.; Costerton, J. W.; Stewart, P. S. *Wound Repair Regen.* **2008**, *16*, 37.

(8) Stewart, P. S.; William Costerton, J. *Lancet* **2001**, *358*, 135.

(9) Szomolay, B.; Klapper, I.; Dockery, J.; Stewart, P. S. *Environ. Microbiol.* **2005**, *7*, 1186.

(10) Marion-Ferey, K.; Pasmore, M.; Stoodley, P.; Wilson, S.; Husson, G. P.; Costerton, J. W. *J. Hosp. Infect.* **2003**, *53*, 64.

(11) Lynch, A. S.; Robertson, G. T. *Annu. Rev. Med.* **2008**, *59*, 415.

(12) Levy, S. B.; Marshall, B. *Nat. Med.* **2004**, *10*, S122.

(13) Kalemba, D.; Kunicka, A. *Curr. Med. Chem.* **2003**, *10*, 813.

(14) Hemaiswarya, S.; Kruthiventi, A. K.; Doble, M. *Phytomedicine* **2008**, *15*, 639.

(15) Burt, S. *Int. J. Food Microbiol.* **2004**, *94*, 223.

(16) Kavanaugh, N. L.; Ribbeck, K. *Appl. Environ. Microbiol.* **2012**, *78*, 4057.

(17) Nostro, A.; Roccaro, A. S.; Bisignano, G.; Marino, A.; Cannatelli, M. A; Pizzimenti, F. C.; Cioni, P. L.; Procopio, F.; Blanco, A. R. *J. Med. Microbiol.* **2007**, *56*, 519.

(18) Chen, H.; Davidson, P. M.; Zhong, Q. *Appl. Environ. Microbiol.* **2014**, *80*, 907.

(19) Carpenter, A. W.; Worley, B. V; Slomberg, D. L.; Schoenfisch, M. H. *Biomacromolecules* **2012**, *13*, 3334.

(20) Zhu, X.; Radovic-Moreno, A. F.; Wu, J.; Langer, R.; Shi, J. *Nano Today* **2014**, *9*, 478.

(21) Radovic-Moreno, A. F.; Lu, T. K.; Puscasu, V. a; Yoon, C. J.; Langer, R.; Farokhzad, O. C. *ACS Nano* **2012**, *6*, 4279.

(22) Goswami, S.; Thiyagarajan, D.; Das, G.; Ramesh, A. *ACS Appl. Mater. Interfaces* **2014**, *6*, 16384.

(23) Chang, Y.; McLandsborough, L.; McClements, D. J. *J. Agric. Food Chem.* **2013**, *61*, 8906.

(24) Liang, R.; Xu, S.; Shoemaker, C. F.; Li, Y.; Zhong, F.; Huang, Q. *J. Agric. Food Chem.* **2012**, *60*, 7548.

(25) Gomes, C.; Moreira, R. G.; Castell-Perez, E. *J. Food Sci.* **2011**, *76*, N16.

(26) Shalel, S.; Streichman, S.; Marmur, A. *J. Colloid Interface Sci.* **2002**, *252*, 66.

(27) Wilhelm, K.-P.; Freitag, G.; Wolff, H. H. *J. Am. Acad. Dermatol.* **1994**, *30*, 944.

(28) Ramsden, W. *Proc. R. Soc. London* **1903**, *72*, 156.

(29) Pickering, S. U. *J. Chem. Soc. Trans.* **1907**, *91*, 2001.

(30) Binks, B. P. *Curr. Opin. Colloid Interface Sci.* **2002**, *7*, 21.

(31) Ghouchi Eskandar, N.; Simovic, S.; Prestidge, C. A. *Pharm. Res.* **2009**, *26*, 1764.

(32) Takasao, N.; Tsuji-Naito, K.; Ishikura, S.; Tamura, A.; Akagawa, M. *J. Agric. Food Chem.* **2012**, *60*, 1193.

(33) Stöber, W.; Fink, A.; Bohn, E. *J. Colloid Interface Sci.* **1968**, *26*, 62..

(34) Rosen, J. E.; Gu, F. X. *Langmuir* **2011**, *27*, 10507.

(35) Rancan, F.; Gao, Q.; Graf, C.; Troppens, S.; Hadam, S.; Hackbarth, S.; Kembuan, C.; Blume-Peytavi, U.; Rühl, E.; Lademann, J.; Vogt, A. *ACS Nano* **2012**, *6*, 6829.

(36) Schladt, T. D.; Schneider, K.; Schild, H.; Tremel, W. *Dalton Trans.* **2011**, *40*, 6315.

(37) Nabeshi, H.; Yoshikawa, T.; Matsuyama, K.; Nakazato, Y.; Matsuo, K.; Arimori, A.; Isobe, M.; Tochigi, S.; Kondoh, S.; Hirai, T.; Akase, T.; Yamashita, T.; Yamashita, K.; Yoshida, T.; Nagano, K.; Abe, Y.; Yoshioka, Y.; Kamada, H.; Imazawa, T.; Itoh, N.; Nakagawa, S.; Mayumi, T.; Tsunoda, S.; Tsutsumi, Y. *Biomaterials* **2011**, *32*, 2713.

(38) Duncan, B.; Landis, R. F.; Jerri, H. a; Normand, V.; Benczédi, D.; Ouali, L.; Rotello, V. M. *Small* **2015**, *11*, 1302.

(39) Williams, M.; Warren, N. J.; Fielding, L. A.; Armes, S. P.; Verstraete, P.; Smets, J. *ACS Appl. Mater. Interfaces* **2014**, *6*, 20919.

(40) Tan, K. L.; Tan, B. T. G.; Kang, E. T.; Neoh, K. G. *Phys. Rev. B* **1989**, *39*, 8070.

(41) Ricci, M.; Trinquecoste, M.; Auguste, F.; Canet, R.; Delhaes, P.; Guimon, C.; Pfister-Guillouzo, G.; Nysten, B.; Issi, J. P. *J. Mater. Res.* **1993**, *8*, 480.

(42) Ramanathan, R.; Campbell, J. L.; Soni, S. K.; Bhargava, S. K.; Bansal, V. *PLoS One* **2011**, *6*, e17707.

(43) Pieranski, P. *Phys. Rev. Lett.* **1980**, *45*, 569.

(44) Hurdle, J. G.; O'Neill, A. J.; Chopra, I.; Lee, R. E. *Nat. Rev. Microbiol.* **2011**, *9*, 62.

(45) Li, X.; Yeh, Y.; Giri, K.; Mout, R.; Landis, R. F.; Prakash, Y. S.; Rotello, V. M. *Chem. Commun.* **2015**, *51*, 282.

(46) Harrison, J. J.; Ceri, H.; Turner, R. J. *Nat. Rev. Microbiol.* **2007**, *5*, 928.

(47) Roy, S.; Elgharably, H.; Sinha, M.; Ganesh, K.; Chaney, S.; Mann, E.; Miller, C.; Khanna, S.; Bergdall, V. K.; Powell, H. M.; Cook, C. H.; Gordillo, G. M.; Wozniak, D. J.; Sen, C. K. *J. Pathol.* **2014**, *233*, 331.

(48) Watt, F. M. *Science* **2014**, *346*, 937.

(49) Sun, B. K.; Siprashvili, Z.; Khavari, P. a. *Science* **2014**, *346*, 941.

(50) Li, X.; Kong, H.; Mout, R.; Saha, K.; Moyano, D. F.; Robinson, S. M.; Rana, S.; Zhang, X.; Riley, M. A.; Rotello, V. M. *ACS Nano* **2014**.

(51) Santra, S.; Liesenfeld, B.; Bertolino, C.; Dutta, D.; Cao, Z.; Tan, W.; Moudgil, B. M.; Mericle, R. a. *J. Lumin.* **2006**, *117*, 75.

(52) Margarida Pereira, A.; Cristina Abreu, A.; Simões, M. *J. Microbiol. Res.* **2012**, *2*, 84.

(53) Decker, T.; Lohmann-Matthes, M. L. *J. Immunol. Methods* **1988**, *115*, 61.

BIBLIOGRAPHY

(1) Ahn, S. H.; Guo, L. J. *ACS Nano* **2009**, *3*, 2304.

(2) Altman, G. H.; Diaz, F.; Jakuba, C.; Calabro, T.; Horan, R. L.; Chen, J.; Lu, H.; Richmond, J.; Kaplan, D. L. *Biomaterials* **2003**, *24*, 401.

(3) Ameloot, R.; Vermoortele, F.; Vanhove, W.; Roeffaers, M. B. J.; Sels, B. F.; De Vos, D. E. *Nat. Chem.* **2011**, *3*, 382.

(4) Amin, S.; Ustunol, Z. *Int. J. Dairy Technol.* **2007**, *60*, 149.

(5) Amsden, J. J.; Domachuk, P.; Gopinath, A.; White, R. D.; Negro, L. D.; Kaplan, D. L.; Omenetto, F. G. *Adv. Mater.* **2010**, *22*, 1746.

(6) Anyango, J. O.; Taylor, J.; Taylor, J. R. N. *J. Agric. Food Chem.* **2011**, *59*, 12674.

(7) Arora, A.; Padua, G. W. *J. Food Sci.* **2010**, *75*, R43.

(8) Atwater, H. A.; Polman, A. *Nat. Mater.* **2010**, *9*, 205.

(9) Balmer, J. A.; Schmid, A.; Armes, S. P. *J. Mater. Chem.* **2008**, *18*, 5722.

(10) Banerjee, I.; Pangule, R. C.; Kane, R. S. *Adv. Mater.* **2011**, *23*, 690.

(11) Becker, J. S. *Int. J. Mass Spectrom.* **2010**, *289*, 65.

(12) Behrens, S. *Nanoscale* **2011**, *3*, 877.

(13) Bettinger, C. J.; Bruggeman, J. P.; Misra, A.; Borenstein, J. T.; Langer, R. *Biomaterials* **2009**, *30*, 3050.

(14) Bigi, A.; Cojazzi, G.; Panzavolta, S.; Rubini, K.; Roveri, N. *Biomaterials* **2001**, *22*, 763.

(15) Binks, B. P.; Lumsdon, S. O. *Langmuir* **2000**, *16*, 8622.

(16) Binks, B. P. *Curr. Opin. Colloid Interface Sci.* **2002**, *7*, 21.

(17) Bombelli, F. B.; Webster, C. a; Moncrieff, M.; Sherwood, V. *Lancet. Oncol.* **2014**, *15*, e22.

(18) Brust, M.; Walker, M.; Bethell, D.; Schiffrin, D. J.; Whyman, R. *J. Chem. Soc. Chem. Commun.* **1994**, 801.

(19) Burt, S. *Int. J. Food Microbiol.* **2004**, *94*, 223.

(20) Bushdid, C.; Magnasco, M. O.; Vosshall, L. B.; Keller, A. *Science (80-.).* **2014**, *343*, 1370.

(21) Busscher, H. J.; Rinastiti, M.; Siswomihardjo, W.; van der Mei, H. C. *J. Dent. Res.* **2010**, *89*, 657.

(22) Cao, N.; Fu, Y.; He, J. *Food Hydrocoll.* **2007**, *21*, 1153.

(23) Carpenter, A. W.; Worley, B. V; Slomberg, D. L.; Schoenfisch, M. H. *Biomacromolecules* **2012**, *13*, 3334.

(24) Caruso, F.; Caruso, R. A.; Möhwald, H. *Science* **1998**, *282*, 1111.

(25) Chang, Y.; McLandsborough, L.; McClements, D. J. *J. Agric. Food Chem.* **2013**, *61*, 8906.

(26) Chen, H.; Davidson, P. M.; Zhong, Q. *Appl. Environ. Microbiol.* **2014**, *80*, 907.

(27) Chen, T.; Colver, P. J.; Bon, S. A. F. *Adv. Mater.* **2007**, *19*, 2286.

(28) Chen, X.; Su, Y.-D.; Ajeti, V.; Chen, S.-J.; Campagnola, P. J. *Cell. Mol. Bioeng.* **2012**, *5*, 307.

(29) Chien, K. B.; Shah, R. N. *Acta Biomater.* **2012**, *8*, 694.

(30) Choi, Y. S.; Hong, S. R.; Lee, Y. M.; Song, K. W.; Park, M. H.; Nam, Y. S. *Biomaterials* **1999**, *20*, 409.

(31) Ciriminna, R.; Fidalgo, A.; Pandarus, V.; Béland, F.; Ilharco, L. M.; Pagliaro, M. *Chem. Rev.* **2013**, *113*, 6592.

(32) Condés, M. C.; Añón, M. C.; Mauri, A. N. *J. Food Eng.* **2013**, *119*, 573.

(33) Costerton, J. W. *Science (80-.).* **1999**, *284*, 1318.

(34) Costerton, J. W.; Montanaro, L.; Arciola, C. R. *Int. J. Artif. Organs* **2005**, *28*, 1062.

(35) Costerton, W.; Veeh, R.; Shirtliff, M.; Pasmore, M.; Post, C.; Ehrlich, G. *J. Clin. Invest.* **2003**, *112*, 1466.

(36) Creran, B.; Li, X.; Duncan, B.; Kim, C. S.; Moyano, D. F.; Rotello, V. M. *ACS Appl. Mater. Interfaces* **2014**, *6*, 19525.

(37) De, M.; Ghosh, P. S.; Rotello, V. M. *Adv. Mater.* **2008**, *20*, 4225.

(38) Decker, T.; Lohmann-Matthes, M. L. *J. Immunol. Methods* **1988**, *115*, 61.

(39) Delaney, J. T.; Smith, P. J.; Schubert, U. S. *Soft Matter* **2009**, *5*, 4866.

(40) Dreaden, E. C.; Alkilany, A. M.; Huang, X.; Murphy, C. J.; El-Sayed, M. A. *Chem. Soc. Rev.* **2012**, *41*, 2740.

(41) Duncan, B.; Elci, S. G.; Rotello, V. M. *Nano Today* **2012**, *7*, 228.

(42) Duncan, B.; Kim, C.; Rotello, V. M. *J. Control. Release* **2010**, *148*, 122.

(43) Duncan, B.; Landis, R. F.; Jerri, H. a; Normand, V.; Benczédi, D.; Ouali, L.; Rotello, V. M. *Small* **2015**, *11*, 1302.

(44) Dunkel, A.; Steinhaus, M.; Kotthoff, M.; Nowak, B.; Krautwurst, D.; Schieberle, P.; Hofmann, T. *Angew. Chem. Int. Ed. Engl.* **2014**, *53*, 7124.

(45) Ehrlich, G. D.; Veeh, R.; Wang, X.; Costerton, J. W.; Hayes, J. D.; Hu, F. Z.; Daigle, B. J.; Ehrlich, M. D.; Post, J. C. *JAMA* **2002**, *287*, 1710.

(46) Fielding, L. A.; Armes, S. P. *J. Mater. Chem.* **2012**, *22*, 11235.

(47) Fredin, N. J.; Broderick, A. H.; Buck, M. E.; Lynn, D. M. *Biomacromolecules* **2009**, *10*, 994.

(48) Fujii, S.; Read, E. S.; Binks, B. P.; Armes, S. P. *Adv. Mater.* **2005**, *17*, 1014.

(49) Fukuda, J.; Khademhosseini, A.; Yeh, J.; Eng, G.; Cheng, J.; Farokhzad, O. C.; Langer, R. *Biomaterials* **2006**, *27*, 1479.

(50) Gagner, J. E.; Kim, W.; Chaikof, E. L. *Acta Biomater.* **2014**, *10*, 1542.

(51) Gennadios, A, Ed.; *Protein-Based Films and Coatings*; CRC Press, 2002.

(52) Ghouchi Eskandar, N.; Simovic, S.; Prestidge, C. A. *Pharm. Res.* **2009**, *26*, 1764.

(53) Gil, E. S.; Panilaitis, B.; Bellas, E.; Kaplan, D. L. *Adv. Healthc. Mater.* **2013**, *2*, 206.

(54) Gomes, C.; Moreira, R. G.; Castell-Perez, E. *J. Food Sci.* **2011**, *76*, N16.

(55) Gomes, S.; Leonor, I. B.; Mano, J. F.; Reis, R. L.; Kaplan, D. L. *Prog. Polym. Sci.* **2012**, *37*, 1.

(56) González-Díaz, J. B.; García-Martín, A.; Armelles, G.; Navas, D.; Vázquez, M.; Nielsch, K.; Wehrspohn, R. B.; Gösele, U. *Adv. Mater.* **2007**, *19*, 2643.

(57) Goswami, S.; Thiyagarajan, D.; Das, G.; Ramesh, A. *ACS Appl. Mater. Interfaces* **2014**, *6*, 16384.

(58) Graf, C.; Vossen, D. L. J.; Imhof, A.; van Blaaderen, A. *Langmuir* **2003**, *19*, 6693.

(59) Greenfield, N. J. *Nat. Protoc.* **2006**, *1*, 2876.

(60) Groseclose, M. R.; Castellino, S. *Anal. Chem.* **2013**, *85*, 10099.

(61) Hammond, P. T. *AIChE J.* **2015**, *61*, 1106.

(62) Har-el, Y.; Gerstenhaber, J. a.; Brodsky, R.; Huneke, R. B.; Lelkes, P. I. *Wound Med.* **2014**, *5*, 9.

(63) Harrison, J. J.; Ceri, H.; Turner, R. J. *Nat. Rev. Microbiol.* **2007**, *5*, 928.

(64) Hellwig, M.; Henle, T. *Angew. Chemie Int. Ed.* **2014**, *53*, 10316.

(65) Hemaiswarya, S.; Kruthiventi, A. K.; Doble, M. *Phytomedicine* **2008**, *15*, 639.

(66) Hernández-Muñoz, P.; Villalobos, R.; Chiralt, A. *Food Hydrocoll.* **2004**, *18*, 647.

(67) Herrmann, A. *Angew. Chem. Int. Ed. Engl.* **2007**, *46*, 5836.

(68) Hofmann, S.; Wong Po Foo, C. T.; Rossetti, F.; Textor, M.; Vunjak-Novakovic, G.; Kaplan, D. L.; Merkle, H. P.; Meinel, L. *J. Control. Release* **2006**, *111*, 219.

(69) Hsu, M. F.; Nikolaides, M. G.; Dinsmore, A. D.; Bausch, A. R.; Gordon, V. D.; Chen, X.; Hutchinson, J. W.; Weitz, D. A.; Marquez, M. *Langmuir* **2005**, *21*, 2963.

(70) Hu, X.; Cebe, P.; Weiss, A. S.; Omenetto, F.; Kaplan, D. L. *Mater. Today* **2012**, *15*, 208.

(71) Huang, C.; Dong, B.; Lu, N.; Yang, B.; Gao, L.; Tian, L.; Qi, D.; Wu, Q.; Chi, L. *Small* **2009**, *5*, 583.

(72) Hurdle, J. G.; O'Neill, A. J.; Chopra, I.; Lee, R. E. *Nat. Rev. Microbiol.* **2011**, *9*, 62.

(73) James, G. A.; Swogger, E.; Wolcott, R.; Pulcini, E. deLancey; Secor, P.; Sestrich, J.; Costerton, J. W.; Stewart, P. S. *Wound Repair Regen.* **2008**, *16*, 37.

(74) Jancar, J.; Douglas, J. F.; Starr, F. W.; Kumar, S. K.; Cassagnau, P.; Lesser, A. J.; Sternstein, S. S.; Buehler, M. J. *Polymer (Guildf).* **2010**, *51*, 3321.

(75) Jeong, Y.; Duncan, B.; Park, M.-H.; Kim, C.; Rotello, V. M. *Chem. Commun. (Camb).* **2011**, *47*, 12077.

(76) Jeoung, E.; Duncan, B.; Wang, L.-S.; Saha, K.; Subramani, C.; Wang, P.; Yeh, Y.; Kushida, T.; Engel, Y.; Barnes, M. D.; Rotello, V. M. *Adv. Mater.* **2015**, *27*, 6251.

(77) Jiang, S.; Cao, Z. *Adv. Mater.* **2010**, *22*, 920.

(78) Jiang, Y.; Huo, S.; Mizuhara, T.; Das, R.; Lee, Y.; Hou, S.; Moyano, D. F.; Duncan, B.; Liang, X.; Rotello, V. M. *ACS Nano* **2015**, *9*, 9986.

(79) Jin, H.-J.; Park, J.; Karageorgiou, V.; Kim, U.-J.; Valluzzi, R.; Cebe, P.; Kaplan, D. L. *Adv. Funct. Mater.* **2005**, *15*, 1241.

(80) Johnston, A. P. R.; Such, G. K.; Ng, S. L.; Caruso, F. *Curr. Opin. Colloid Interface Sci.* **2011**, *16*, 171.

(81) Kalemba, D.; Kunicka, A. *Curr. Med. Chem.* **2003**, *10*, 813.

(82) Kanaras, A. G.; Kamounah, F. S.; Schaumburg, K.; Kiely, C. J.; Brust, M. *Chem. Commun.* **2002**, 2294.

(83) Kavanaugh, N. L.; Ribbeck, K. *Appl. Environ. Microbiol.* **2012**, *78*, 4057.

(84) Kharlampieva, E.; Kozlovskaya, V.; Wallet, B.; Shevchenko, V. V; Naik, R. R.; Vaia, R.; Kaplan, D. L.; Tsukruk, V. V. *ACS Nano* **2010**, *4*, 7053.

(85) Kim, C. S.; Le, N. D. B.; Xing, Y.; Yan, B.; Tonga, G. Y.; Kim, C.; Vachet, R. W.; Rotello, V. M. *Adv. Healthc. Mater.* **2014**, *3*, 1200.

(86) Kim, D.-H.; Viventi, J.; Amsden, J. J.; Xiao, J.; Vigeland, L.; Kim, Y.-S.; Blanco, J. A.; Panilaitis, B.; Frechette, E. S.; Contreras, D.; Kaplan, D. L.; Omenetto, F. G.; Huang, Y.; Hwang, K.-C.; Zakin, M. R.; Litt, B.; Rogers, J. A. *Nat. Mater.* **2010**, *9*, 511.

(87) Kim, S.; Marelli, B.; Brenckle, M. a.; Mitropoulos, A. N.; Gil, E.-S.; Tsioris, K.; Tao, H.; Kaplan, D. L.; Omenetto, F. G. *Nat. Nanotechnol.* **2014**, *9*, 306.

(88) Knowles, T. P. J.; Oppenheim, T. W.; Buell, A. K.; Chirgadze, D. Y.; Welland, M. E. *Nat. Nanotechnol.* **2010**, *5*, 204.

(89) Kuhnt, T.; Herrmann, A.; Benczédi, D.; Foster, E. J.; Weder, C. *Polym. Chem.* **2015**, *6*, 6553.

(90) Kuhnt, T.; Herrmann, A.; Benczédi, D.; Weder, C.; Foster, E. J. *RSC Adv.* **2014**, *4*, 50882.

(91) Kundu, B.; Kurland, N. E.; Bano, S.; Patra, C.; Engel, F. B.; Yadavalli, V. K.; Kundu, S. C. *Prog. Polym. Sci.* **2014**, *39*, 251.

(92) Lang, N.; Pereira, M. J.; Lee, Y.; Friehs, I.; Vasilyev, N. V; Feins, E. N.; Ablasser, K.; O'Cearbhaill, E. D.; Xu, C.; Fabozzo, A.; Padera, R.; Wasserman, S.; Freudenthal, F.; Ferreira, L. S.; Langer, R.; Karp, J. M.; del Nido, P. J. *Sci. Transl. Med.* **2014**, *6*, 218ra6.

(93) Lee, K.-B.; Park, S.-J.; Mirkin, C. A.; Smith, J. C.; Mrksich, M. *Science* **2002**, *295*, 1702.

(94) Levy, S. B.; Marshall, B. *Nat. Med.* **2004**, *10*, S122.

(95) Li, X.; Kong, H.; Mout, R.; Saha, K.; Moyano, D. F.; Robinson, S. M.; Rana, S.; Zhang, X.; Riley, M. A.; Rotello, V. M. *ACS Nano* **2014**.

(96) Li, X.; Robinson, S. M.; Gupta, A.; Saha, K.; Jiang, Z.; Moyano, D. F.; Sahar, A.; Riley, M. A.; Rotello, V. M. *ACS Nano* **2014**, *8*, 10682.

(97) Li, X.; Yeh, Y.; Giri, K.; Mout, R.; Landis, R. F.; Prakash, Y. S.; Rotello, V. M. *Chem. Commun.* **2015**, *51*, 282.

(98) Liang, R.; Xu, S.; Shoemaker, C. F.; Li, Y.; Zhong, F.; Huang, Q. *J. Agric. Food Chem.* **2012**, *60*, 7548.

(99) Lindsay, D.; von Holy, A. *J. Hosp. Infect.* **2006**, *64*, 313.

(100) Liou, Y. R.; Torng, W.; Kao, Y. C.; Sung, K. Bin; Lee, C. H.; Kuo, P. L. *PLoS One* **2014**, *9*.

(101) Liscio, A.; Palermo, V.; Samorì, P. *Acc. Chem. Res.* **2010**, *43*, 541.

(102) Lu, J. T.; Lee, C. J.; Bent, S. F.; Fishman, H. A.; Sabelman, E. E. *Biomaterials* **2007**, *28*, 1486.

(103) Lupoi, J. S.; Smith, E. A. *Biotechnol. Bioeng.* **2011**, *108*, 2835.

(104) Lynch, A. S.; Robertson, G. T. *Annu. Rev. Med.* **2008**, *59*, 415.

(105) Ma, L.; Yang, Y.; Yao, J.; Shao, Z.; Chen, X. *Polym. Chem.* **2013**, *4*, 5425.

(106) Macfarlane, R. J.; Jones, M. R.; Senesi, A. J.; Young, K. L.; Lee, B.; Wu, J.; Mirkin, C. A. *Angew. Chem. Int. Ed. Engl.* **2010**, *49*, 4589.

(107) Maeda, H.; Okada, M.; Fujii, S.; Nakamura, Y.; Furuzono, T. *Langmuir* **2010**, *26*, 13727.

(108) Mann, S. *Nat. Mater.* **2009**, *8*, 781.

(109) Mao, J.; Zhao, L.; de Yao, K.; Shang, Q.; Yang, G.; Cao, Y. *J. Biomed. Mater. Res.* **2003**, *64A*, 301.

(110) Margarida Pereira, A.; Cristina Abreu, A.; Simões, M. *J. Microbiol. Res.* **2012**, *2*, 84.

(111) Marion-Ferey, K.; Pasmore, M.; Stoodley, P.; Wilson, S.; Husson, G. P.; Costerton, J. W. *J. Hosp. Infect.* **2003**, *53*, 64.

(112) Marquié, C. *J. Agric. Food Chem.* **2001**, *49*, 4676.

(113) Matsuda, S.; Iwata, H.; Se, N.; Ikada, Y. *J. Biomed. Mater. Res.* **1999**, *45*, 20.

(114) Meier, C.; Welland, M. E. *Biomacromolecules* **2011**, *12*, 3453.

(115) Miller, K. P.; Wang, L.; Benicewicz, B. C.; Decho, A. W. *Chem. Soc. Rev.* **2015**, *44*, 7787.

(116) Miranda, O. R.; Creran, B.; Rotello, V. M. *Curr. Opin. Chem. Biol.* **2010**, *14*, 728.

(117) Miranda, O. R.; Li, X.; Garcia-Gonzalez, L.; Zhu, Z.; Yan, B.; Bunz, U. H. F.; Rotello, V. M. *J. Am. Chem. Soc.* **2011**, *133*, 9650.

(118) Mout, R.; Tonga, G. Y.; Ray, M.; Moyano, D. F.; Xing, Y.; Rotello, V. M. *Nanoscale* **2014**, *6*, 8873.

(119) Murphy, A. R.; John, P. S.; Kaplan, D. L. *Biomaterials* **2008**, *29*, 2829.

(120) Nabeshi, H.; Yoshikawa, T.; Matsuyama, K.; Nakazato, Y.; Matsuo, K.; Arimori, A.; Isobe, M.; Tochigi, S.; Kondoh, S.; Hirai, T.; Akase, T.; Yamashita, T.; Yamashita, K.; Yoshida, T.; Nagano, K.; Abe, Y.; Yoshioka, Y.; Kamada, H.; Imazawa, T.; Itoh, N.; Nakagawa, S.; Mayumi, T.; Tsunoda, S.; Tsutsumi, Y. *Biomaterials* **2011**, *32*, 2713.

(121) Niu, Z.; He, J.; Russell, T. P.; Wang, Q. *Angew. Chemie Int. Ed.* **2010**, *49*, 10052.

(122) Nostro, A.; Roccaro, A. S.; Bisignano, G.; Marino, A.; Cannatelli, M. A.; Pizzimenti, F. C.; Cioni, P. L.; Procopio, F.; Blanco, A. R. *J. Med. Microbiol.* **2007**, *56*, 519.

(123) Omenetto, F. G.; Kaplan, D. L. *Science (80-.).* **2010**, *329*, 528.

(124) Park, J. S.; Chu, J. S.; Tsou, A. D.; Diop, R.; Tang, Z.; Wang, A.; Li, S. *Biomaterials* **2011**, *32*, 3921.

(125) Park, J.; Lee, E.; Hwang, N.-M.; Kang, M.; Kim, S. C.; Hwang, Y.; Park, J.-G.; Noh, H.-J.; Kim, J.-Y.; Park, J.-H.; Hyeon, T. *Angew. Chemie Int. Ed.* **2005**, *44*, 2872.

(126) Park, M.-H.; Agasti, S. S.; Creran, B.; Kim, C.; Rotello, V. M. *Adv. Mater.* **2011**, *23*, 2839.

(127) Park, S. K.; Bae, D. H.; Rhee, K. C. *J. Am. Oil Chem. Soc.* **2000**, *77*, 879.

(128) Pati, F.; Jang, J.; Ha, D.-H.; Won Kim, S.; Rhie, J.-W.; Shim, J.-H.; Kim, D.-H.; Cho, D.-W. *Nat. Commun.* **2014**, *5*, 3935.

(129) Peles, Z.; Binderman, I.; Berdicevsky, I.; Zilberman, M. *J. Tissue Eng. Regen. Med.* **2013**, *7*, 401.

(130) Perry, H.; Gopinath, A.; Kaplan, D. L.; Dal Negro, L.; Omenetto, F. G. *Adv. Mater.* **2008**, *20*, 3070.

(131) Phillips, R. L.; Miranda, O. R.; You, C.-C.; Rotello, V. M.; Bunz, U. H. F. *Angew. Chemie Int. Ed.* **2008**, *47*, 2590.

(132) Philpott, C. M.; Wolstenholme, C. R.; Goodenough, P. C.; Clark, a; Murty, G. E. *J. Laryngol. Otol.* **2008**, *122*, 912.

(133) Pickering, S. U. *J. Chem. Soc. Trans.* **1907**, *91*, 2001.

(134) Pieranski, P. *Phys. Rev. Lett.* **1980**, *45*, 569.

(135) Pinheiro, A. V.; Han, D.; Shih, W. M.; Yan, H. *Nat. Nanotechnol.* **2011**, *6*, 763.

(136) Prabhakar, U.; Maeda, H.; Jain, R. K.; Sevick-Muraca, E. M.; Zamboni, W.; Farokhzad, O. C.; Barry, S. T.; Gabizon, A.; Grodzinski, P.; Blakey, D. C. *Cancer Res.* **2013**, *73*, 2412.

(137) Pritchard, E. M.; Valentin, T.; Panilaitis, B.; Omenetto, F.; Kaplan, D. L. *Adv. Funct. Mater.* **2013**, *23*, 854.

(138) Pyayt, A. L.; Wiley, B.; Xia, Y.; Chen, A.; Dalton, L. *Nat. Nanotechnol.* **2008**, *3*, 660.

(139) Qiu, G.-M.; Zhu, L.-P.; Zhu, B.-K.; Xu, Y.-Y.; Qiu, G.-L. *J. Supercrit. Fluids* **2008**, *45*, 374.

(140) Radovic-Moreno, A. F.; Lu, T. K.; Puscasu, V. a; Yoon, C. J.; Langer, R.; Farokhzad, O. C. *ACS Nano* **2012**, *6*, 4279.

(141) Ramanathan, R.; Campbell, J. L.; Soni, S. K.; Bhargava, S. K.; Bansal, V. *PLoS One* **2011**, *6*, e17707.

(142) Ramsden, W. *Proc. R. Soc. London* **1903**, *72*, 156.

(143) Rana, S.; Le, N. D. B.; Mout, R.; Duncan, B.; Elci, S. G.; Saha, K.; Rotello, V. M. *ACS Cent. Sci.* **2015**, *1*, 191.

(144) Rancan, F.; Gao, Q.; Graf, C.; Troppens, S.; Hadam, S.; Hackbarth, S.; Kembuan, C.; Blume-Peytavi, U.; Rühl, E.; Lademann, J.; Vogt, A. *ACS Nano* **2012**, *6*, 6829.

(145) Rangavajhyala, N.; Ghorpade, V.; Hanna, M. *J. Agric. Food Chem.* **1997**, *45*, 4204.

(146) Reddy, N.; Tan, Y.; Li, Y.; Yang, Y. *Macromol. Mater. Eng.* **2008**, *293*, 614.

(147) Rhim, J. W.; Park, H. M.; Ha, C. S. *Prog. Polym. Sci.* **2013**, *38*, 1629.

(148) Rhim, J. W.; Gennadios, A.; Fu, D.; Weller, C. L.; Hanna, M. a. *LWT - Food Sci. Technol.* **1999**, *32*, 129.

(149) Rhim, J. W.; Gennadios, A.; Handa, A.; Weller, C. L.; Hanna, M. a. *J. Agric. Food Chem.* **2000**, *48*, 4937.

(150) Ricci, M.; Trinquecoste, M.; Auguste, F.; Canet, R.; Delhaes, P.; Guimon, C.; Pfister-Guillouzo, G.; Nysten, B.; Issi, J. P. *J. Mater. Res.* **1993**, *8*, 480.

(151) Richardson, J. J.; Bjornmalm, M.; Caruso, F. *Science (80-.).* **2015**, *348*, aaa2491.

(152) Richardson, J. J.; Bjornmalm, M.; Caruso, F. *Science (80-.).* **2015**, *348*, aaa2491.

(153) Roberts, M. J.; Bhatt, N.; Voge, C. M.; Meshot, E. R.; Stegemann, J. P.; Hart, A. J. *J. Mater. Chem. B* **2013**, *1*, 4711.

(154) Rosen, J. E.; Gu, F. X. *Langmuir* **2011**, *27*, 10507.

(155) Roy, S.; Elgharably, H.; Sinha, M.; Ganesh, K.; Chaney, S.; Mann, E.; Miller, C.; Khanna, S.; Bergdall, V. K.; Powell, H. M.; Cook, C. H.; Gordillo, G. M.; Wozniak, D. J.; Sen, C. K. *J. Pathol.* **2014**, *233*, 331.

(156) Saha, K.; Bajaj, A.; Duncan, B.; Rotello, V. M. *Small* **2011**, *7*, 1903.

(157) Sakakibara, K.; Hill, J. P.; Ariga, K. *Small* **2011**, *7*, 1288.

(158) Sanchez, C.; Shea, K. J.; Kitagawa, S. *Chem. Soc. Rev.* **2011**, *40*, 471.

(159) Santra, S.; Liesenfeld, B.; Bertolino, C.; Dutta, D.; Cao, Z.; Tan, W.; Moudgil, B. M.; Mericle, R. a. *J. Lumin.* **2006**, *117*, 75.

(160) Saxena, A.; Tripathi, B. P.; Shahi, V. K. *J. Phys. Chem. B* **2007**, *111*, 12454.

(161) Schladt, T. D.; Schneider, K.; Schild, H.; Tremel, W. *Dalton Trans.* **2011**, *40*, 6315.

(162) Scholl, J. A.; Koh, A. L.; Dionne, J. A. *Nature* **2012**, *483*, 421.

(163) Sela, L.; Sobel, N. *Exp. Brain Res.* **2010**, *205*, 13.

(164) Shah, N. J.; Hyder, M. N.; Moskowitz, J. S.; Quadir, M. A.; Morton, S. W.; Seeherman, H. J.; Padera, R. F.; Spector, M.; Hammond, P. T. *Sci. Transl. Med.* **2013**, *5*, 191ra83.

(165) Shah, N. J.; Hong, J.; Hyder, M. N.; Hammond, P. T. *Adv. Mater.* **2012**, *24*, 1445.

(166) Shah, N. J.; Hyder, M. N.; Moskowitz, J. S.; Quadir, M. a; Morton, S. W.; Seeherman, H. J.; Padera, R. F.; Spector, M.; Hammond, P. T. *Sci. Transl. Med.* **2013**, *5*, 191ra83.

(167) Shalel, S.; Streichman, S.; Marmur, A. *J. Colloid Interface Sci.* **2002**, *252*, 66.

(168) Silva, N. H. C. S.; Vilela, C.; Marrucho, I. M.; Freire, C. S. R.; Pascoal Neto, C.; Silvestre, A. J. D. *J. Mater. Chem. B* **2014**, *2*, 3715.

(169) Sim, H. R.; Wark, A. W.; Lee, H. J. *Analyst* **2010**, *135*, 2528.

(170) Sinensky, A. K.; Belcher, A. M. *Nat. Nanotechnol.* **2007**, *2*, 653.

(171) Smith, K. H.; Tejeda-Montes, E.; Poch, M.; Mata, A. *Chem. Soc. Rev.* **2011**, *40*, 4563.

(172) Solov'yov, I. a.; Chang, P.-Y.; Schulten, K. *Phys. Chem. Chem. Phys.* **2012**, *14*, 13861.

(173) Soto-Cantu, E.; Cueto, R.; Koch, J.; Russo, P. S. *Langmuir* **2012**, *28*, 5562.

(174) Stewart, P. S.; William Costerton, J. *Lancet* **2001**, *358*, 135.

(175) Stöber, W.; Fink, A.; Bohn, E. *J. Colloid Interface Sci.* **1968**, *26*, 62.

(176) Subramani, C.; Saha, K.; Creran, B.; Bajaj, A.; Moyano, D. F.; Wang, H.; Rotello, V. M. *Small* **2012**, *8*, 1209.

(177) Subramani, C.; Yu, X.; Agasti, S. S.; Duncan, B.; Eymur, S.; Tonga, M.; Rotello, V. M. *J. Mater. Chem.* **2011**, *21*, 14156.

(178) Such, G. K.; Johnston, A. P. R.; Caruso, F. *Chem. Soc. Rev.* **2011**, *40*, 19.

(179) Sun, B. K.; Siprashvili, Z.; Khavari, P. a. *Science (80-.).* **2014**, *346*, 941.

(180) Sun, T.; Qing, G.; Su, B.; Jiang, L. *Chem. Soc. Rev.* **2011**, *40*, 2909.

(181) Szomolay, B.; Klapper, I.; Dockery, J.; Stewart, P. S. *Environ. Microbiol.* **2005**, *7*, 1186.

(182) Takasao, N.; Tsuji-Naito, K.; Ishikura, S.; Tamura, A.; Akagawa, M. *J. Agric. Food Chem.* **2012**, *60*, 1193.

(183) Tan, K. L.; Tan, B. T. G.; Kang, E. T.; Neoh, K. G. *Phys. Rev. B* **1989**, *39*, 8070.

(184) Tang, R.; Moyano, D. F.; Subramani, C.; Yan, B.; Jeoung, E.; Tonga, G. Y.; Duncan, B.; Yeh, Y.-C.; Jiang, Z.; Kim, C.; Rotello, V. M. *Adv. Mater.* **2014**, *26*, 3310.

(185) Tang, R.; Moyano, D. F.; Subramani, C.; Yan, B.; Jeoung, E.; Tonga, G. Y.; Duncan, B.; Yeh, Y.-C.; Jiang, Z.; Kim, C.; Rotello, V. M. *Adv. Mater.* **2014**, *26*, 3310.

(186) Tao, H.; Marelli, B.; Yang, M.; An, B.; Onses, S.; Rogers, J. a.; Kaplan, D. L.; Omenetto, F. G. *Adv. Mater.* **2015**, n/a.

(187) Tejaswi Naidu, K.; Prakash Prabhu, N. *J. Phys. Chem. B* **2011**, *115*, 14760.

(188) Templeton, A. C.; Wuelfing, W. P.; Murray, R. W. *Acc. Chem. Res.* **2000**, *33*, 27.

(189) Tokarev, I.; Minko, S. *Soft Matter* **2012**, *8*, 5980.

(190) Tonga, G. Y.; Jeong, Y.; Duncan, B.; Mizuhara, T.; Mout, R.; Das, R.; Kim, S. T.; Yeh, Y.-C.; Yan, B.; Hou, S.; Rotello, V. M. *Nat. Chem.* **2015**, *7*, 597.

(191) Tonga, G. Y.; Saha, K.; Rotello, V. M. *Adv. Mater.* **2014**, *26*, 359.

(192) Tsuchiya, H.; Hoshino, Y.; Tajima, K.; Takagi, N. *J. Prosthet. Dent.* **1994**, *71*, 618.

(193) Tsukatani, T.; Miwa, T.; Furukawa, M.; Costanzo, R. M. *Chem. Senses* **2003**, *28*, 25.

(194) Vaz, C. M.; De Graaf, L. a; Reis, R. L.; Cunha, A. M. *J. Mater. Sci. Mater. Med.* **2003**, *14*, 789.

(195) Wahba, L.; D'Arienzo, M.; Donetti, R.; Hanel, T.; Scotti, R.; Tadiello, L.; Morazzoni, F. *RSC Adv.* **2013**, *3*, 5832.

(196) Wang, D.; Salgueiriño-Maceira, V.; Liz-Marzán, L. M.; Caruso, F. *Adv. Mater.* **2002**, *14*, 908.

(197) Warren, S. C.; Perkins, M. R.; Adams, A. M.; Kamperman, M.; Burns, A. a; Arora, H.; Herz, E.; Suteewong, T.; Sai, H.; Li, Z.; Werner, J.; Song, J.; Werner-Zwanziger, U.; Zwanziger, J. W.; Grätzel, M.; DiSalvo, F. J.; Wiesner, U. *Nat. Mater.* **2012**, *11*, 460.

(198) Watt, F. M. *Science (80-.).* **2014**, *346*, 937.

(199) Werkmeister, J. A.; Ramshaw, J. A. M. *Biomed. Mater.* **2012**, *7*, 012002.

(200) Westcott, S. L.; Oldenburg, S. J.; Lee, T. R.; Halas, N. J. *Langmuir* **1998**, *14*, 5396.

(201) Whitesides, G. M. *Angew. Chemie Int. Ed.* **2015**, *54*, 3196.

(202) WHO (2011) Guidelines for drinking-water quality -4th ed. Geneva, Switzerland: WHO Press.

(203) WHO, UNICEF (2014) Progress on drinking water and sanitation: 2014 Update. Geneva, Switzerland: WHO Press.

(204) Wihodo, M.; Moraru, C. I. *J. Food Eng.* **2013**, *114*, 292.

(205) Wilhelm, K.-P.; Freitag, G.; Wolff, H. H. *J. Am. Acad. Dermatol.* **1994**, *30*, 944.

(206) Williams, M.; Warren, N. J.; Fielding, L. A.; Armes, S. P.; Verstraete, P.; Smets, J. *ACS Appl. Mater. Interfaces* **2014**, *6*, 20919.

(207) Xu, P.; Han, X.; Zhang, B.; Du, Y.; Wang, H.-L. *Chem. Soc. Rev.* **2014**, *43*, 1349.

(208) Yan, B.; Zhu, Z.-J.; Miranda, O. R.; Chompoosor, A.; Rotello, V. M.; Vachet, R. W. *Anal. Bioanal. Chem.* **2010**, *396*, 1025.

(209) Yang, H.; Fu, L.; Wei, L.; Liang, J.; Binks, B. P. *J. Am. Chem. Soc.* **2015**, *137*, 1362.

(210) Yang, K.; Hu, L.; Ma, X.; Ye, S.; Cheng, L.; Shi, X.; Li, C.; Li, Y.; Liu, Z. *Adv. Mater.* **2012**, *24*, 1868.

(211) Yang, X.-C.; Samanta, B.; Agasti, S. S.; Jeong, Y.; Zhu, Z.-J.; Rana, S.; Miranda, O. R.; Rotello, V. M. *Angew. Chemie Int. Ed.* **2011**, *50*, 477.

(212) Yermolenko, I. S.; Gorkun, O. V; Fuhrmann, A.; Podolnikova, N. P.; Lishko, V. K.; Oshkadyerov, S. P.; Lord, S. T.; Ros, R.; Ugarova, T. P. *J. Biol. Chem.* **2012**, *287*, 41979.

(213) Yoon, S.-H.; Kim, Y. K.; Han, E. D.; Seo, Y.-H.; Kim, B. H.; Mofrad, M. R. K. *Lab Chip* **2012**, *12*, 2391.

(214) You, C.-C.; Miranda, O. R.; Gider, B.; Ghosh, P. S.; Kim, I.-B.; Erdogan, B.; Krovi, S. A.; Bunz, U. H. F.; Rotello, V. M. *Nat. Nanotechnol.* **2007**, *2*, 318.

(215) Zhang, H.; Mittal, G. *Environ. Prog. Sustain. Energy* **2010**, *29*, 203.

(216) Zhao, Y.; Jiang, Q.; Xu, H.; Reddy, N.; Xu, L.; Yang, Y. *J. Biomed. Mater. Res. - Part B Appl. Biomater.* **2014**, *102*, 729.

(217) Zheng, W.; Zhang, W.; Jiang, X. *Adv. Healthc. Mater.* **2013**, *2*, 95.

(218) Zhu, X.; Radovic-Moreno, A. F.; Wu, J.; Langer, R.; Shi, J. *Nano Today* **2014**, *9*, 478.

(219) Zou, H.; Wu, S.; Shen, J. *Chem. Rev.* **2008**, *108*, 3893.